2008

Numerical simulation of three dimensional vortex-dominated flows

Abrar Hasan Mohammad
Iowa State University

Recommended Citation

Mohammad, Abrar Hasan, "Numerical simulation of three dimensional vortex-dominated flows" (2008). *Graduate Theses and Dissertations*. 10981.
https://lib.dr.iastate.edu/etd/10981

Numerical simulation of three dimensional vortex-dominated flows

by

Abrar Hasan Mohammad

A thesis submitted to the graduate faculty

in partial fulfillment of the requirements for the degree of

MASTER OF SCIENCE

Major: Aerospace Engineering

Program of Study Committee:
Z. J. Wang, Major Professor
Tom I-P. Shih
Richard H. Pletcher

Iowa State University

Ames, Iowa

2008

TABLE OF CONTENTS

LIST OF FIGURES

LIST OF TABLES

LIST OF SYMBOLS

ρ = Density

u = Velocity component along x-axis

v = Velocity component along y-axis

w = Velocity component along z-axis

E = Energy

p = Pressure

μ = Coefficient of Viscosity

C_p = Coefficient of Pressure

P_r = Prandtl Number

γ = Ratio of Specific heats

J = Jacobian matrix

Re_D = Reynolds number based on cylinder diameter

λ_z = Wavelength

U_∞ = Free-stream velocity along x-axis

ΔT = Non-dimensional time step

$\Delta r_{\min}$ = Minimum size of a cell

<u> = Average value of velocity component along x-axis

<v> = Average value of velocity component along y-axis

<u'u'> = Component of Reynolds stress

<v'v'> = Component of Reynolds stress

<u'v'> = Component of Reynolds stress

u_{rms} = Root Mean Square (r.m.s.) of velocity along x-axis

v_{rms} = Root Mean Square (r.m.s.) of velocity along y-axis

q_∞ = Dynamic pressure

r_o = Initial Radius of a spiral

α = constant

H = Height of the turbine

D = Diameter of spiral

ACKNOWLEDGEMENTS

I wish to express my sincere gratitude to my supervisor Prof. Z. J. Wang of the Department of Aerospace Engineering at Iowa State University for his constant inspiration, guidance and personal attention while carrying out my master’s work. Prof Z. J. Wang helped me in making my work a success and gave me the opportunity to learn. I am indebted to him for extending all the necessary support during the course of the work.

I would also like to give appreciative thanks to Dr. Chunlei Liang, Prof. Paul Durbin and Prof. Richard Pletcher for their suggestions for turbulent flow across bluff bodies. I would also like to thank Prof. Tom Shih for serving as my committee member. My heartfelt thanks are due to my fellow group members for their help and cooperation during my work.

Last but not least, thanks to my parents and my friend Ayesha for their love and inspiration

ABSTRACT

The objective of the present work was to investigate three dimensional unsteady vortex dominated flows using the spectral difference (SD) method and finite volume (FV) method. The simulations were carried out over a circular cylinder, a delta wing and a spiral-shaped wind turbine. SD method was used to demonstrate its potential in Large Eddy Simulation (LES) of flow over a cylinder and also to predict the mean and instantaneous flow structure over a delta wing. FLUENT and MUSIC (2nd order FV solvers) were used to study the flow behavior in a spiral-shaped wind turbine designed to extract maximum power out of it.

Large eddy simulation of the flow over a circular cylinder at Reynolds number $Re_D = 2580$ was studied with a high-order unstructured SD method. Grid and accuracy refinement studies were carried out to assess numerical errors. The mean and fluctuating velocity fields in the wake of a circular cylinder were compared with PIV experimental measurements. The numerical results are in an excellent agreement with the measurements for both the mean velocity and Reynolds stresses. Other wake characteristics such as the re-circulation bubble length, vortex formation length and maximum intensity of the velocity fluctuations have also been predicted accurately. The numerical simulations demonstrated the potential of the high-order SD method in large eddy simulation of physically complex problems.

Computational simulations were performed for a 50^o sweep delta wing at 15^o degree angle of attack and a moderate Reynolds number of $Re = 2\times10^5$ using SD method. A preliminary study was carried out to demonstrate once again the potential of high order spectral difference method in a highly vortex dominated flow. Comparisons were made with high resolution PIV images and numerical simulations performed by Raymond and Visbal. The numerical results were examined to provide a description of the mean and instantaneous flow structure over the delta wing including the separated vortical flow and vortex breakdown. The results suggest the importance of grid resolution on the upper surface of the delta wing, to obtain a better accuracy of the vortex structure.

2nd order FV method was used to study the flow in a Tornado Type Wind Turbine (TTWT) which uses a strong Rankine vortex to generate low pressure at the turbine base. The primary aim was to design the spiral shaped turbine in order to broaden the usability of wind energy. Two solvers, FLUENT and MUSIC, both utilizing the 2nd order FV method were used to perform the CFD analysis. Grid refinement study was carried out to assess numerical errors. The effect of different parameters, like diameter of the spiral, height of the turbine and blockage effect, on the vortex strength were studied. The numerical results were compared with the experiment results. The distribution of pressure was within 5-10% of experiment values but the values are not small enough to extract high power out of the turbine.

Chapter 1 - Introduction

Lot of research on both low and high Reynolds number flows have been carried out in the past. In the recent past, Computational Fluid Dynamics (CFD) is used in many industry problems like thermal study of spent nuclear fuel casks, electronic cooling, rotor blade flows, to name a few. The advent of high computational resources has allowed the use of CFD to simulate many practical flow and thermal problems. Numerous numerical schemes have been developed and based on the performance and accuracy; they are used for problems of different nature. Tremendous amount of work has been carried out to study vortex dominated flows – flows with the formation of a vortex or multiple vortices which play an important role in the physics of the flow. After extensive research, more accurate and reliable methods have been developed – one among them being high order accurate algorithms for conservation laws. This led to the development of many methods including the discontinuous Galerkin method[9,10], the spectral volume (SV)[41,66,68] and spectral difference (SD)[28,39,40,67] method and the k-exact finite volume[1, 11] method. Depending on the nature of the problem and accuracy level desired, a 2nd order finite volume method or a high-order accurate method can be used.

1.1 Motivation

Innumerous studies have been carried out on Large Eddy Simulation of flow over a circular cylinder. In the past, 2nd order finite volume method was used along with a turbulence model like Smagorinsky, Dynamic Smagorinsky[34,35,38] and many more. The statistics obtained by Chunlei[38] for an unperturbed inlet flow were not comparable at most of the locations in the wake of the cylinder. This motivated the author to use a high order method – spectral difference method – to obtain the flow statistics in the wake of a cylinder at a sub-critical Reynolds number. Even though second order methods have achieved success, there are several areas where their performance is unsatisfactory, e.g., for vortex-dominated flows including helicopter blade vortex interactions and flow over high lift configurations. Higher order methods are more successful in handling these flows. For example, high order compact methods have demonstrated much better results than their lower order counterparts[64]. Not only are high order methods more accurate, they also have the potential to reduce the CPU time required to obtain the solutions. This again motivated the use of SD algorithm to predict the flow over a delta wing which has a highly complex flowfield involving regions of laminar, transitional and turbulent flows both on the surface of the wing and in the separated vortical flow. Most computations of the delta wing flows in the past have employed lower-order (2^{nd} order in space) numerical schemes which require large number of grid points to capture with sufficient accuracy the unsteady vortical flow features associated with a low sweep delta wing. A preliminary study was carried out to study the flow over a delta wing.

Yen[73-75] made lot of contributions in the past to study the characteristics of a spiral shaped turbine. The idea was to develop a potential way to reduce the cost and broaden the usability of wind energy. The system uses a large hollow tower of the shape of a spiral to form an internal vortex. A commercial solver FLUENT[12] and an in-house solver MUSIC[65] were used to study the physics of such a system. Most of the current commercial CFD packages use the standard finite volume approach for discretizing the Euler and the Navier-Stokes equations and are capable of simulating complex large scale problems. In other words, the error decreases as O (Δx^2), with Δx being the mesh size, which is the case with the solvers used in the present study of tornado type wind turbine.

1.2 Thesis Outline

This thesis contains the work carried out in studying the Large Eddy Simulation (LES) of flow over a cylinder, flow over a delta wing and physics of a tornado type wind energy system. It is organized into different chapters – Chapter 2 gives a basic idea and formulation of the spectral difference method, Chapter 3 includes the computational details, geometry and numerical results for the flow over a cylinder, Chapter 4 discusses about the computational details and preliminary results for the flow over a delta wing and Chapter 5 talks about the tornado type wind energy system, solvers used and the results obtained. Chapters 3, 4 and 5 also discuss about the possible future work.

Chapter 2 - The Spectral Difference Method

2.1 Introduction

Computational Fluid Dynamics (CFD) has been used in solving various flow problems for more than three decades. The main area of concern has been the performance of numerical methods in CFD tools with respect to both reliability and accuracy. Extensive research efforts have led to the development of more accurate and reliable methods. Various research projects have been carried out in the last decade to develop and improve high order accurate algorithms for conservation laws. High-order methods capable of handling unstructured grids are highly sought after in many practical applications with complex geometries in LES, DNS of turbulence, computational aero-acoustics, to name a few. Discontinuous galerkin method[9,10] (DG), spectral volume method[41,66,68] (SV), and spectral difference method[28,39,40,67] (SD) are a few high-order schemes developed in the recent past. High-order methods are known not only for their accuracy but also for their potential to reduce the CPU time required to obtain the solutions. Most of the current calculations in computational aerodynamics, aero-acoustics and CFD are performed using methods that are at most 2nd order accurate. Even though second order methods have achieved successes, there exist several areas where their performance is unsatisfactory, e.g., for vortex-dominated flows including helicopter blade vortex interactions and flow over high lift configurations. Higher order methods are more successful in handling these flows.

Methods like Finite Difference (FD) and Finite Volume (FV) normally employ relatively low-order approximations in their formulations. But now we turn to spectral methods which have the properties of very high accuracy and spectral (or exponential) convergence[5,21]. In traditional spectral methods, the unknown variable is expressed as a truncated series expansion in terms of some basis functions (trial functions) and solved using the method weighted of residuals. The trial functions are infinitely differentiable global functions, and the most frequently used ones are trigonometric functions or Chebyshev and Legendre polynomials.

2.2 The Spectral Difference Method

The spectral difference (SD) method is a high-order, conservative, and efficient numerical method developed for conservation laws on unstructured grids. It combines the best features of structured and unstructured grid methods to attain computational efficiency and geometric flexibility. It utilizes the concept of discontinuous and high-order local representations to achieve conservation and high accuracy; and it is based on the FD formulation for simplicity.

The SD method is a type of finite-difference method or nodal spectral method for unstructured grids, in which inside each cell or element, there are structured nodal unknown and flux distributions, in such a way that the local integral conservation is satisfied. The conservative unknowns are defined at quadrature points. The unknowns are updated using the differential form of the conservation law by approximating the flux derivatives at those points. In order to obtain the flux derivatives, a polynomial reconstruction of the fluxes is used from their values at certain flux points. To evaluate the fluxes, the values of unknowns (and their gradients) at flux points are required. They are obtained from a reconstruction of unknowns using their values at unknown points. The reconstruction of fluxes is one order higher than that of unknowns.

In order to minimize the number of unknowns for a given accuracy, the unknowns are normally placed at Gauss quadrature points, while the fluxes are placed at Gauss-Lobatto quadrature points. By placing the unknowns and fluxes at the above quadrature points, one can obtain the spectral convergence and accuracy[5,30,33]. However in a recent study, Van den Abeele *et al*[60] found that the SD method does not depend on where the solution points are located, while the location of the flux points determines the method. Therefore, the solution points can be chosen to maximize efficiency. It was also found that the use of Chebyshev-Gauss-Lobatto points as the flux points results in a weak instability by Van den Abeele *et al*[60] and Huynh[29]. In the present study, the solution points are chosen to be the Chebyshev-Gauss points.

There are two important features of the method dealing with the relation of numerical solution in different cells. If the nodes are distributed in a geometrically similar manner for all cells, the discretizations become universal. The other feature concerns the fact that the flux at the surface points between two cells will in general be discontinuous. In order to have local and global conservations, certain flux components must be continuous. Therefore, the fluxes at those points are replaced with numerical fluxes. The numerical fluxes serve to couple the solutions in two neighboring cells and provide the necessary numerical dissipation to stabilize the numerical method.

The method is very simple to implement since it involves one-dimensional operations only, and does not involve any surface or volume integrals. The basic idea is presented next for the Navier-Stokes equations.

2.3 Formulation of the Spectral Difference Method on Hexahedral Grids

2.3.1 Governing equation

Consider the unsteady compressible three-dimensional Navier-Stokes equations in conservative form written as

$$\frac{\partial Q}{\partial t}+\frac{\partial F}{\partial x}+\frac{\partial G}{\partial y}+\frac{\partial H}{\partial z}=0 \qquad (2\text{-}1)$$

where Q is the vector of conserved variables, and F, G, H are the total fluxes including both the inviscid and viscous flux vectors, i.e., $F=F^i-F^v, G=G^i-G^v, H=H^i-H^v$, which take the following form

$$Q=\begin{Bmatrix}\rho\\ \rho u\\ \rho v\\ \rho w\\ E\end{Bmatrix},\quad F^i=\begin{Bmatrix}\rho u\\ p+\rho u^2\\ \rho uv\\ \rho uw\\ u(E+p)\end{Bmatrix},\quad G^i=\begin{Bmatrix}\rho v\\ \rho uv\\ p+\rho v^2\\ \rho vw\\ v(E+p)\end{Bmatrix},\quad H^i=\begin{Bmatrix}\rho w\\ \rho uw\\ \rho vw\\ p+\rho w^2\\ w(E+p)\end{Bmatrix} \qquad (2\text{-}2)$$

and

$$F^v=\begin{Bmatrix}0\\ \tau_{xx}\\ \tau_{yx}\\ \tau_{zx}\\ u\tau_{xx}+v\tau_{yx}+w\tau_{zx}+\dfrac{\mu C_P}{P_r}T_x\end{Bmatrix},$$

$$G^v = \begin{Bmatrix} 0 \\ \tau_{xy} \\ \tau_{yy} \\ \tau_{zy} \\ u\tau_{xy} + v\tau_{yy} + w\tau_{zy} + \frac{\mu C_P}{P_r} T_y \end{Bmatrix},$$

$$H^v = \begin{Bmatrix} 0 \\ \tau_{xz} \\ \tau_{yz} \\ \tau_{zz} \\ u\tau_{xz} + v\tau_{yz} + w\tau_{zz} + \frac{\mu C_P}{P_r} T_z \end{Bmatrix} \tag{2-3}$$

In equations 2-1 to 2-3, ρ is the density, u, v and w are the velocity components in x, y and z directions respectively, p is the pressure, E is the total energy, μ is the dynamic viscosity, C_P is the specific heat at constant pressure, P_r is the Prandtl number, and T is the temperature. For a perfect gas, the pressure is related the total energy by

$$E = \frac{p}{\gamma - 1} + \frac{1}{2}\rho\left(u^2 + v^2 + w^2\right), \tag{2-4}$$

with a constant ratio of specific heats γ, which is taken as 1.4 for air. The stress tensor in equation (2-3) takes the following form:

$$\tau_{xx} = 2\mu\left(u_x - \frac{1}{3}\left(u_x + v_y + w_z\right)\right) \tag{2-5a}$$

$$\tau_{yy} = 2\mu\left(v_y - \frac{1}{3}\left(u_x + v_y + w_z\right)\right) \tag{2-5b}$$

$$\tau_{zz} = 2\mu\left(w_z - \frac{1}{3}\left(u_x + v_y + w_z\right)\right) \tag{2-5c}$$

$$\tau_{xy} = \tau_{yx} = \mu\left(v_x + u_y\right) \tag{2-5d}$$

$$\tau_{yz} = \tau_{zy} = \mu\left(w_y + v_z\right) \qquad (2\text{-}5e)$$

$$\tau_{xz} = \tau_{zx} = \mu\left(u_z + w_x\right) \qquad (2\text{-}5f)$$

2.3.2 Coordinate transformation

Non-overlapping unstructured hexahedral cells or elements are employed to fill the computational domain. The use of hexahedral cells for viscous boundary layers is preferred over tetrahedral cells because of the efficiency and accuracy. In order to handle curved boundaries, both linear and quadratic isoparametric elements are employed, with linear elements used in the interior domain and quadratic elements near high-order curved boundaries. All the elements are transformed from the physical domain (x, y, z) into a standard cubic element $(\xi, \eta, \zeta) \in [0,1] \times [0,1] \times [0,1]$ as shown in Figure 2-1. The transformation can be written as

$$\begin{pmatrix} x \\ y \\ z \end{pmatrix} = \sum_{i=1}^{K} M_i(\xi, \eta, \zeta) \begin{pmatrix} x_i \\ y_i \\ z_i \end{pmatrix}, \qquad (2\text{-}6)$$

where K is the number of points used to define the physical element, (x_i, y_i, z_i) are the Cartesian coordinates of those points, and $M_i(\xi, \eta, \zeta)$ are the shape functions.

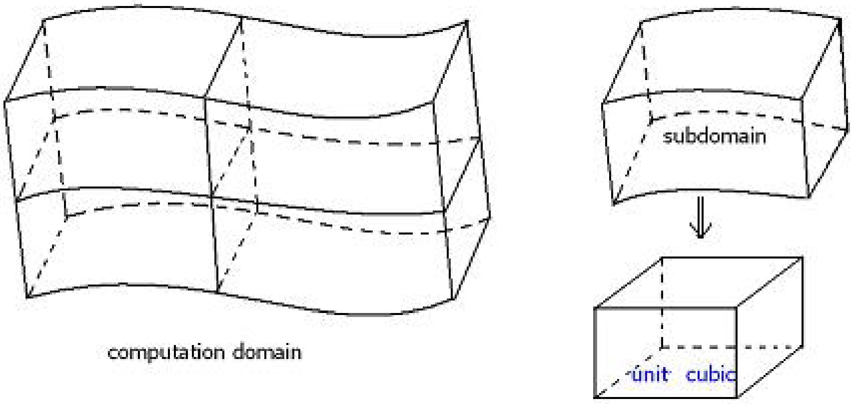

Figure 2-1 Transformation from a physical element to a standard element[55]

For the transformation given in Equation 2-6, the Jacobian matrix J takes the following form

$$J = \frac{\partial(x,y,z)}{\partial(\xi,\eta,\zeta)} = \begin{bmatrix} x_\xi & x_\eta & x_\zeta \\ y_\xi & y_\eta & y_\zeta \\ z_\xi & z_\eta & z_\zeta \end{bmatrix}. \tag{2-7}$$

For a non-singular transformation, its inverse transformation must also exist, and the Jacobian matrices are related to each other according to

$$\frac{\partial(\xi,\eta,\zeta)}{\partial(x,y,z)} = \begin{bmatrix} \xi_x & \xi_y & \xi_z \\ \eta_x & \eta_y & \eta_z \\ \zeta_x & \zeta_y & \zeta_z \end{bmatrix} = J^{-1}. \tag{2-8}$$

Therefore the metrics can be computed according to

$$\xi_x = \frac{(y_\eta z_\zeta - y_\zeta z_\eta)}{|J|}, \xi_y = \frac{(x_\zeta z_\eta - x_\eta z_\zeta)}{|J|}, \xi_z = \frac{(x_\eta y_\zeta - x_\zeta y_\eta)}{|J|} \tag{2-9a}$$

$$\eta_x = \frac{(y_\zeta z_\xi - y_\xi z_\zeta)}{|J|}, \eta_y = \frac{(x_\xi z_\zeta - x_\zeta z_\xi)}{|J|}, \eta_z = \frac{(x_\zeta y_\xi - x_\xi y_\zeta)}{|J|} \tag{2-9b}$$

$$\zeta_x = \frac{(y_\xi z_\eta - y_\eta z_\xi)}{|J|}, \zeta_y = \frac{(x_\eta z_\xi - x_\xi z_\eta)}{|J|}, \zeta_z = \frac{(x_\xi y_\eta - x_\eta y_\xi)}{|J|} \tag{2-9c}$$

The governing equations in the physical domain are then transformed into the computational domain (standard element), and the transformed equations take the following form

$$\frac{\partial \tilde{Q}}{\partial t} + \frac{\partial \tilde{F}}{\partial \xi} + \frac{\partial \tilde{G}}{\partial \eta} + \frac{\partial \tilde{H}}{\partial \zeta} = 0 \tag{2-10}$$

where

$$\tilde{Q} = |J| \cdot Q$$

$$\tilde{F} = \tilde{F}^i - \tilde{F}^v, \tilde{G} = \tilde{G}^i - \tilde{G}^v, \tilde{H} = \tilde{H}^i - \tilde{H}^v.$$

$$\begin{bmatrix} \widetilde{F}^i \\ \widetilde{G}^i \\ \widetilde{H}^i \end{bmatrix} = |J| \begin{bmatrix} \xi_x & \xi_y & \xi_z \\ \eta_x & \eta_y & \eta_z \\ \zeta_x & \zeta_y & \zeta_z \end{bmatrix} \cdot \begin{bmatrix} F^i \\ G^i \\ H^i \end{bmatrix} \qquad \begin{bmatrix} \widetilde{F}^v \\ \widetilde{G}^v \\ \widetilde{H}^v \end{bmatrix} = |J| \begin{bmatrix} \xi_x & \xi_y & \xi_z \\ \eta_x & \eta_y & \eta_z \\ \zeta_x & \zeta_y & \zeta_z \end{bmatrix} \cdot \begin{bmatrix} F^v \\ G^v \\ H^v \end{bmatrix}$$

Let $\vec{S}_\xi = |J|(\xi_x, \xi_y, \xi_z)$, $\vec{S}_\eta = |J|(\eta_x, \eta_y, \eta_z)$ and $\vec{S}_\zeta = |J|(\zeta_x, \zeta_y, \zeta_z)$.

Then, finally $\widetilde{F} = \vec{f}.S_\xi, \widetilde{G} = \vec{f}.S_\eta$, $\widetilde{H} = \vec{f}.S_\zeta$ with $\vec{f} = (F, G, H)$. In the implementation, $|J|$ is stored at the solution points, while $\vec{S}_\xi, \vec{S}_\eta, \vec{S}_\zeta$ are stored at flux points to minimize memory usage.

2.3.3 Spatial discretization

In a standard element, two sets of points are defined, namely the solution points and the flux points, illustrated in Figure 2-2 for 2D. The solution unknowns or degrees-of-freedom (DOFs) are the conserved variables at the solution points, while fluxes are computed at the flux points in order to update the solution unknowns. In order to construct a degree *(N-1)* polynomial in any direction, solutions at *N* points are required.

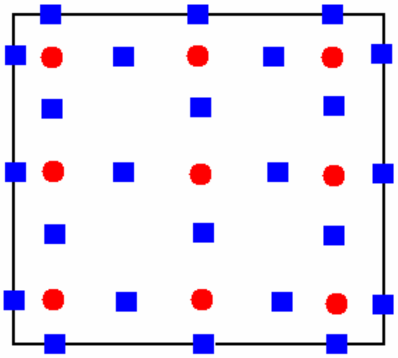

Figure 2-2 Distribution of solution points (circles) and flux points (squares) in a standard element for a 3rd order SD scheme[55]

As mentioned earlier, Van den Abeele *et al*[60] found that the SD method does not depend on where the solution points are located, while the location of the flux points determines the method. In the current work, the solution points are chosen to be the Chebyshev-Gauss points defined by

$$X_s = \frac{1}{2}\left[1-\cos\left(\frac{2s-1}{2N}\cdot\pi\right)\right], \quad s=1,2,\ldots,N\,. \qquad (2\text{-}11)$$

The flux points are selected to be the Legendre-Gauss-quadrature points plus the two end points, 0 and 1, as suggested by Huynh[29]. Using the N solutions at the solution points, a degree *N-1* polynomial can be built using the following Lagrange basis defined as

$$h_i(X) = \prod_{s=1,s\neq i}^{N}\left(\frac{X-X_s}{X_i-X_s}\right). \qquad (2\text{-}12)$$

Similarly, using the $N+1$ fluxes at the flux points, a degree N polynomial can be built for the flux using a similar Lagrange basis defined as

$$l_{i+1/2}(X) = \prod_{s=0,s\neq i}^{N}\left(\frac{X-X_{s+1/2}}{X_{i+1/2}-X_{s+1/2}}\right). \qquad (2\text{-}13)$$

The reconstructed solution for the conserved variables in the standard element is just the tensor products of the three one-dimensional polynomials, i.e.,

$$Q(\xi,\eta,\varsigma) = \sum_{k=1}^{N}\sum_{j=1}^{N}\sum_{i=1}^{N}\frac{\widetilde{Q}_{i,j,k}}{\left|J_{i,j,k}\right|}\, h_i(\xi)\cdot h_j(\eta)\cdot h_k(\varsigma)\,.$$

Similarly, the reconstructed flux polynomials take the following forms:

$$\widetilde{F}(\xi,\eta,\varsigma) = \sum_{k=1}^{N}\sum_{j=1}^{N}\sum_{i=0}^{N}\widetilde{F}_{i+1/2,j,k}\; l_{i+1/2}(\xi)\cdot h_j(\eta)\cdot h_k(\varsigma)\,, \qquad (2\text{-}14a)$$

$$\widetilde{G}(\xi,\eta,\varsigma) = \sum_{k=1}^{N}\sum_{j=0}^{N}\sum_{i=1}^{N}\widetilde{G}_{i,j+1/2,k}\; h_i(\xi)\cdot l_{j+1/2}(\eta)\cdot h_k(\varsigma)\,, \qquad (2\text{-}14b)$$

$$\widetilde{H}(\xi,\eta,\varsigma) = \sum_{k=0}^{N}\sum_{j=1}^{N}\sum_{i=1}^{N}\widetilde{H}_{i,j,k+1/2}\; h_i(\xi)\cdot h_j(\eta)\cdot l_{k+1/2}(\varsigma)\,. \qquad (2\text{-}14c)$$

The reconstructed fluxes are only element-wise continuous, but discontinuous across cell interfaces. For the inviscid flux, a Riemann solver, such as the Rusanov or Roe flux, is employed to compute a common flux at interfaces to ensure conservation and stability. In summary, the algorithm to compute the inviscid flux derivatives consists of the following steps:

1. Given the conserved variables at the solution points $\left\{\widetilde{Q}_{i,j,k}\right\}$, compute the conserved variables at the flux points
2. Compute the inviscid fluxes at the interior flux points using the solutions computed at Step 1

3. Compute the inviscid flux at element interfaces using a Riemann solver, in terms of the left and right conserved variables of the interface.
4. Compute the derivatives of the fluxes at all the solution points according to

$$\left(\frac{\partial\widetilde{F}}{\partial\xi}\right)_{i,j,k}=\sum_{r=0}^{N}\widetilde{F}_{r+1/2,j,k}\cdot l'_{r+1/2}(\xi_i)\,, \qquad (2\text{-}15a)$$

$$\left(\frac{\partial\widetilde{G}}{\partial\eta}\right)_{i,j,k}=\sum_{r=0}^{N}\widetilde{G}_{i,r+1/2,k}\cdot l'_{r+1/2}(\eta_j)\,, \qquad (2\text{-}15b)$$

$$\left(\frac{\partial\widetilde{H}}{\partial\varsigma}\right)_{i,j,k}=\sum_{r=0}^{N}\widetilde{H}_{i,j,r+1/2}\cdot l'_{r+1/2}(\varsigma_k)\,. \qquad (2\text{-}15c)$$

The viscous flux is a function of both the conserved variables and their gradients, e.g., $\widetilde{F}^{v}_{i+1/2,j,k}=\widetilde{F}^{v}(Q_{i+1/2,j,k},\nabla Q_{i+1/2,j,k})$. Therefore the key is how to compute the solution gradients at the flux points. The following steps are taken to compute the viscous fluxes:

1. Same as Step 1 for the inviscid flux computations;
2. When computing the derivatives, the solution Q at the cell interface is not uniquely defined. The solution at the interface is simply the average of the left and right solutions, $\hat{Q}=(Q_L+Q_R)/2$.
3. Compute the gradients of the solution at the solution points using the solutions at the flux points. Then the gradients are interpolated from the solution points to the flux points using the same Lagrangian interpolation approach given in.
4. Compute the viscous flux at the flux points using the solutions and their gradients at the flux points. Again at cell interfaces, the gradients have two values, one from the left and one from the right. The gradients used in the viscous fluxes at the cell interface are simply the averaged ones, i.e., $\widetilde{F}^{v}=\widetilde{F}^{v}((Q_L+Q_R)/2,(\nabla Q_L+\nabla Q_R)/2)$.

Once all fluxes are computed at the flux points, the flux polynomials are built according to Equation 2-14, and the derivatives of the fluxes are then evaluated at each solution point to update the DOFs, i.e.,

$$\frac{\partial\widetilde{Q}}{\partial t}=-\left(\frac{\partial\widetilde{F}}{\partial\xi}+\frac{\partial\widetilde{G}}{\partial\eta}+\frac{\partial\widetilde{H}}{\partial\zeta}\right)_{i,j,k} \qquad (2\text{-}16)$$

More details of the SD method can be found in References 55 and 56.

The potential of spectral difference method in vortex-dominated flows is demonstrated in the case of flow over a circular cylinder and flow over a delta wing, discussed in chapters 3 and 4 to follow.

Chapter 3 – Large Eddy Simulation of Flow over a Cylinder

3.1 Introduction

The flow around bluff bodies is very complex and can involve regions of laminar, transitional and turbulent flows, unsteady separation and reattachment, and the formation of coherent structures, particularly in the wake region of the flow. The understanding of bluff body vortex shedding is of great practical importance and the uniform flow over a circular cylinder is a classical example of bluff body flow. The configuration is quite simple but the flow is characterized by a very complex wake at Reynolds number Re_D=2580 examined in the current work. The importance of using high order methods to study the numerical and physical aspect of unsteady wake flow involving separation, recirculation, unsteady vortex shedding and large complex flow structures at a sub-critical Reynolds number is shown. The near wake structure behind a bluff body plays an important role in the overall vortex formation and shedding processes and determines the magnitude of mean and fluctuating forces exerted on the body. Direct numerical simulations (DNS) of the Navier-Stokes equations, in which all eddy scales have to be captured, is almost impossible for problems with moderately high Reynolds number because of the huge computational requirements in resolving all turbulence scales. Hence a less expensive and accurate method is required. In Reynolds averaged Navier-Stokes (RANS) approach, all eddies are averaged over to give equations for variables representing the mean flow. But RANS has proved to be generally inadequate in predicting the effects of turbulent separating and reattaching flows, because the large eddies responsible for the primary transport are geometry dependent. For any turbulent flow, the largest scale is of the order of the domain size and the small scales are related to the dissipative eddies where the viscous effects become predominant. Large eddy simulation (LES) is a method where the three-dimensional and unsteady motion of the large eddies is computed explicitly and the non-linear interactions with the smaller eddies, which are assumed to be isotropic and universal, are modeled. LES is an active area of research and the numerical simulation of complex flows is essential in the development of the method as a tool to predict flows of engineering interest.

In the current work, implicit LES computations were performed without any sub-grid scale model in order to investigate the effectiveness of the spectral difference method. These simulations were deliberately not called direct numerical simulations because they did not comply with the resolution requirements of DNS. Turbulent flow past a circular cylinder has been the subject of a large number of experimental and numerical investigations[54,70]. In recent years a good understanding of the physics of flow at low Reynolds number of below a few hundred, has been obtained. But at higher Reynolds number, still subcritical though, considerably less is known. A comprehensive review of the flow characteristics for a wide range of Reynolds numbers was studied by Williamson[69]. In addition, a number of simulations at various Reynolds numbers, mostly LES, have been carried out[6,59]. The cylinder flow at Reynolds number Re_D=3900 has become a common test case for LES primarily because of the availability of the experimental results of Lourenco and Shih[36] and Ong and Wallace[51]. The calculations were performed on structured[2,4,35,45] and unstructured meshes[15,26,42]. Beaudan and Moin[2], Mittal and Moin[45], Kravchenko and Moin[34] were among the first to perform LES studies at Re_D=3900. Motivated by the direct simulation results of Rai and Moin[52], Beaudan and Moin[2] used high-order upwind-biased schemes for the numerical simulations of the compressible Navier–Stokes equations. The profiles of mean velocity and Reynolds stresses obtained in these simulations were in reasonable agreement with the experimental data. However, inside the recirculation region, the streamwise velocity profiles differed in shape from those observed in the experiment[36]. These differences were attributed to the experimental errors as manifested in the large asymmetry of the experimental data[2]. A new experiment at the same Reynolds number was carried out by Ong and Wallace[51] and provided the mean flow data at several locations in the near wake of the cylinder downstream of the recirculation region. Even though fair agreement between the simulations of Beaudan and Moin[2] and the experiment was observed in the mean velocity profiles, turbulence intensities at several downstream locations did not match the experimental data. Also the Reynolds stresses were not predicted correctly when compared to experimental data. Similar problems were observed with Mittal and

Moin's work[35,45]. In the two mentioned simulations, they showed a shape of the streamwise velocity profile inside the recirculation region different from that observed in the experiment of Laurenco and Shih[36]. A new experiment at the same Reynolds number was carried out by Ong and Wallace[51] and provided the mean flow data at several locations in the near wake of the cylinder downstream of the recirculation region. Even though fair agreement between the simulations of Beaudan and Moin[2] and the experiment was observed in the mean velocity profiles, turbulence intensities at several downstream locations did not match the experimental data. Several other researchers have examined a variety of aspects that affect the quality of LES solutions at Re_D=3900. The numerical and modeling aspects which influence the quality of LES solutions were studied by Breuer[3]. He had also carried out LES computations without any sub-grid scale model.

DNS of the cylinder flow at Re_D=3900 was performed by Ma *et al.*[42]. The mean velocity profiles and the power spectra are in good agreement with the experimental data in the near wake as well as far downstream. In particular, the velocity profiles agree well with those from the experiments in the vicinity of the cylinder. Compared with LES[35], the pressure coefficient in DNS is a little lower, while the recirculation bubble length is larger. Franke and Frank[13] found out that this is an effect of the averaging time in computing statistics. In DNS[42] the statistics is accumulated over 600 convective time units (D/U), while in LES[35] the statistics is accumulated over 35 convective time units. The numerical issues raised in the previous large eddy simulations prompted us to attempt simulations of the flow over a circular cylinder using a high order method. Second-order simulations for unperturbed inlet flow conditions at Re_D=2580 were performed by Liang[38]. The length of the recirculation bubble was under predicted probably due to under-resolution. The primary motivation for using a high order method is to accurately study the wake flow at Reynolds number Re_D=2580. The numerical results obtained were compared with the PIV experiment performed by Konstantinidis *et al.*[31].

3.2 Problem Definition and Computational Details

The simulation was performed to match the geometry of the experiment performed by Konstantinidis *et al*[31]. The experiments were performed using the PIV technique in a stainless steel water tunnel with a cross-section of 72mm x 72mm. The origin and size of the computational domain are shown in Figure 3-1. The x-axis is along the streamwise flow direction and the z-axis is along the cylinder axis i.e. the spanwise direction. The cylinder has a non-dimensional unit diameter. The upstream velocity is fixed at U=0.1 m/s and is assumed to be uniform across the inlet. The Reynolds number based on the cylinder diameter and upstream velocity is 2580.

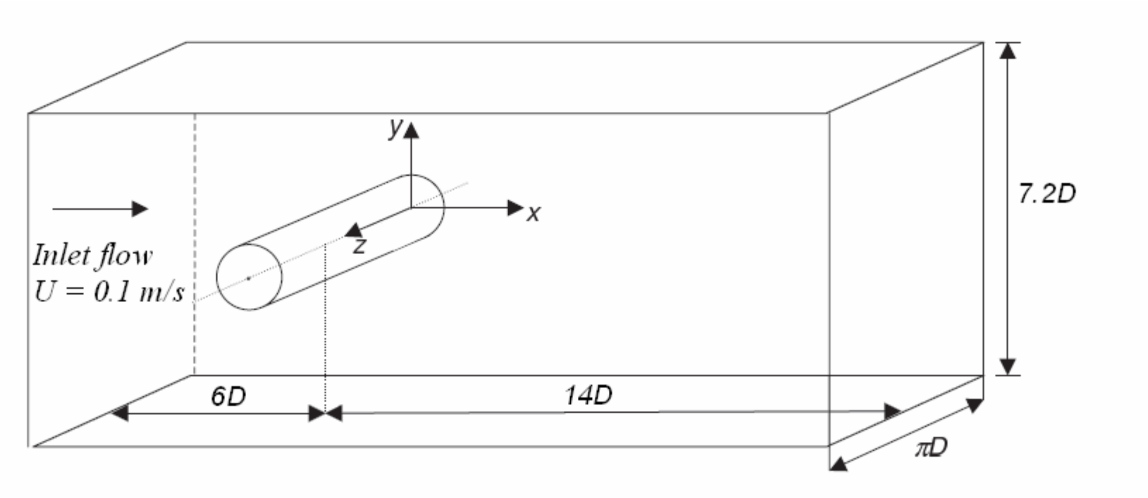

Figure 3-1 The geometry of the flow over cylinder

The size of the computational domain in the y-direction is equal to 7.2 cylinder diameters, which is equal to the one used in the experiment. The required size in the spanwise direction is estimated from the prior knowledge of the sizes of the streamwise vortex structures. It has been reported in the experimental studies by Mansy *et al.*[43] and Williamson *et al.*[71] that the wavelength of the streamwise structures in the near wake of a circular cylinder scale as

$$\lambda_z/D \sim 25\, Re_D^{-0.5} \tag{3-1}$$

For the present case of Re_D=2580, the wavelength is approximately 0.5D. Further downstream, large scale structures were observed by Williamson *et al.*[71] with wavelengths $\lambda_z/D \sim 1$. No experimental information was available about the size of streamwise structures, so the length of the domain in the spanwise direction is taken to be πD which is the same as the one used by Kravchenko and Moin[35], and Breuer[4].

High-order spectral difference method is employed to solve the problem. Implicit scheme with 2nd order accuracy in time was used. Both 2nd and 3rd orders of spatial accuracy were tested with quadratic boundary for the cylinder surface. Although the explicit scheme is easy to implement and has high-order accuracy in time, it suffered from too small time step, especially for viscous grids which are clustered in the viscous boundary layer. It is well-known that high-order methods are restricted to a smaller CFL number than low order ones. In addition, they also possess much less numerical dissipation. The computation cost of high-order explicit methods for many steady-state problems is so high that they become less efficient than low-order implicit methods in terms of the total CPU time given the same level of solution error. Therefore an efficient implicit lower-upper symmetric Gauss-Seidel (LU-SGS)[7,76] solution algorithm is used to solve viscous compressible flows for the high order spectral difference method on unstructured hexahedral grids.

As shown in Figure 3-2 and Figure 3-3, two meshes are used. The coarse mesh has 86,680 cells and the fine mesh has 189,448 cells. For third order spatial accuracy, the coarse mesh has 2.34 million degrees-of-freedom (DOFs) while the fine mesh has 5.12 million DOFs. The fine mesh is produced by refining the coarse mesh by about 1.5 times in the wake region of the cylinder.

As mentioned earlier, the length of the domain in the spanwise direction is πD and 12 layers are used for coarse mesh while 18 layers are used for the fine mesh. A constant expansion of 1.1 was used in the radial direction away from the cylinder. The smallest cell spacing in the radial direction is $\Delta r_{min}/D = 1.75 \times 10^{-3}$ for the fine mesh and 3.5×10^{-3} for the coarse mesh. Beaudan and Moin[2] had used a slightly lower value of $\Delta r_{min}/D = 1.25 \times 10^{-3}$ for their finest mesh at Re_D=3900. Therefore the mesh used is coarser than the finest mesh used by Beaudan and Moin[2]. In every layer in the spanwise direction, 120 cells were placed along the circumference of the cylinder for coarse mesh while 160 for fine mesh which is lower than the ones used by Liang[38] at Re_D=2580. The time step (normalized $\Delta T = tU/D$) used is 0.005 for the coarse mesh while for the fine mesh it is half of the one used for the coarse mesh. It takes roughly 4 to 5 sub-iterations for the unsteady residual to drop by two orders. A far-field boundary condition is used at the inlet with an unperturbed inlet flow velocity. At the outlet, a fixed pressure boundary condition is used. Periodic boundary condition is applied in the spanwise direction while symmetry is imposed for the top and bottom surfaces. Zero velocity boundary condition is used for the cylinder wall.

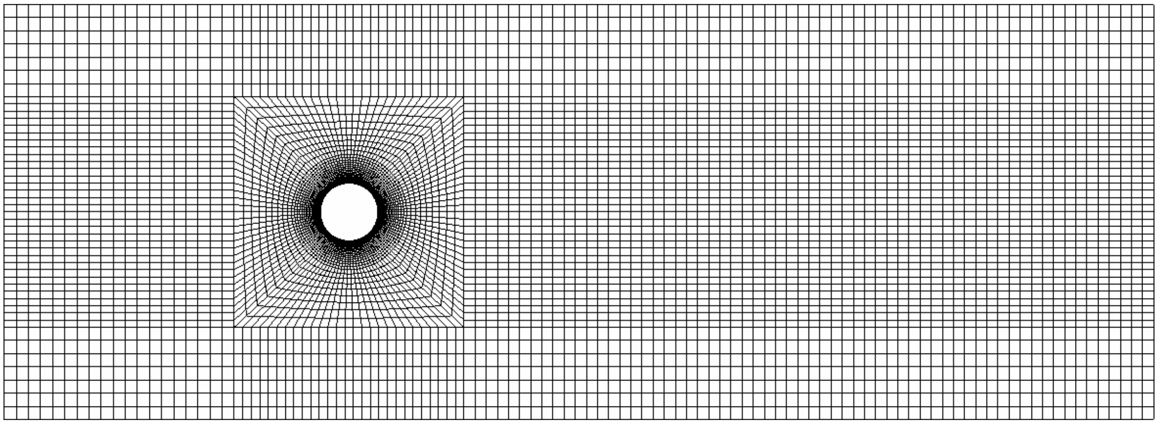

Figure 3-2 Coarse mesh in X-Y plane

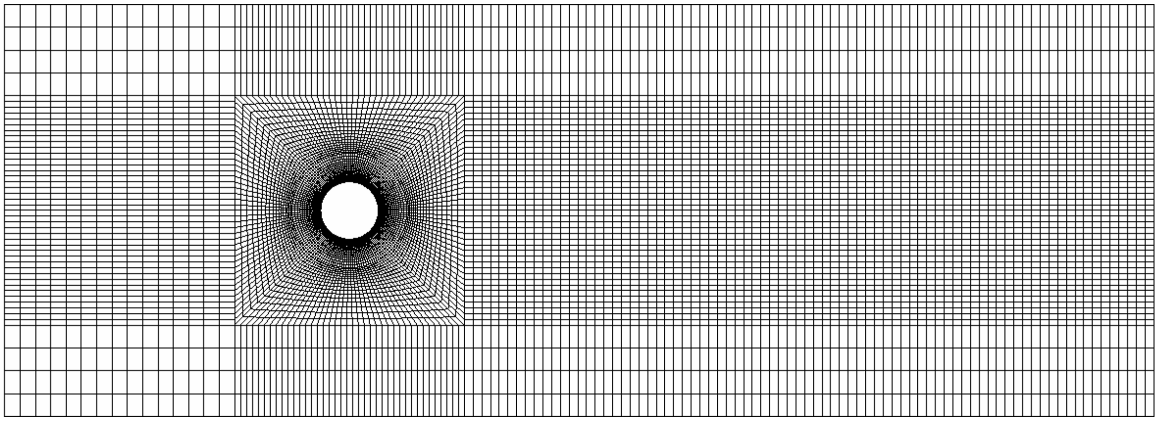

Figure 3-3 Fine mesh in X-Y plane

The flow over the cylinder is first allowed to reach a statistically steady state so as to allow all transients to exit the computational domain and then the statistics, mean and r.m.s. values, were obtained. The transients are convected out using 12 shedding periods and then 20 shedding periods are used to collect the statistics of mean and r.m.s. values.

3.3 Numerical Results and Discussion

The instantaneous streamwise, transverse and spanwise velocities in the wake of the circular cylinder are shown in Figures 3-4, 3-5 and 3-6. Figure 3-4 clearly shows the unsteady recirculation region. The alternating regions of positive and negative transverse velocity corresponding to the Karman vortices can also be observed in Figure 3-5. At Re_D=2580, the flow becomes turbulent and three-dimensional which is evident of the presence of both the small and large scale structures in Figure 3-6. It also shows that the flow structures increase in size as we go downstream of the cylinder. It can be noted that small scale structures are still present very far away from the cylinder which were not observed by Beaudan and Moin[2]. Moser *et al.*[48] performed a DNS and could capture the small scale and large scale turbulent structures at Re_D=2000.

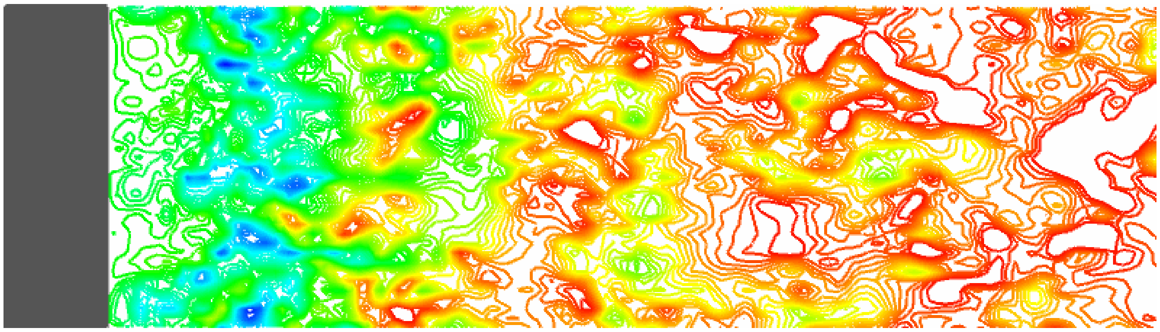

Figure 3-4 Instantaneous streamwise velocity in x-z plane (y=0) in the wake of the cylinder. There are 40 contours from -0.1 to 0.1.

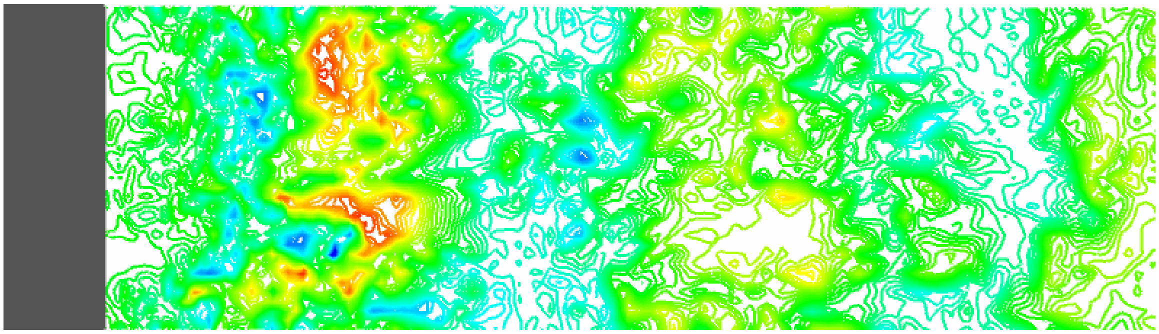

Figure 3-5 Instantaneous transverse velocity in x-z plane (y=0) in the wake of the cylinder. There are 40 contours from -0.1 to 0.1.

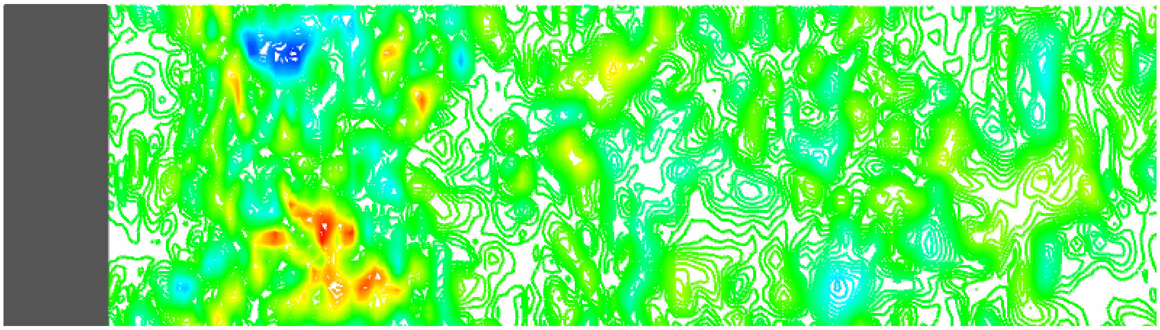

Figure 3-6 Instantaneous spanwise velocity in x-z plane (y=0) in the wake of the cylinder. There are 52 contours from -0.1 to 0.1.

Figure 3-7 shows contours of instantaneous vorticity magnitude. Two long shear layers can be seen separating from the cylinder. The Karman vortex street can also be seen in Figure 3-7. The vortices arising from the instabilities of the shear layers mix in the primary Karman vortices before propagating downstream and similar observations were made by Chyu and Rockwell[26] in their PIV experiments. Figure 3-8 shows the iso-surfaces of z-vorticity in the wake of the cylinder.

A study on grid independency is made for the coarse and fine mesh since insufficient grid resolution can lead to inaccurate predictions of the wake characteristics[35]. Figure 3-9 shows that the second order method cannot capture the statistics accurately. Contours for Mach number are shown in Figure 3-10. It can be clearly seen that the 2nd order results predict a smaller re-circulation region when compared to 3rd order. Figures 3-9 and 3-10 show the incapability of second order scheme to predict the flow accurately. On the other hand, the coarse mesh results with third order accuracy are in fairly good agreement with the experiment results. Figure 3-11 and Figure 3-12 show that 3rd order results are in excellent agreement with the experiment (PIV) measurements for the mean streamwise and transverse velocity at various locations in the wake of the cylinder for both fine mesh and coarse mesh. The statistics obtained from both fine and coarse meshes are pretty similar but the fine mesh gives slightly better results. It can be seen in Figures 3-11 and 3-12 that, at x/D=1.5, 2 and 2.5, both the mean streamwise and mean transverse velocities are slightly over predicted for the coarse mesh. But the fine mesh results give a good agreement with the experiment values. This can clearly be seen in Figure 3-13 and 3-14, where the fine mesh gives a very good prediction of the physics of the flow even far downstream.

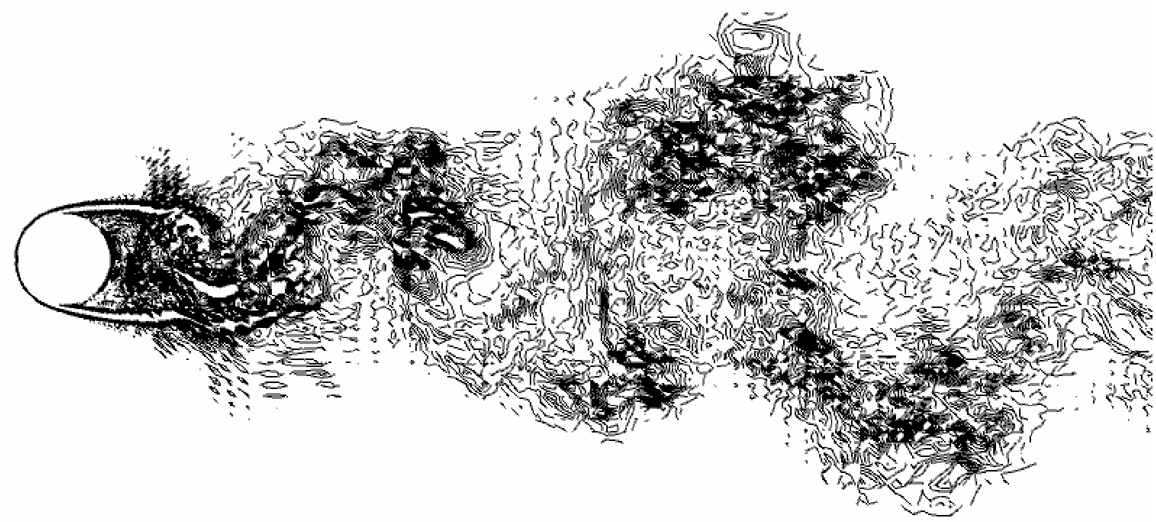

Figure 3-7 Instantaneous vorticity magnitude showing 16 contours from ωD/U = -0.1 to ωD/U = 0.1.

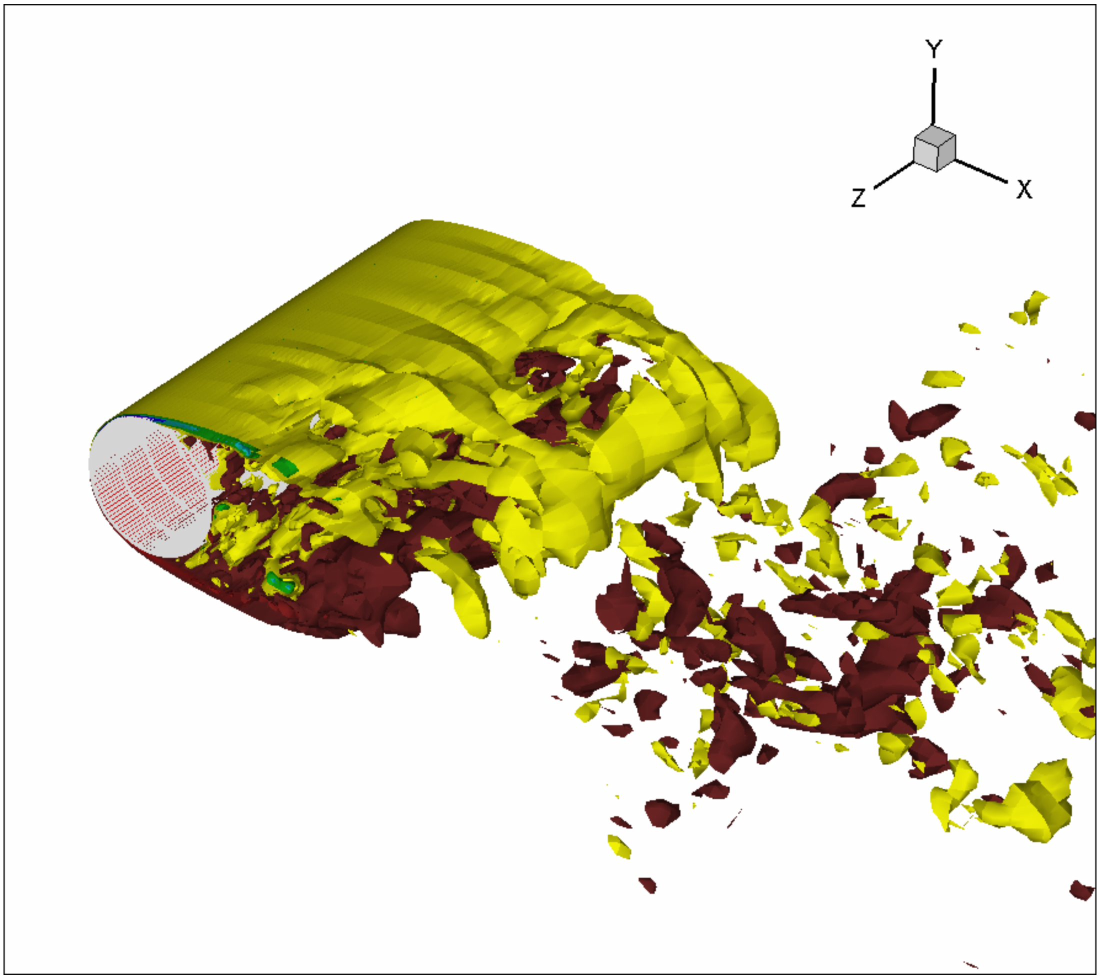

Figure 3-8 Iso-surface of z-vorticity. There are 16 surfaces from -5 to 5.

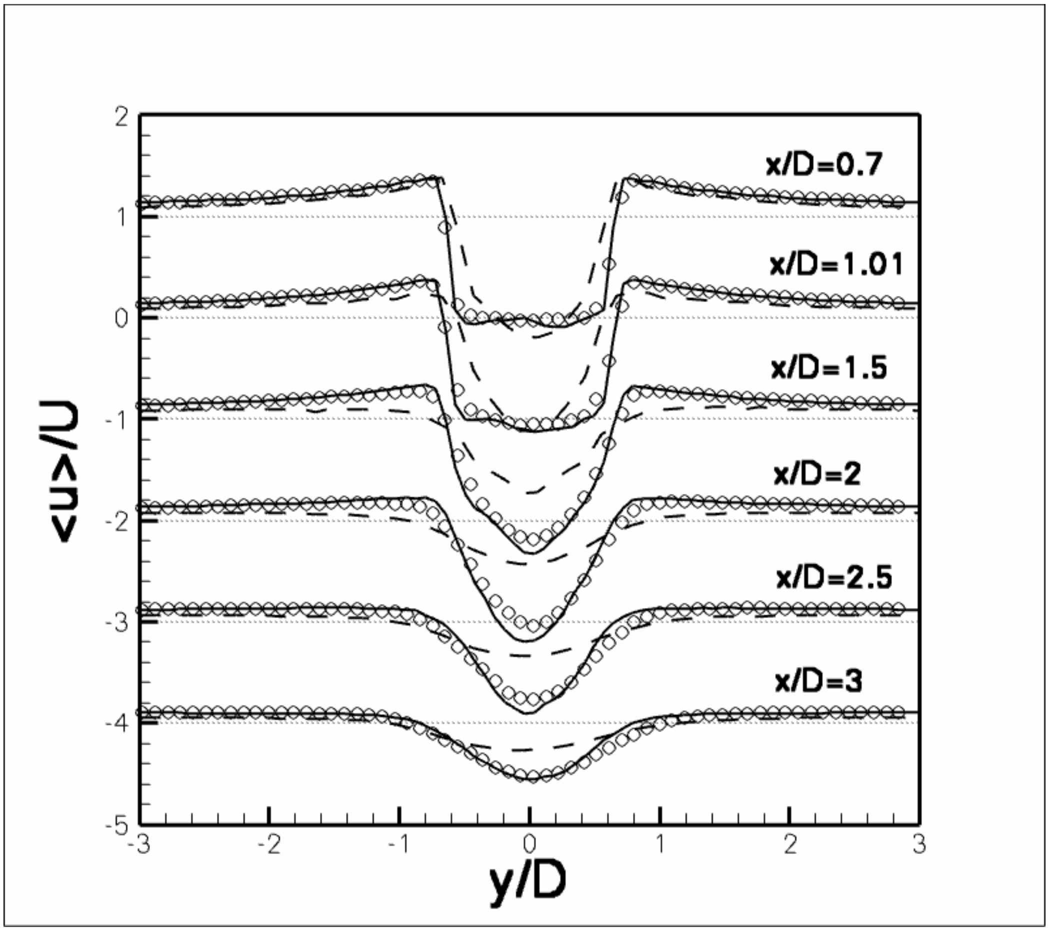

Figure 3-9 Mean normalized streamwise velocity in the wake of the circular cylinder, (oooo) - experiment; (Dashed line) – 2nd order results; (Solid line) – 3rd order results. The dotted line (......) represents the zero location of the shifted curves.

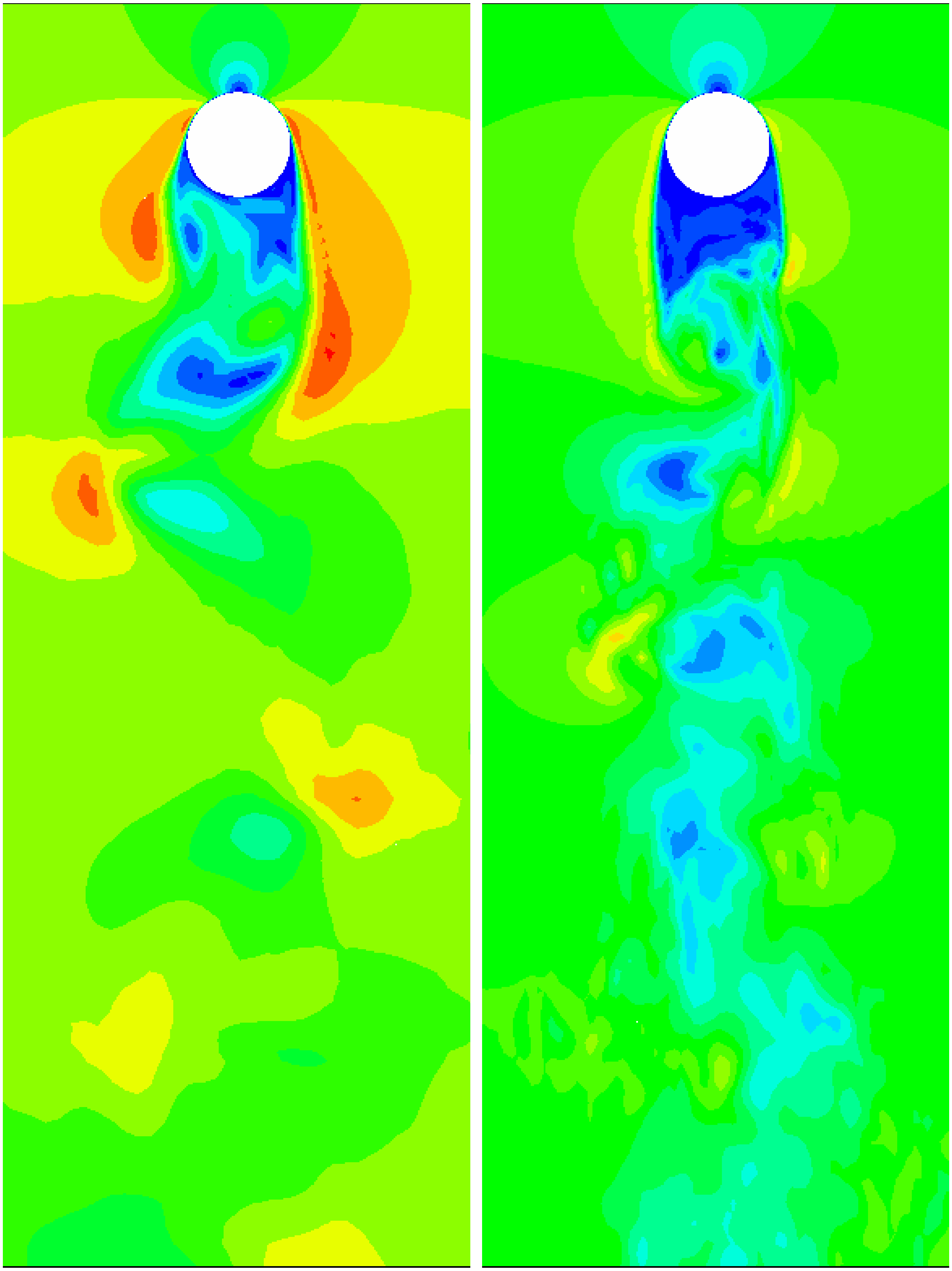

(a) (b)

Figure 3-10 Mach number in x-y plane for the coarse mesh. (a) 2^{nd} order; (b) 3^{rd} order. There are 14 contours from 0.01 to 0.14.

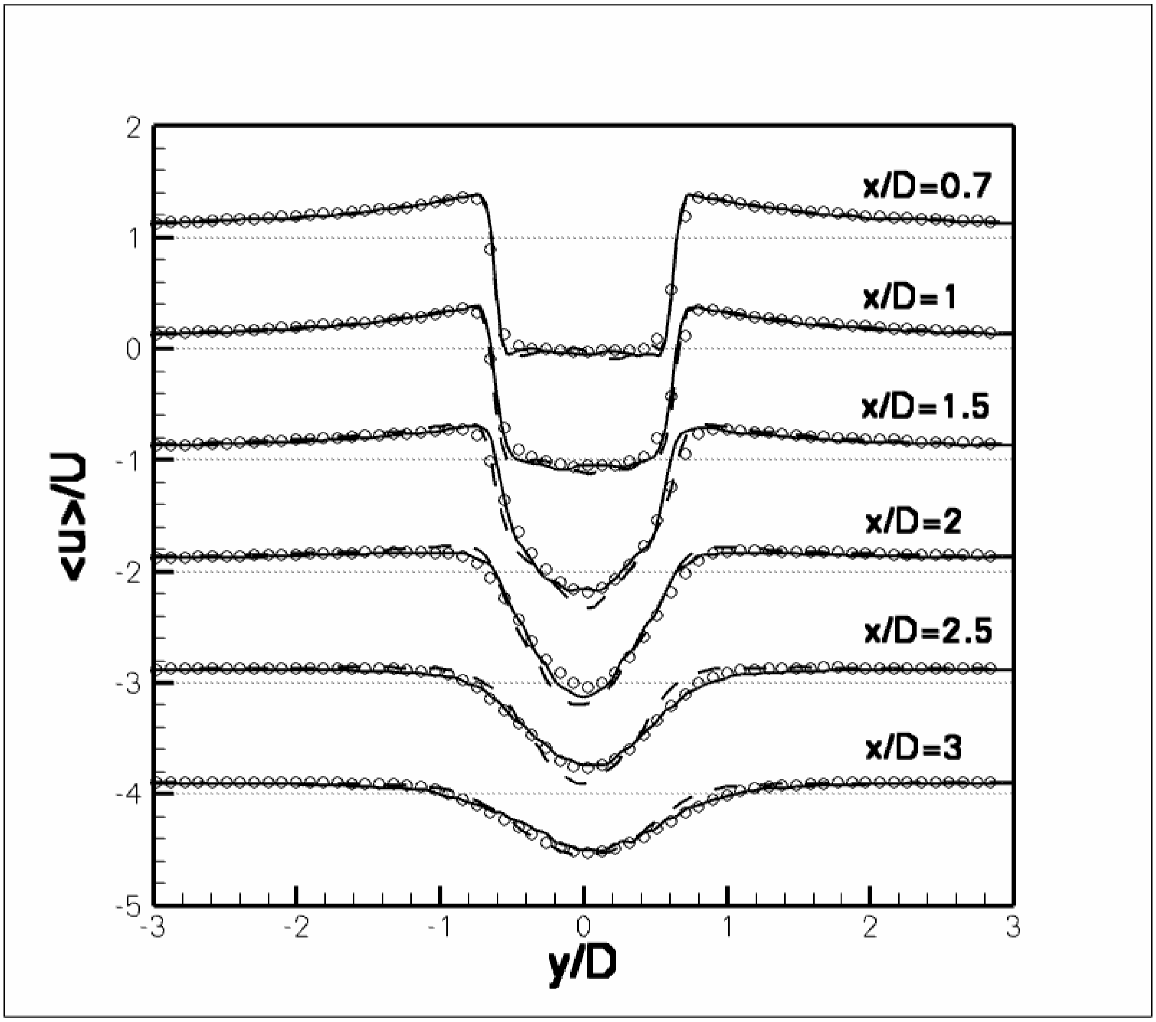

Figure 3-11 Mean normalized streamwise velocity in the wake of the circular cylinder, (oooo) - experiment; (Dashed line) – coarse mesh; (Solid line) – fine mesh. The dotted line (......) represents the zero location of the shifted curves.

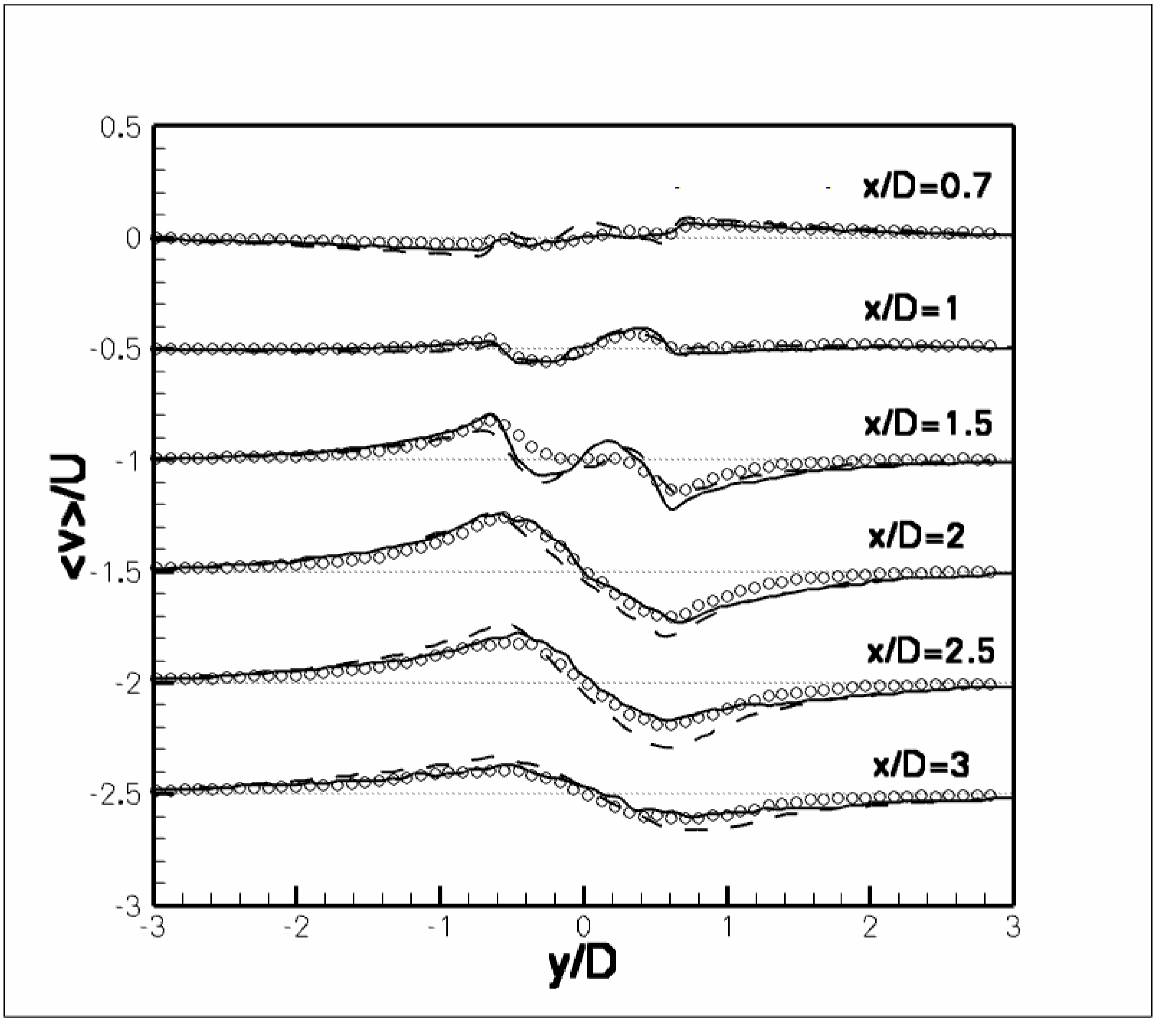

Figure 3-12 Mean normalized transverse velocity in the wake of the circular cylinder, (oooo) - experiment; (Dashed line) – coarse mesh; (Solid line) – fine mesh. The dotted line (......) represents the zero location of the shifted curves.

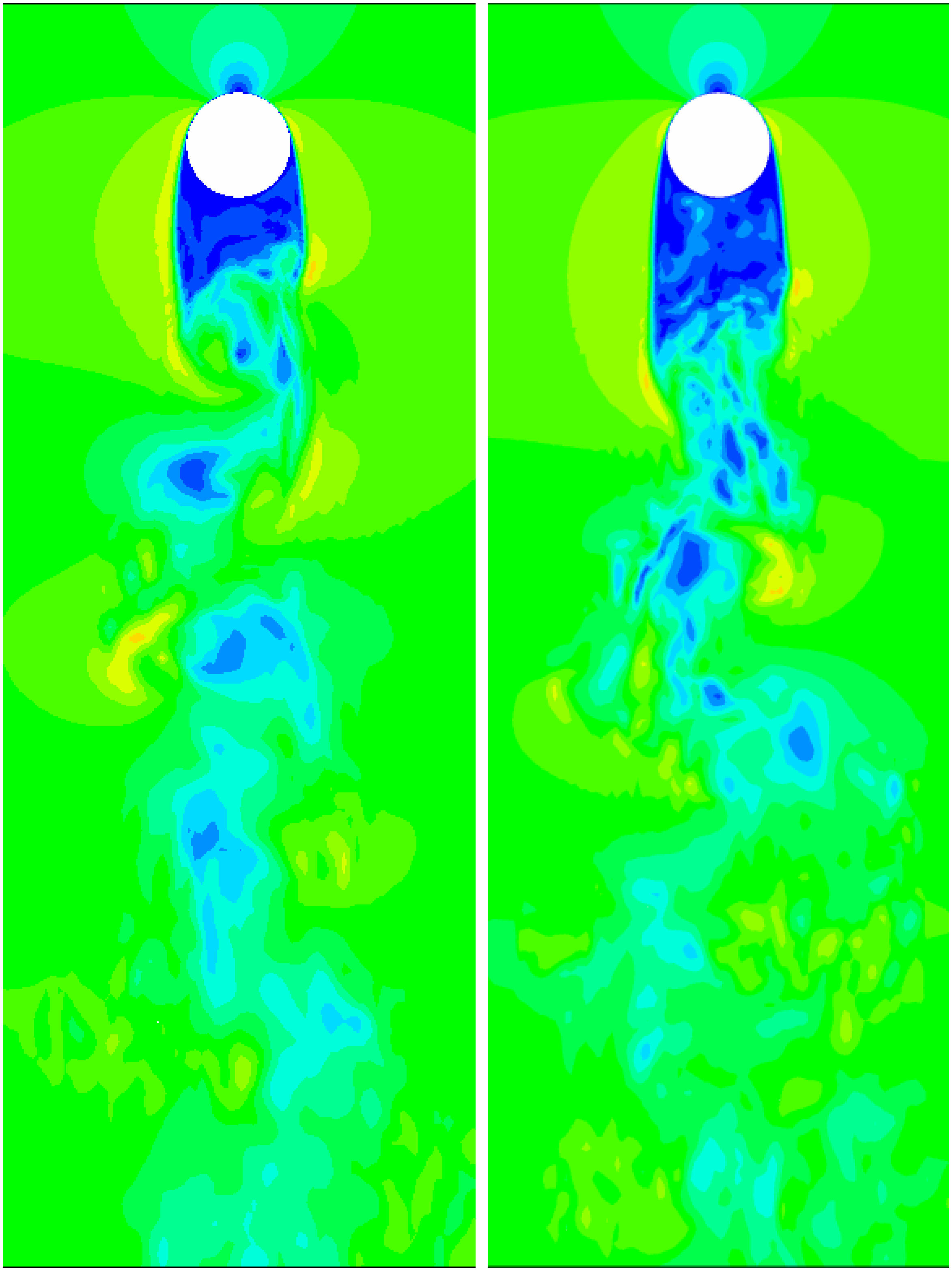

(a) (b)

Figure 3-13 Mach number in x-y plane. (a) coarse mesh; (b) fine mesh. There are 14 contours from 0.01 to 0.14.

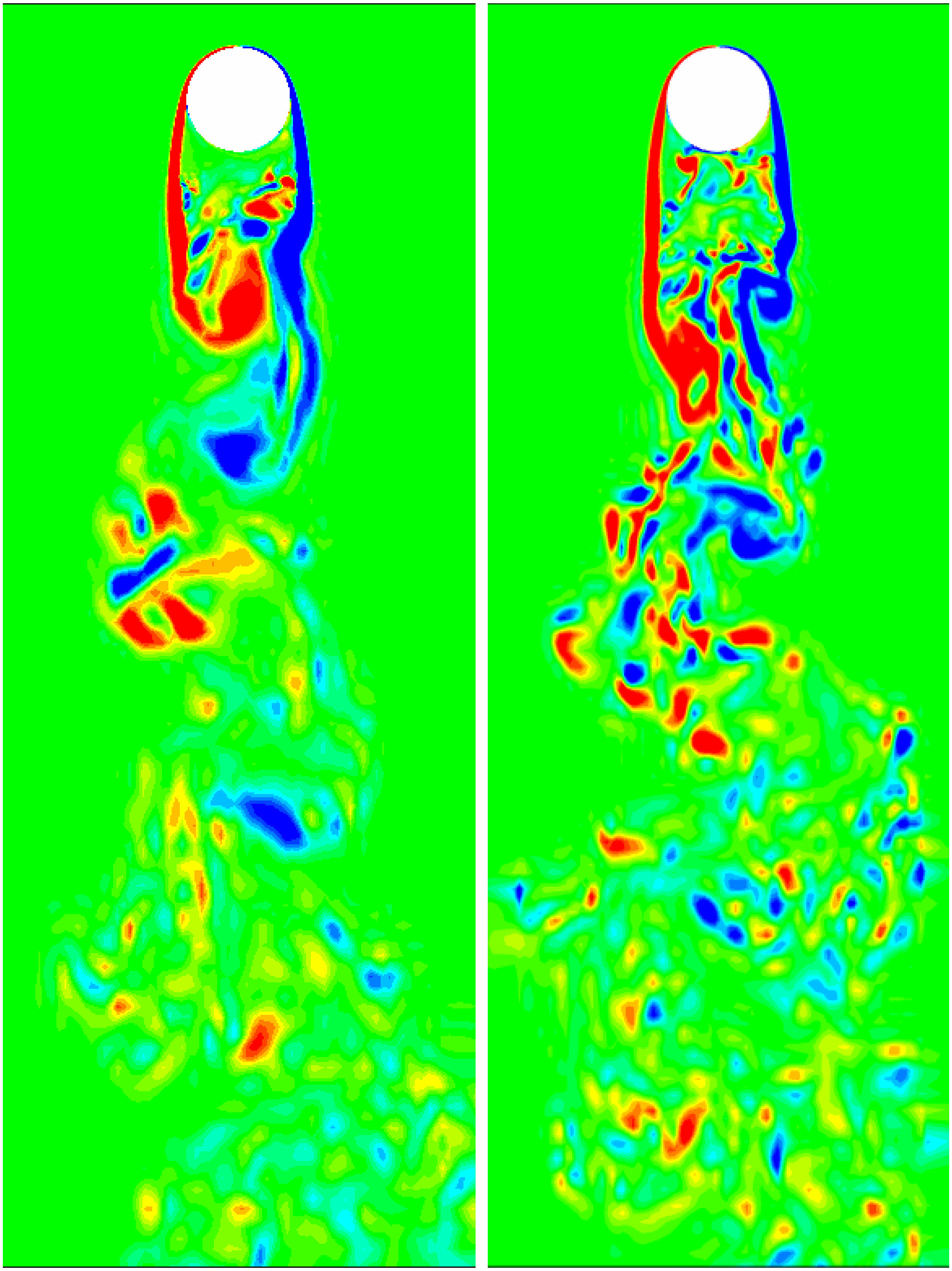
(a) (b)

Figure 3-14 Z-vorticity in x-y plane. (a) coarse mesh; (b) fine mesh. There are 16 contours from -0.3 to 0.3.

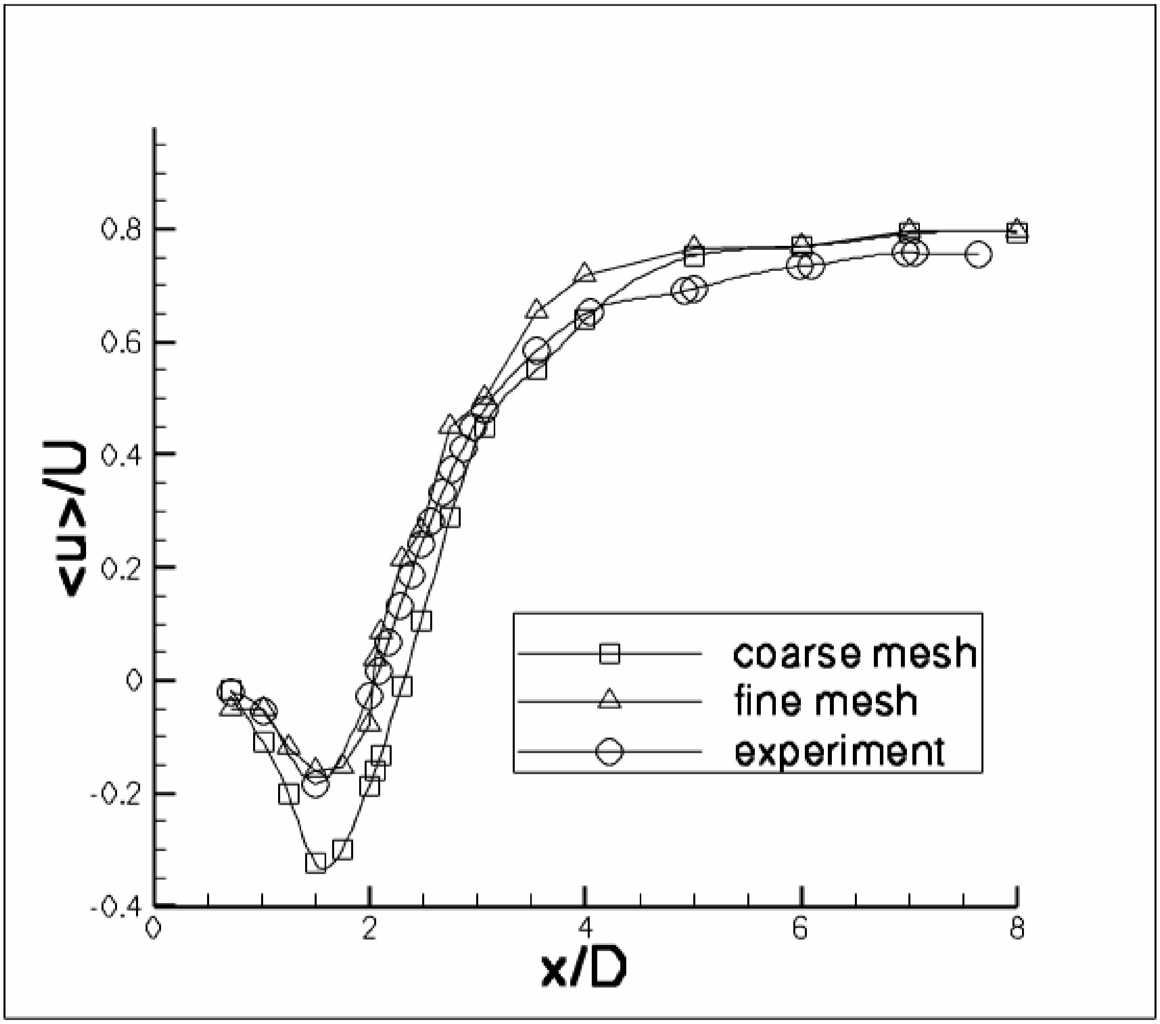

Figure 3-15 Distribution of the streamwise mean velocity along the wake center-line.

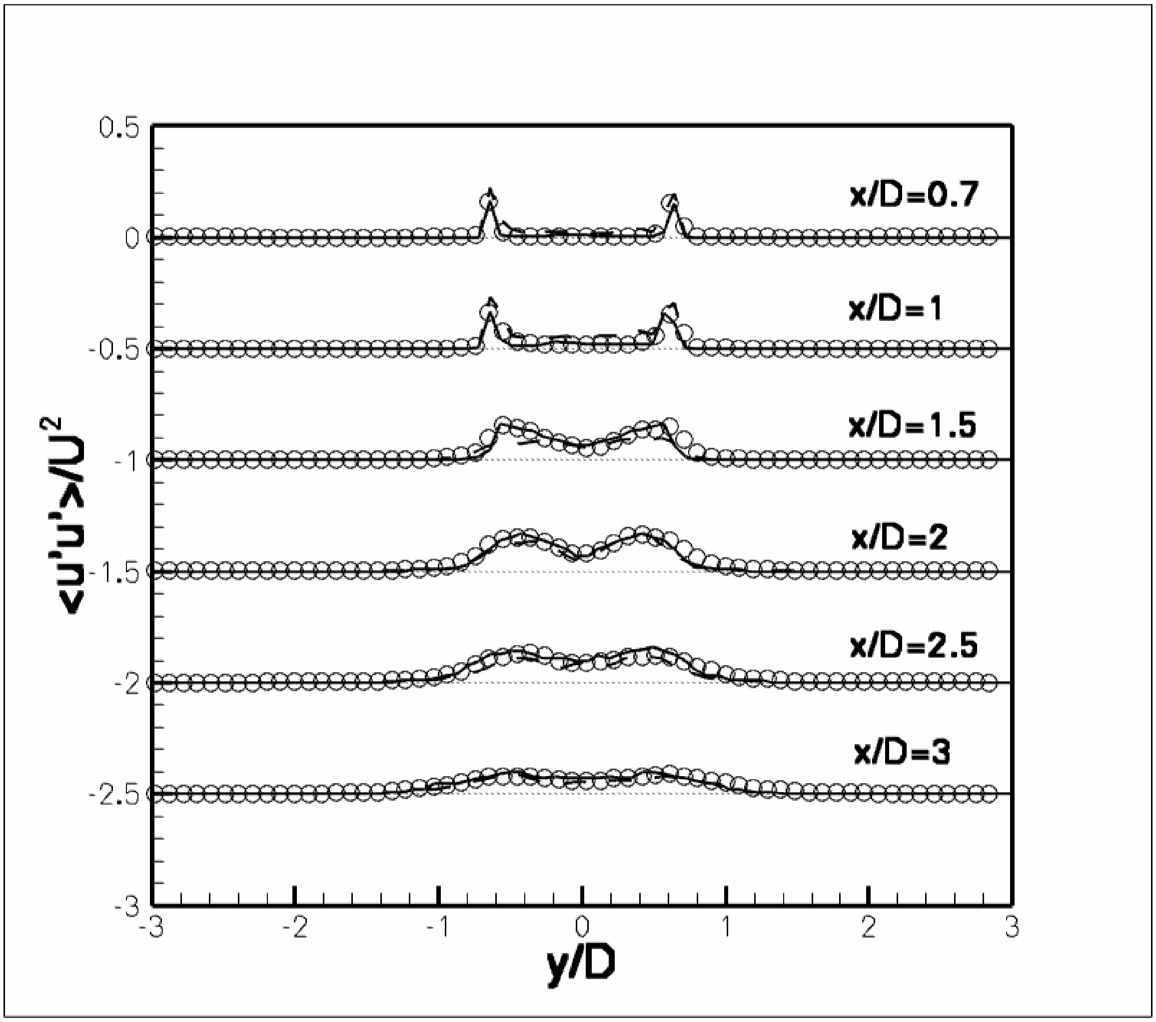

Figure 3-16 Normalized <u'u'>/U^2 in the wake of the circular cylinder, (oooo) - experiment; (Dashed line) – coarse mesh; (Solid line) – fine mesh. The dotted line (......) represents the zero location of the shifted curves.

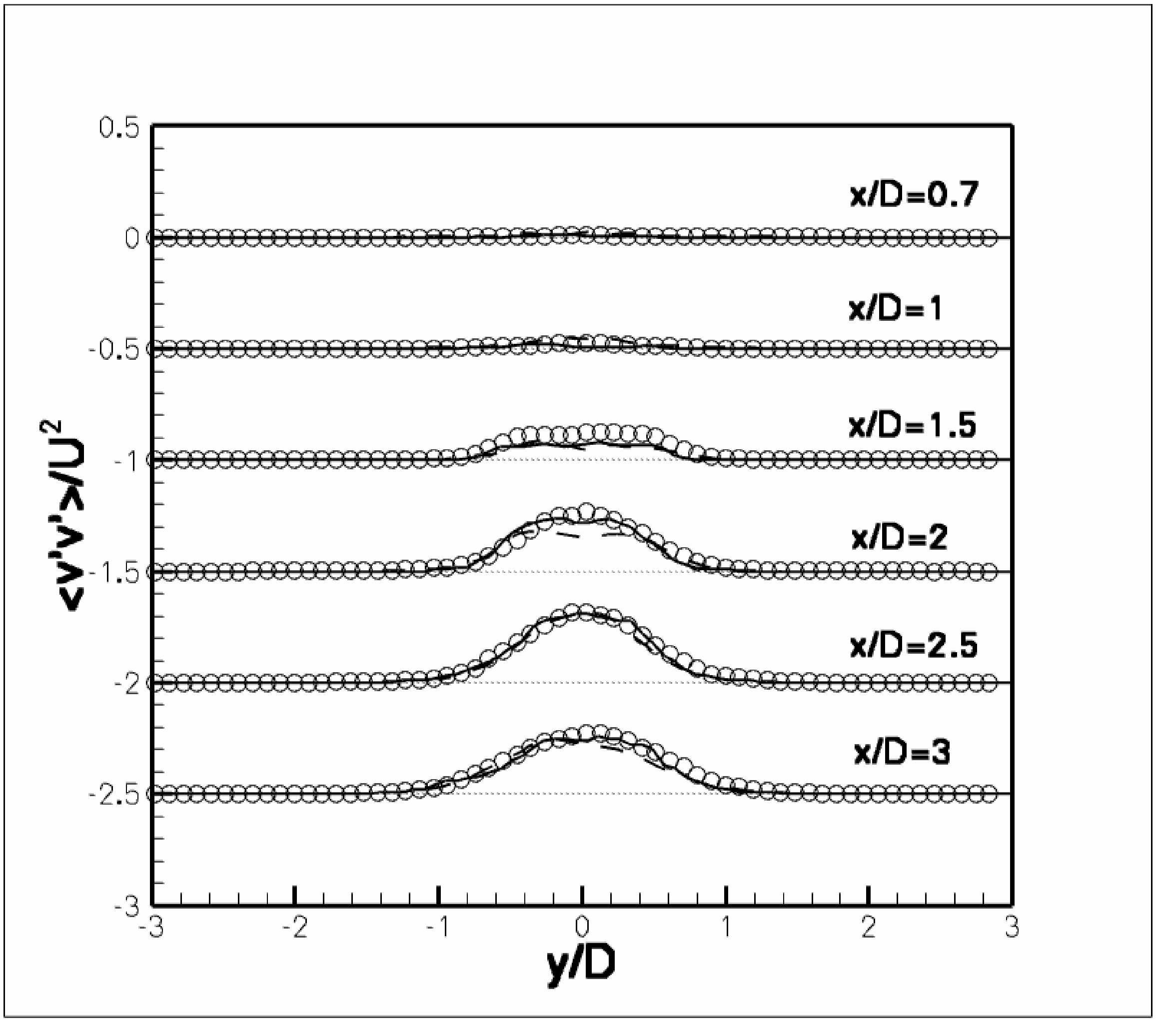

Figure 3-17 Normalized <v'v'>/U^2 in the wake of the circular cylinder, (oooo) - experiment; (Dashed line) – coarse mesh; (Solid line) – fine mesh. The dotted line (......) represents the zero location of the shifted curves.

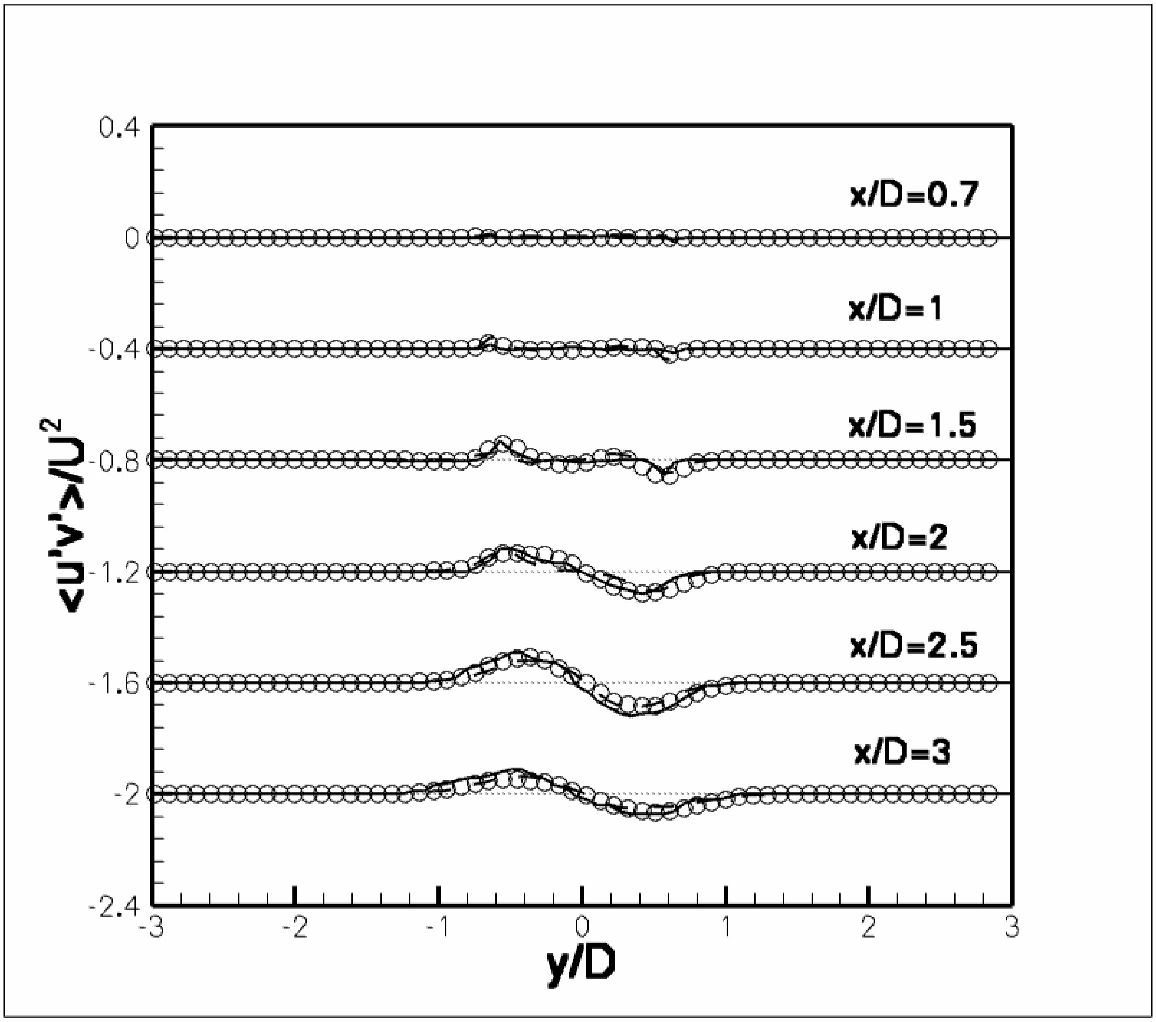

Figure 3-18 Normalized <u'v'>/U^2 in the wake of the circular cylinder, (oooo) - experiment; (Dashed line) – coarse mesh; (Solid line) – fine mesh. The dotted line (......) represents the zero location of the shifted curves.

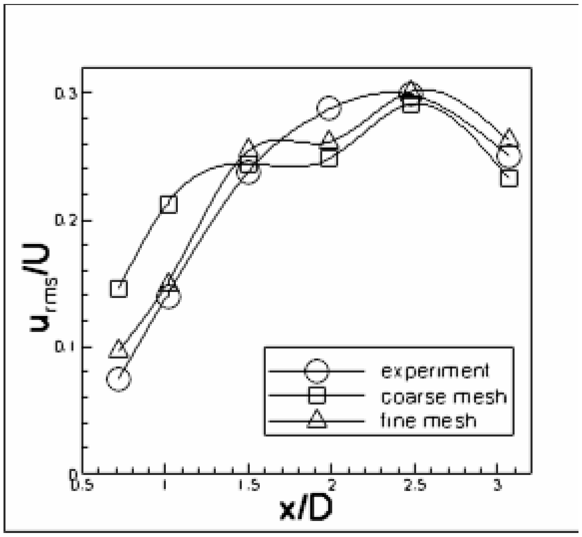

Figure 3-19 Distribution of the streamwise r.m.s. velocities along the wake centerline.

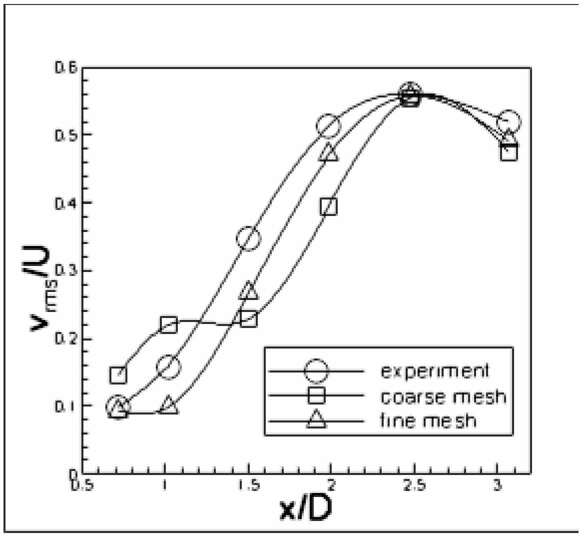

Figure 3-20 Distribution of the transverse r.m.s. velocities along the wake centerline.

Figure 3-15 shows the normalized streamwise mean velocity along the wake centerline. A small region of reversed flow occurs very near to the cylinder which is often defined as recirculation bubble. The velocity decreases and reaches a maximum negative value close to the cylinder and rises rapidly to positive values and finally reaching an asymptotic behavior far downstream. The length of the recirculation bubble is generally defined as the position downstream of the cylinder where the mean velocity becomes zero. The fine mesh gives an excellent agreement of the length of the recirculation bubble with the PIV measurements of Konstantinidis *et al.*[31]. Though the coarse mesh does not predict the length of the recirculation bubble accurately, it gives a very good agreement of mean velocity at the wake center line further downstream.

Figures 3-16 and 3-17 show respectively the normalized time-averaged streamwise and cross-wake Reynolds stresses. The peaks in the streamwise Reynolds stress are predicted very well. But the cross-stream Reynolds stress is a little under predicted at x/D=1.5. The shear stress predictions are shown in Figure 3-18. Both the coarse mesh and fine mesh are in good agreement with the experiment.

The distribution of the normalized streamwise and transverse r.m.s. velocities along the wake center line are shown in Figures 3-19 and 3-20 respectively. Figure 3-19 shows a peak at a position which is a measure of vortex formation length (Griffin[22]). Similar peak is observed in the case of transverse r.m.s. velocity distribution along the wake center line. It can be noted from Figures 3-19 and 3-20 that the magnitude of the transverse fluctuations is roughly two times that of the streamwise fluctuations at almost every position due to the way that vortices are formed, typical of bluff body wakes. The maximum r.m.s. fluctuations along the wake center line for the fine mesh is in good agreement with the experiment results. The maximum streamwise r.m.s. velocity $(u'/U)_{max}$ for the coarse mesh is slightly less than the experiment results. The maximum values were over predicted by Konstantinidis *et al.*[32]. The results agree very well with the ones published by Noberg[49] at a slightly higher Reynolds number $Re_D=3000$.

3.4 Conclusions

An unperturbed inlet flow past a circular cylinder at a Reynolds number of $Re_D=2580$ was simulated using the spectral difference method. The predictions for the mean velocities and Reynolds stresses agree well with the experiment results obtained by Konstanidis *et al.*[31]. The second order results are inaccurate but higher order (=3) of spatial accuracy gives excellent results. The length of the recirculation bubble and vortex formation length were very well predicted. The effect of mesh refinement was also studied by considering both coarse and fine meshes. Higher order results on a finer mesh showed the best agreement with experimental data. The wake characteristics were very well captured with the third order SD method, demonstrating its effectiveness and potential in handling bluff body problems and vortex dominated flows.

Chapter 4 – Flow over a Delta Wing

4.1 Introduction

Modern fighter aircraft and proposed unmanned combat air vehicle (UCAV) and macro air vehicles (MAV) incorporate wings of moderate sweep of about 40 to 60 degrees. The complex flows over these types of maneuvering, unmanned aircraft may involve massive separation whose simulation places numerous demands on a computational method. The flow fields are unsteady and three dimensional. The flow can involve regions of laminar, transitional and turbulent flows both on the surface of the wing and in the separated vortical flow. Significantly less research has been undertaken for these higher aspect ratio delta wing configurations. The aerodynamic issues associated with lower sweep angles may be even more complicated than those already encountered for slender delta wing flowfields. Several recent papers[25,44,50] have presented experimental investigations of the flow field structure over moderately swept wings. The current work performed explores the complex unsteady vortical flow field that develops over a 50 degree sweep flat plate delta wing through highly accurate numerical simulations. Most computations of the delta wing flows have employed lower-order (2nd order in space) numerical schemes. It requires large number of grid points to capture with sufficient accuracy the unsteady vortical flow features associated with a low sweep delta wing using these lower-order schemes. Therefore, to simulate the flow accurately, spectral difference method has been employed.

Morton et al.[46,47] and Görtz[20] have recently investigated the Detached Eddy Simulation (DES) approach to predict the unsteady vortical flow fields over delta wings. DES employs a RANS turbulence model (Spallart-Allmaras) to represent the assumed turbulent wall boundary layer. The model then smoothly switches to an LES-like model (Smagorinsky) in the separated region to represent the separated flow. In the present work, spectral difference method is employed. Once again, no subgrid scale model is used.

In recent years a concerted effort has been made both experimentally[50,57,58,72] and computationally[16] to understand the distinctive characteristics of low sweep delta wing flows. These investigations have primarily been performed at low Reynolds numbers

(<40,000). Reviews by Gursul[23] and Gursul, Gordnier and Visbal[24] provide good summaries of this body of work. Interest in higher Reynolds numbers exists due to the operation of UCAVs and small air vehicles in moderate Reynolds number ranges ($1\text{x}10^5 < \text{Re} < 1\text{x}10^6$). In the previous chapter, SD method showed good promise in capturing the flow physics for the flow around a cylinder. Hence it is used in the present work to study the flow over a low sweep delta wing. In the present work, computations are performed for a 50^o sweep delta wing at Reynolds number $\text{Re} = 2\text{x}10^5$. It is a preliminary study and more computational analysis needs to be carried out. Experimental measurements have also been made at the specified Reynolds number and are compared with the computed flow field. The results are also compared with the ones obtained by Gordnier and Visbal[16]. They used an implicit LES modeling technique which was developed based on the Pade differentiation and low-pass spatial filtering procedures.

4.2 Problem Definition and Computational Details

Computations are carried out on a low-sweep delta wing ($\Lambda = 50^o$). The model has a chord length c = 310mm and a thickness t = 5mm, giving a thickness-to-chord ratio t/c = 1.6%. The model has 45-deg beveled sharp leading edges, and a square trailing edge. Numerical simulations were carried out at a wing incidence of $\alpha = 15^o$ and at a Reynolds number of $2\text{x}10^5$ ($\text{Re} = U_\infty c/\nu$, where U_∞ is the free-stream velocity and ν is the fluid kinematic viscosity).

Figure 4-1 shows the equivalent delta wing geometry used in the computations. The present computations are carried out for one half of the delta wing assuming flow symmetry about its axis to reduce computational requirements. The computational domain is a rectangular cross-section of 3m x 6m. The boundaries are located far from the delta wing. The x-axis is along the line of symmetry of the delta wing. The z-axis is perpendicular to the plane of the delta wing. The upstream velocity is fixed at $U_\infty = 68$ m/s with an angle of incidence of $\alpha = 15^o$. The size of the computational domain in the y-direction is equal to approximately 10 times the chord length *c* of the delta wing. As mentioned earlier, the boundaries are very far from the body i.e. the domain size is 29c in the x-direction and 20c in the z-direction.

The mesh used in the computations is shown in Figure 4-2. The mesh has 159,000 hexahedra cells. The mesh is coarse for it to capture details of the flow. High-order spectral difference method is employed once again to solve the problem. Implicit scheme with 2nd order accuracy in time was used. Only 3rd order of spatial accuracy was tested since the mesh is already very coarse. For third order spatial accuracy, the coarse mesh has 4.29 million degrees-of-freedom (DOFs). The flow over a delta wing is highly complex especially over the top of the delta wing. A very fine mesh resolution is required to capture the flow physics in good detail[14].

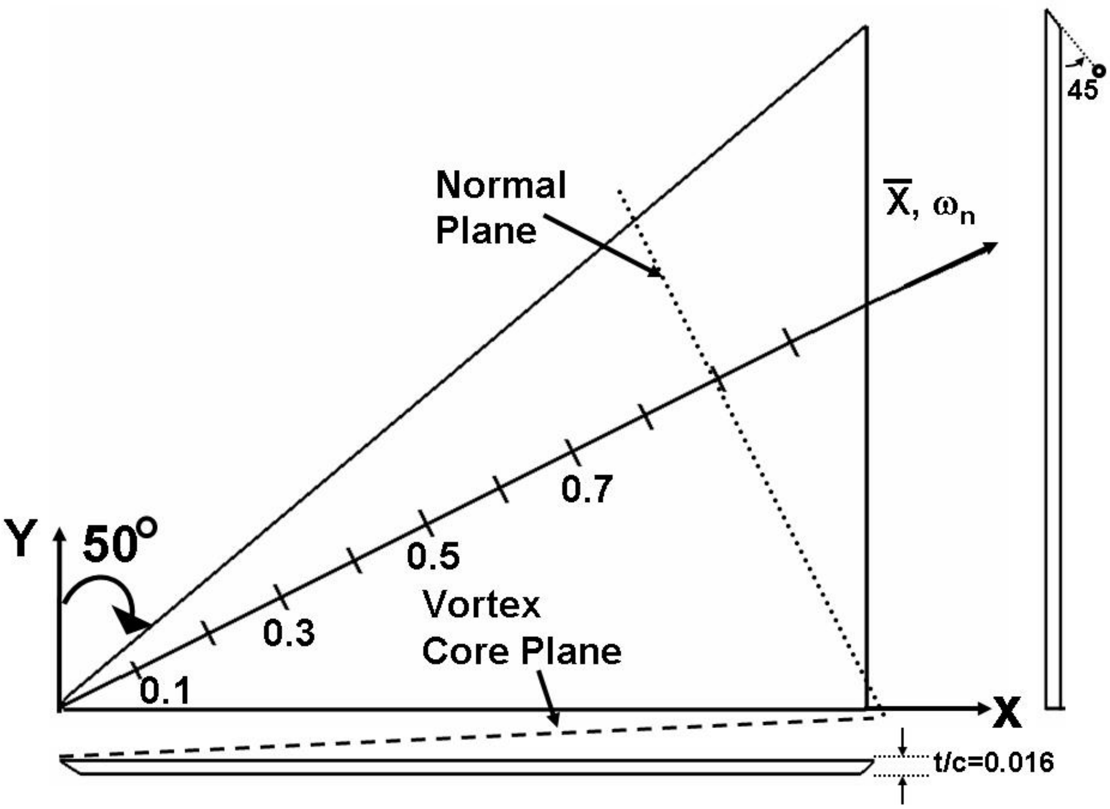

Figure 4-1 Computational Delta Wing Geometry[16]

The mesh consists of 84 points (i.e. 252 DOFs) in the axial direction (54 located on the wing), 86 points (258 DOFs) in the circumferential direction, 32 points (96 DOFs) normal to the upper surface of the wing and 10 points (30 DOFs) normal to the lower surface of the wing. The resolution is much finer on the upper side of the surface because the vortex core is formed on the upper side of the delta wing surface. A typical cross section of the grid used in the current work is compared with the one used by Gordnier and Visbal[16] in Figures 4-2 and 4-3, respectively, while the surface mesh comparisons are shown in Figures 4-4 and 4-5. The nominal spacing on the wing (x, y, z normalized by the root chord c) is $\Delta x = 0.004$ in the axial direction and $\Delta z = 0.0009$ in the normal direction at the (upper) surface. The mesh used by Gordier et al[16] was very fine in the normal direction. The nominal spacing Δz used by Gordnier et al[16] in the normal direction was 90 times finer than the one used in the current work. Computations are performed for the same conditions as in the experiment, $\alpha = 15^{\circ}$ and $Re = 2 \times 10^5$. A description of the mean vortical flow structure based on the computations is then presented.

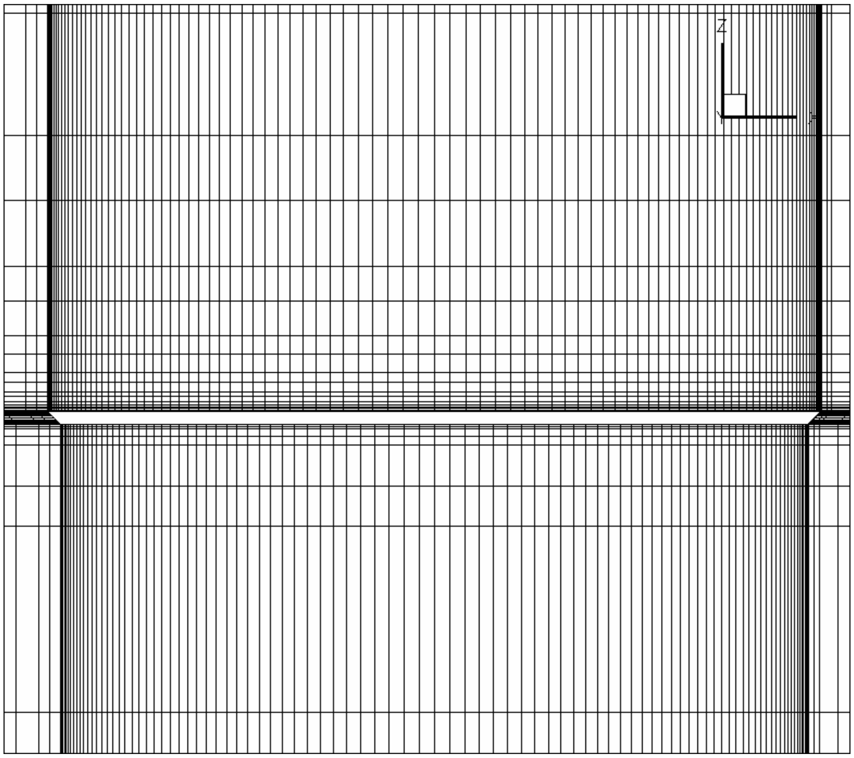

Figure 4-2 Grid structure of the cross-section of the delta wing

The boundary conditions for the flow domain are prescribed as follows. At the solid surface, the no slip condition is applied (i.e. u = v = w = 0). Symmetry conditions are employed on the symmetry plane of the delta wing, $\eta = 0$. Farfield boundary condition is used on rest of the other boundaries.

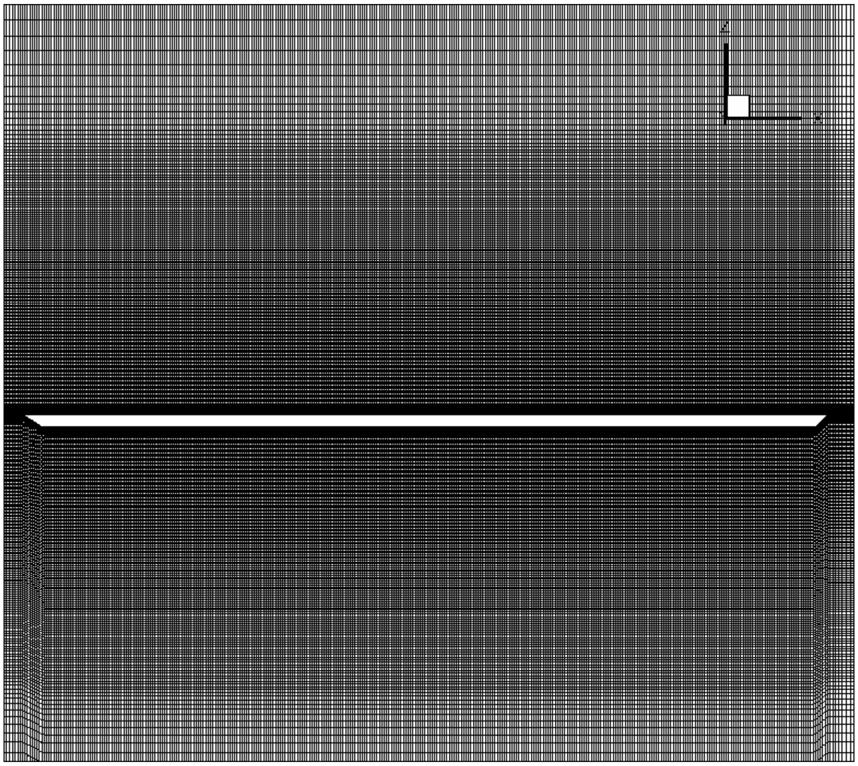

Figure 4-3 Grid structure of the cross-section of the delta wing used by Gordnier and Visbal[16]

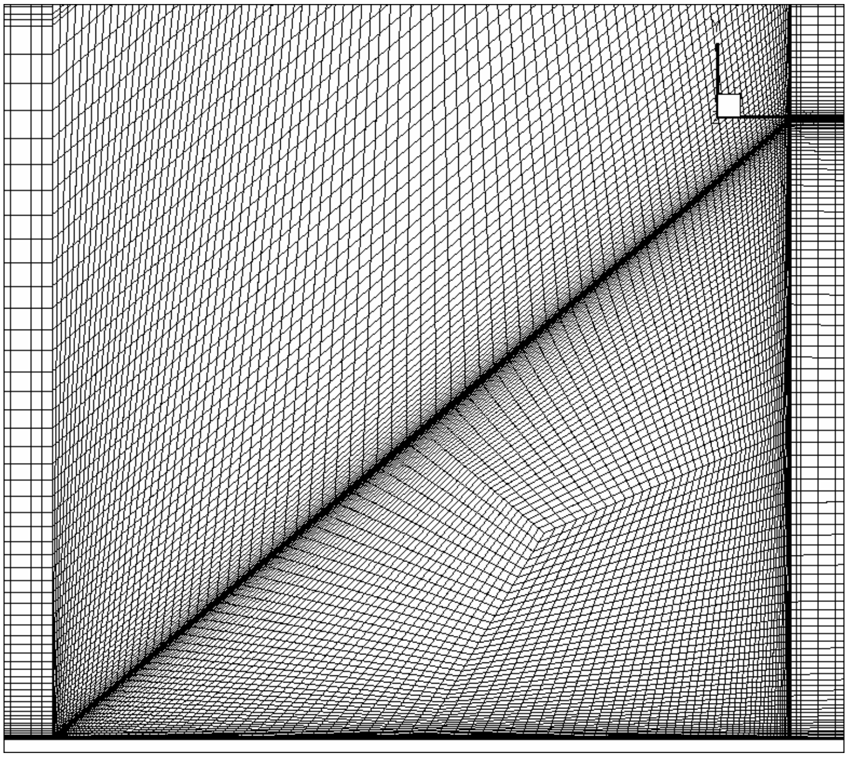

Figure 4-4 Grid structure on the surface of the delta wing

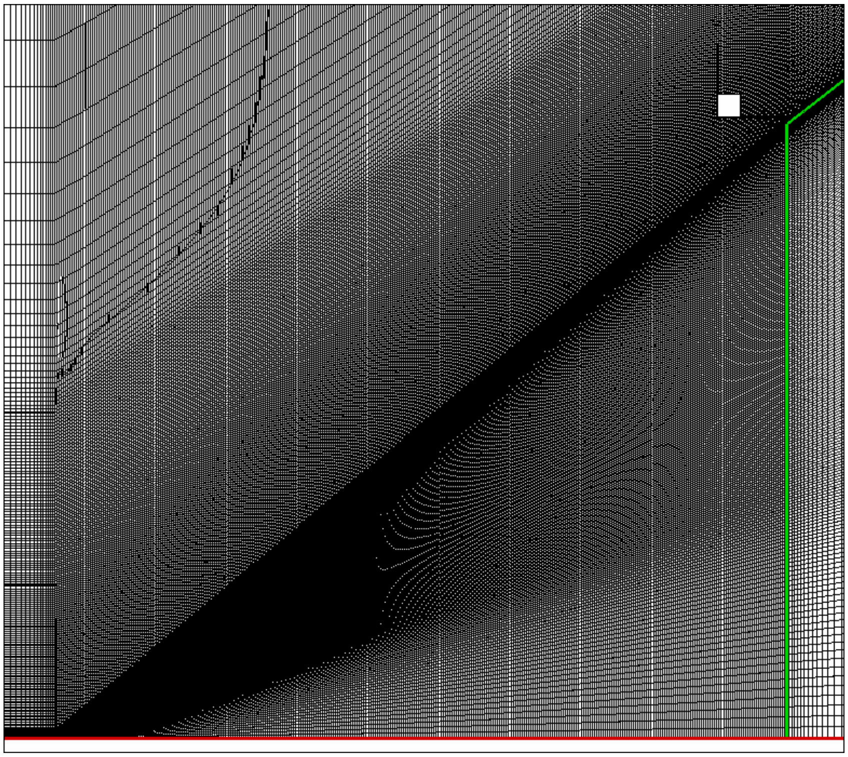

Figure 4-5 Grid structure on the surface of the delta wing used by Gordnier and Visbal[16]

4.3 Numerical Results and Discussion

The solution to the flow over a delta wing, like most other physical problems, is affected by mesh resolution and the type of numerical scheme. The mesh used in the current analysis is not fine enough to capture the details to a very good extent. But it gives an idea about the future and promise spectral difference method holds. The impact of mesh refinement on the global structure of the vortex for both the mean and instantaneous flow is demonstrated in Figures 4-6 and 4-7 respectively. The results obtained from spectral difference method are compared with the fine mesh results obtained by Gordnier and Visbal[16]. The numerical results of Gordnier and Visbal's work were obtained by private communication. The isosurfaces of axial vorticity colored by density contours highlight the general vortex structure. The mesh used in the current work gives a good idea about the vortex structure but was unable to capture the fine structures i.e. smaller scale unsteady features of the vortical flow. Due to this fact, the mean flow is also unable to exhibit the small scale substructures.

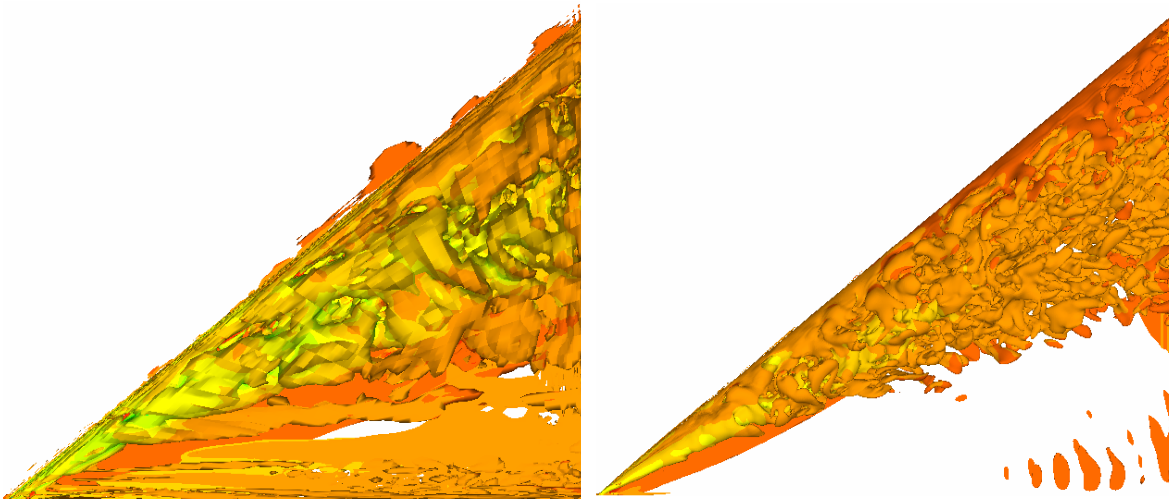

(a) (b)

Figure 4-6 Instantaneous vortex structure - Isosurfaces of constant axial vorticity colored by density contours (a) current work, (b) Gordnier and Visbal[16]

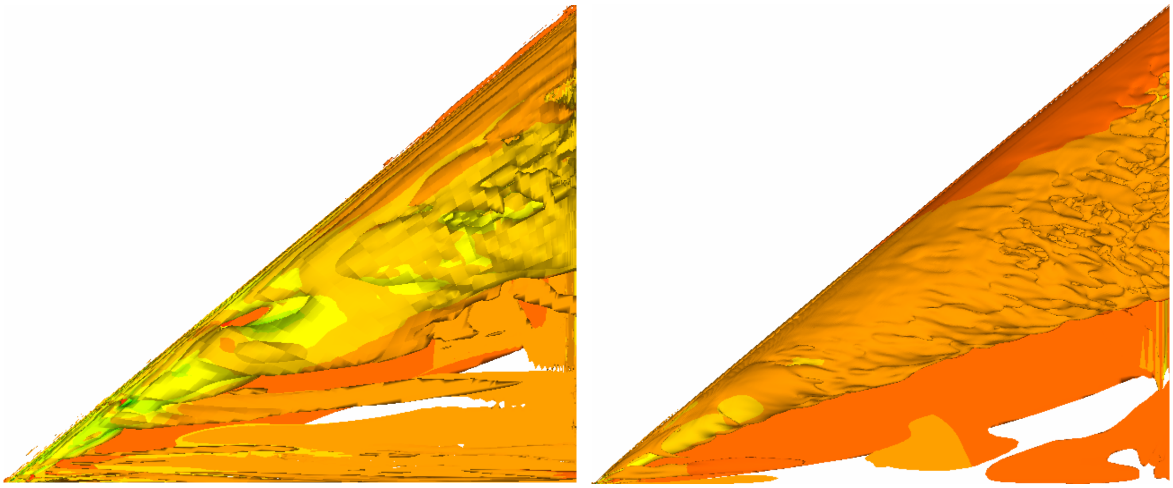

(a) (b)

Figure 4-7 Mean vortex structure - Isosurfaces of constant axial vorticity colored by density contours (a) current work, (b) Gordnier and Visbal[16]

The effect of mesh in the wing normal direction plays an important role. The mesh used in the current work, as mentioned before, is almost 100 times coarser than the ones used by Gordnier[16]. This effect on the computed flowfield can be further understood by examining the structures in planes normal to the vortex core as shown in Figure 4-1. Figures 4-8 (a) and (b) compare the vortex structure upstream of breakdown at a location

$\bar{x} = 0.1429$. It can be noticed that primary, secondary and tertiary vortices are observed, as well as a second vortex of the same sign as the primary vortex outboard near the leading edge. This type of dual vortex system has been observed previously for low sweep delta wings[16,58,72] and results from the interaction of the secondary flow with the primary shear layer.

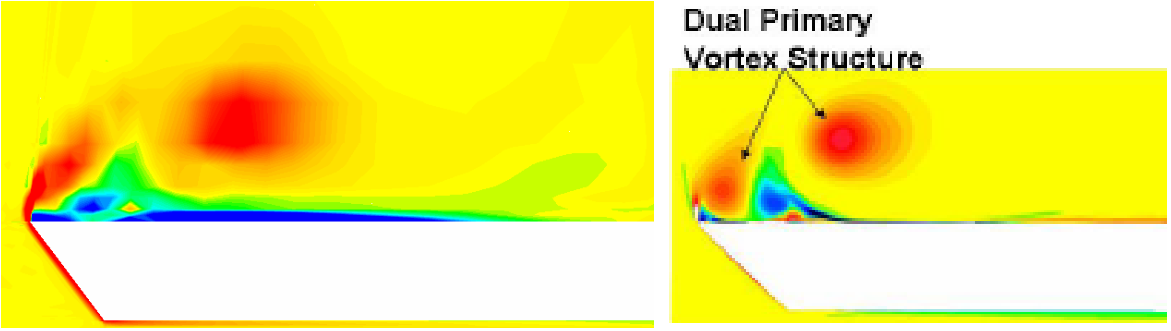

(a) (b)

Figure 4-8 Contours of the mean axial vorticity in a crossflow plane normal to the vortex, $\bar{x} = 0.1429$: (a) current work, (b) Gordnier and Visbal[16]

The weakening of the vortex upstream of breakdown is seen in Figures 4-9 (a) and (b) where contours of the axial velocity on a plane through the vortex core are plotted. Upstream of breakdown the peak jet velocity in the vortex core is bigger on the grid used in the current work, Figure 4-9 (a). The vortex breakdown location (normalized with chord) is similar to that obtained by Gordnier[16]. While the strength of the upstream vortex has been diminished, this has not resulted in a noticeable change in the vortex breakdown location.

Downstream of breakdown, the solution exhibits a much more detailed flow structure with significantly smaller scales being captured, Figure 4-10. The instantaneous flow shows large scale features in the outer shear layer that rolls up to form the vortex, but unable to capture the small scale features. This can also be noticed in the coarse mesh (Figure 4-10 (b)) used by Gordnier[16]. Enhanced interactions of these structures with the surface boundary layer are also seen as they move across the wing surface. Mesh refinement will result in capturing the smaller scales as well.

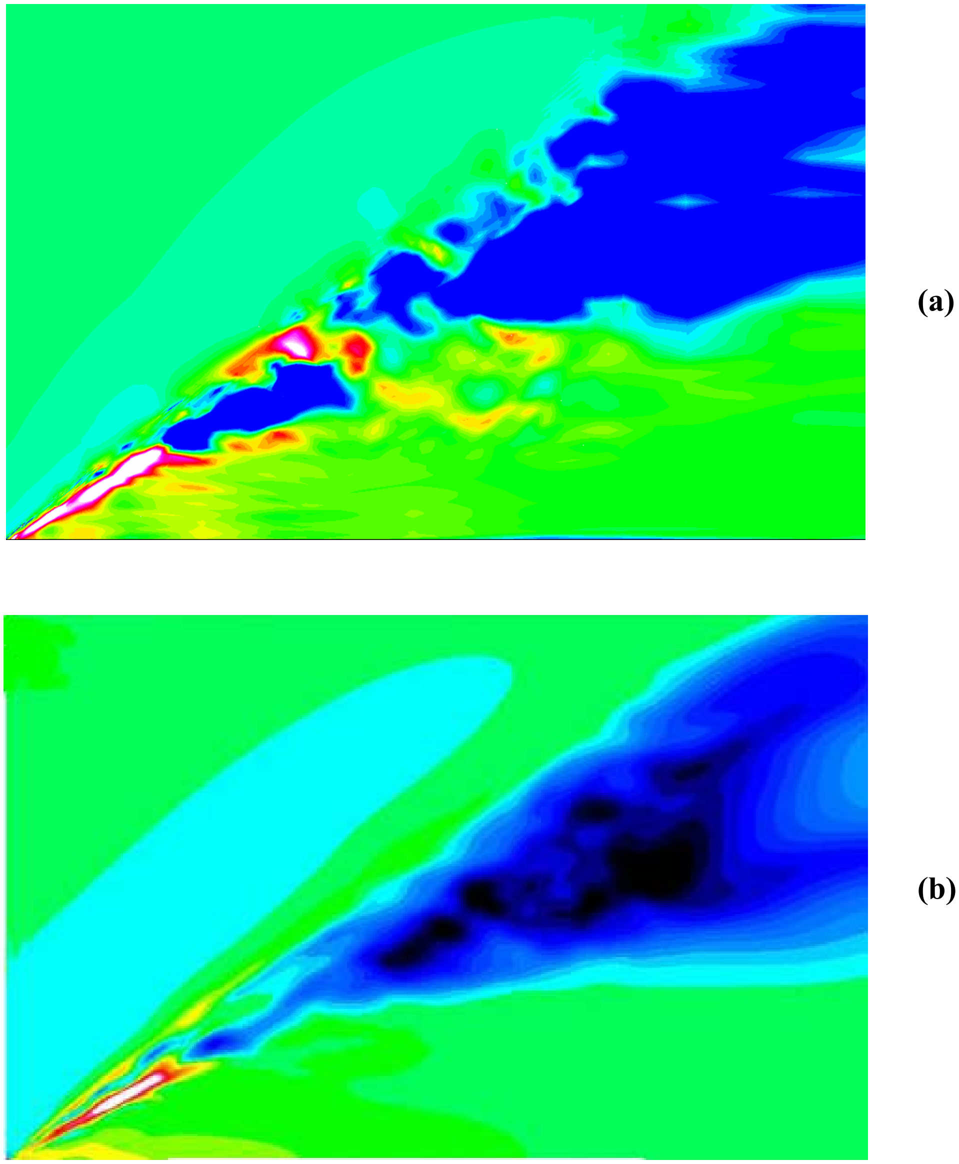

Figure 4-9 Contours of the mean axial velocity on a plane through the vortex core: (a) current work, (b) Gordnier and Visbal[16]

From the comparisons made till now with the computational results from Gordnier[16], it can be understood that the grid resolution shows significantly more of the unsteady, fine scale features of the flow. These results demonstrate that sufficient grid resolution remains important for correctly modeling this type of transitional flow even with the higher-order computational method employed.

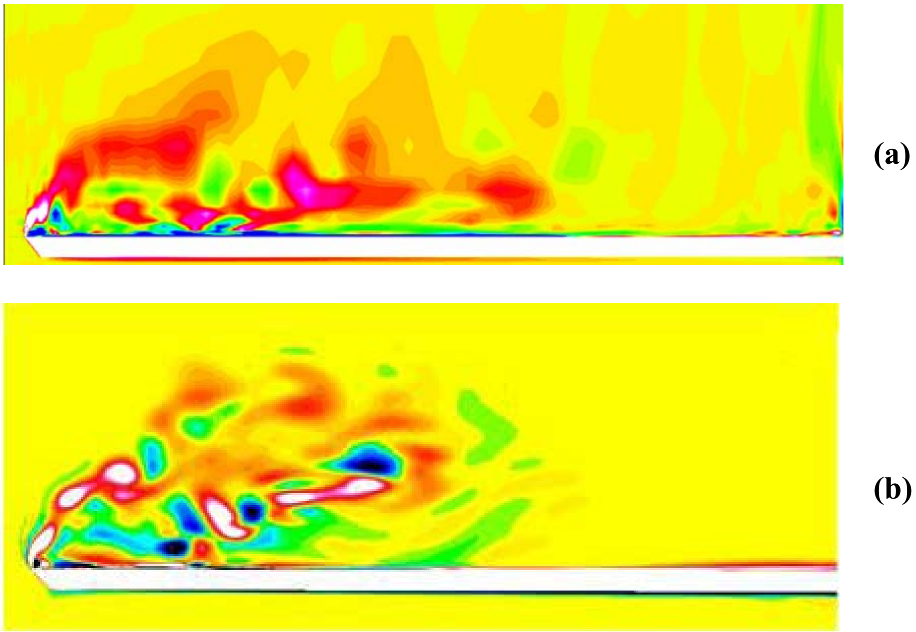

Figure 4-10 Contours of the instantaneous axial vorticity in a crossflow plane normal to the vortex, $\bar{x} = 0.85$: (a) current work, (b) Gordnier and Visbal[16]

Comparisons between the experimental PIV measurements and the computations are made for Reynolds number Re = 2×10^5. Figure 4-11 compares the mean vorticity at the axial location x = 0.2 for the current work, Gordnier's mesh and experiments. Good qualitative agreement is seen between the computation and the experiment with all the salient features in the experiment being reproduced in the computation. A comparison of the mean velocity magnitude on a plane through the vortex core, Figures 4-12 and 4-13, also display a striking similarity between the computation and the experiment with vortex breakdown occurring at approximately the same axial location. The results, Figure 4-12, shows a conically shaped region of low speed flow associated with vortex breakdown that penetrates approximately the same distance upstream with similar velocity levels. In between this region and the intact vortex core denoted by the high jet like velocities lies a region over which the breakdown of the vortex occurs. This region is longer than the one obtained by Gordnier[16] (Figure 4-13) but similar to the experiment result (Figure 4-14). The initial breakdown of the vortex in the current work occurs slightly upstream than that of the location from Gordnier's work.

The overall good agreement between the computation and experiment provides confidence that the spectral difference approach can properly capture the relevant flow features for this separated delta wing flow at moderate Reynolds numbers. Since the full three dimensional flowfield is available from the computations, only these results will be described in detail in the subsequent sections.

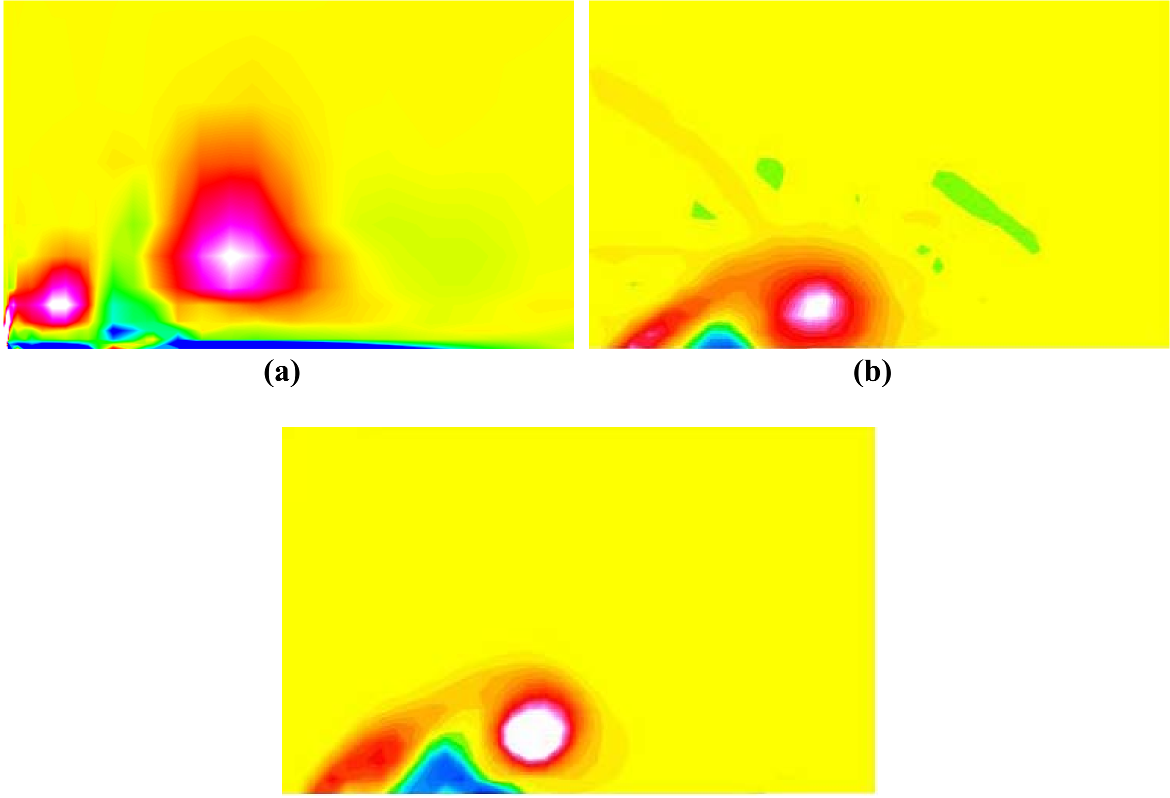

(a) (b)

(c)

Figure 4-11 Comparison between the computation and PIV measurements on the crossflow plane x = 0.2: (a) current study, (b) Gordnier and Visbal[16] and (c) experiment, Re = 2 × 10^5

The onset of vortex breakdown can be seen by examining the vortex structure on a vertical plane through the vortex core. Figures 4-15 (a) and (b) display contours of the mean axial velocity. A jetlike velocity region characterizes the intact vortex core upstream of breakdown. Downstream a transformation from this jetlike flow to wakelike flow occurs. This switch from jetlike to wakelike flow is indicative of the onset of vortex breakdown (see for instance References 53 and 61). No actual flow reversal is achieved in the wake region as observed for vortex breakdown over higher sweep delta wings.

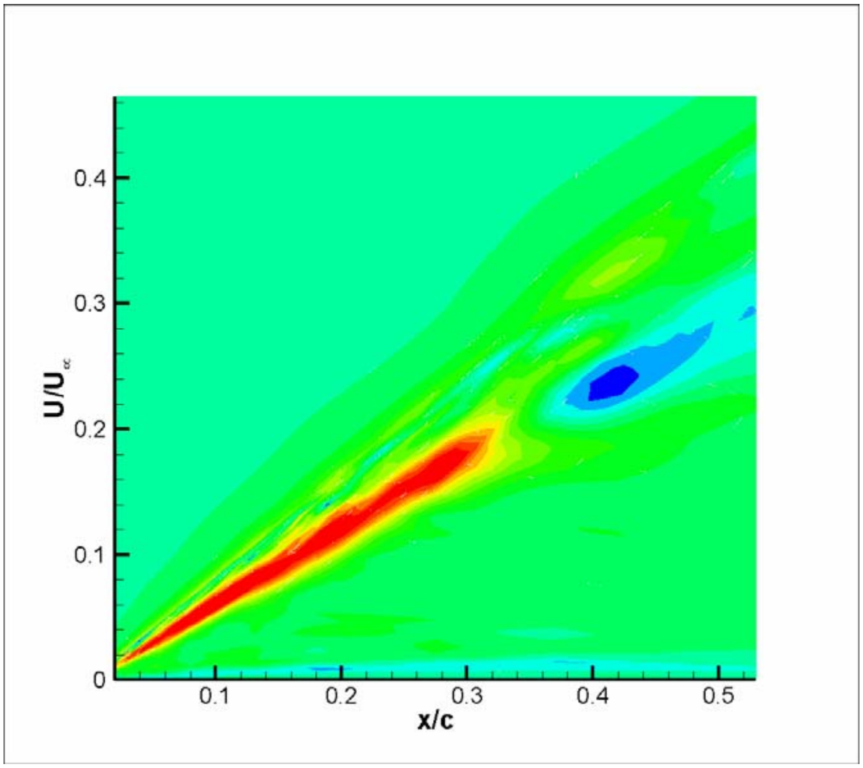

Figure 4-12 Computational mean velocity magnitude on a plane through the vortex core for the current work

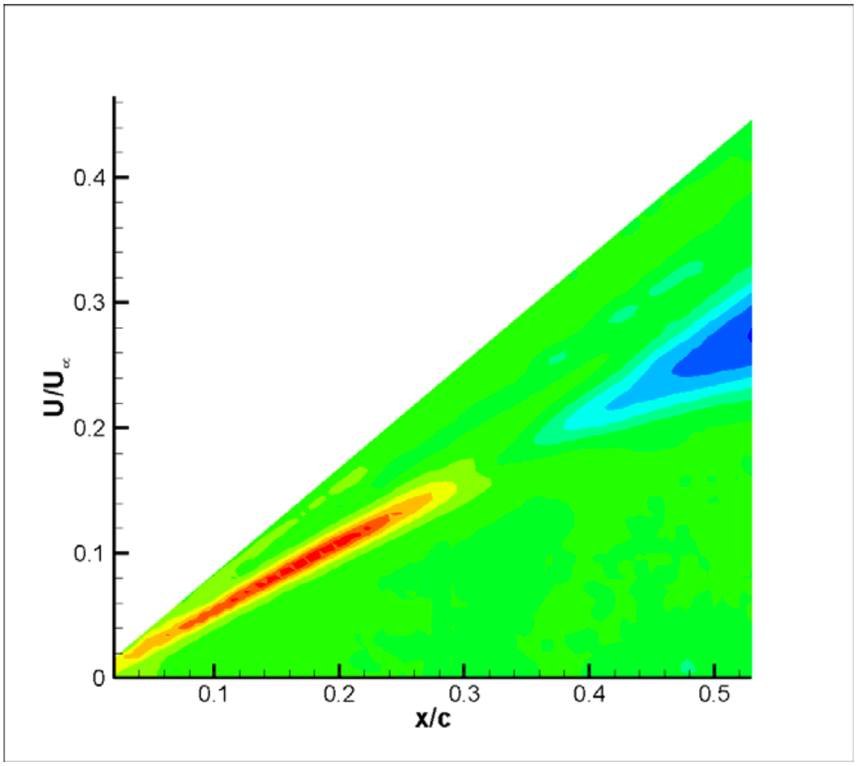

Figure 4-13 Computational mean velocity magnitude on a plane through the vortex core by Gordnier and Visbal[16]

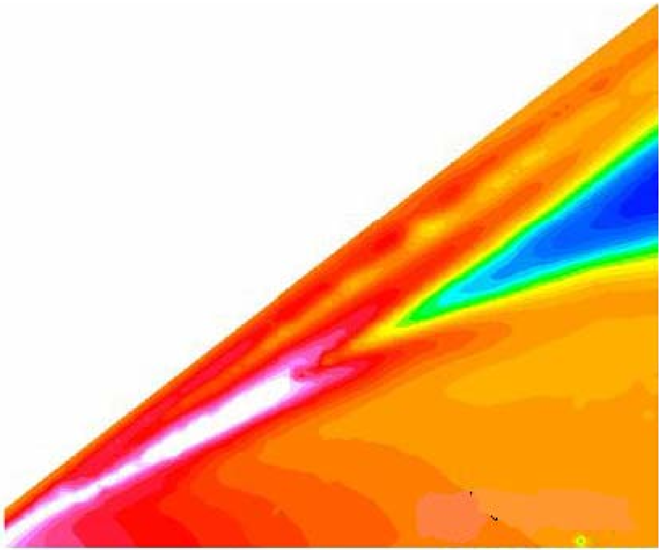

Figure 4-14 Experimental mean velocity magnitude on a plane through the vortex core

The onset of mean vortex breakdown is at x/c=0.3 and the normalized core velocity is 2.97. These values are over predicted when compared to the ones reported by Gordnier and Visbal[16]. The values for the coarse mesh used by Gordnier would be higher than their fine mesh results and comparable to the results obtained in the current work.

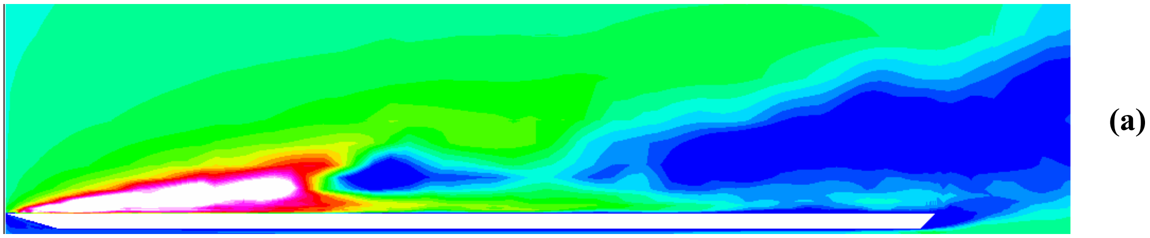

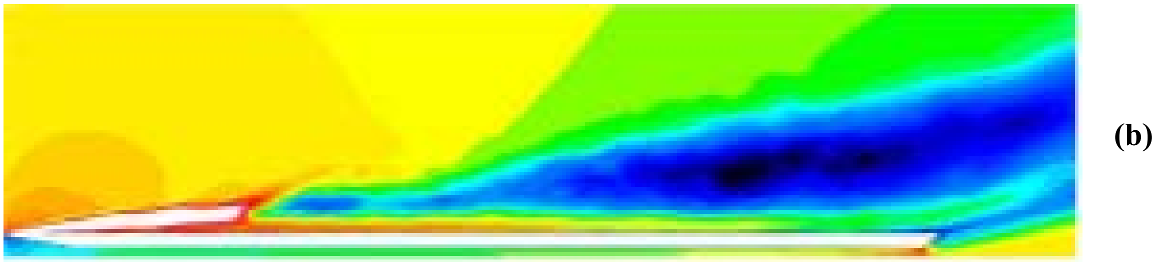

Figure 4-15 Mean axial velocity contours on a vertical plane through the vortex core: (a) current work, (b) Gordnier and Visbal[16]

The breakdown of the vortex thus appears to occur in two stages. In the first region a change from the strong jetlike velocity in the core to a more diffuse region of lower velocities is seen for a limited longitudinal extent. In the downstream portion of this stage there is a partial recovery of the velocity prior to the onset of a stronger conically-shaped wake in the second stage.

The mean vortex structure may be further elucidated by analyzing the flow on crossflow planes normal to the vortex core (see Figure 4-1) at locations both upstream and downstream of breakdown. Figure 4-16 plots the axial vorticity on a plane upstream of breakdown located at $\bar{x}$ = 0.175. For all cases distinct primary and secondary vortices are present.

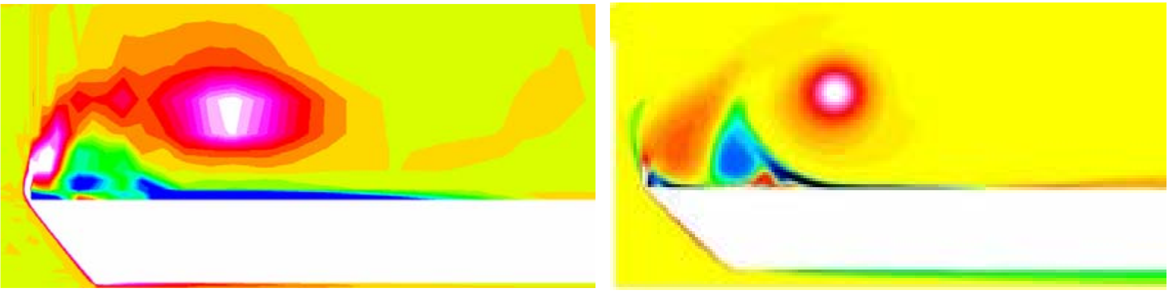
(a) **(b)**

Figure 4-16 Mean axial vorticity contours on a crossflow plane located at $\bar{x}$=0.175: (a) current work, (b) Gordnier and Visbal[16]

Similar dual vortex structures have been observed in previous computations[58] and experiments[14,23] and arise from the interaction of the secondary flow with the primary shear layer separating from the leading edge.

The highly unsteady behavior upstream of breakdown can be better understood by examining the flow in a crossflow plane normal to the vortex core, Figure 4-17. At locations upstream of breakdown there is a strong interaction of the leading edge vortex with the surface boundary layer flow that results in an eruptive response of the secondary flow with vorticity of the opposite sign being ejected from the surface and wrapped into the primary vortex. Accompanying this unsteady behavior is the development of small scale vortices in the shear layer that rolls up to form the primary vortex. This highly unsteady interaction of the primary vortex with the surface boundary layer and the corresponding development of shear layer instabilities have been described in detail in References[16,18,19,62,63].

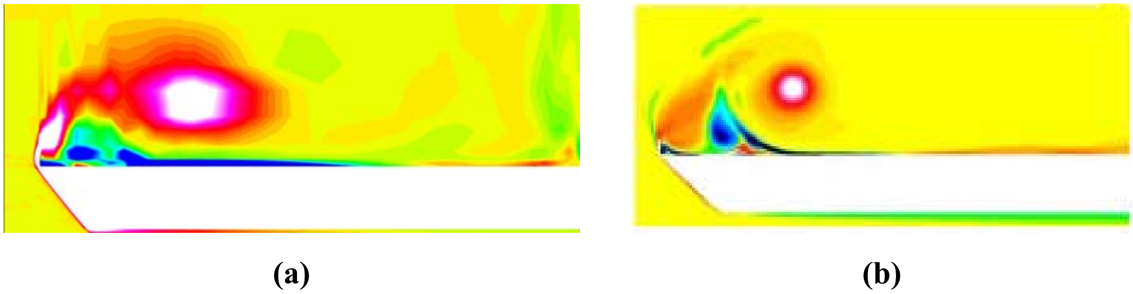
(a) (b)

Figure 4-17 Instantaneous axial vorticity contours on a crossflow plane normal to the vortex core at $\bar{x}$=0.175: (a) current work, (b) Gordnier and Visbal[16]

A mean separated flow region is associated with the onset of transition in the surface boundary layer near the symmetry plane and may be further understood by examining contours of the spanwise component of vorticity on the surface, Figure 4-18.

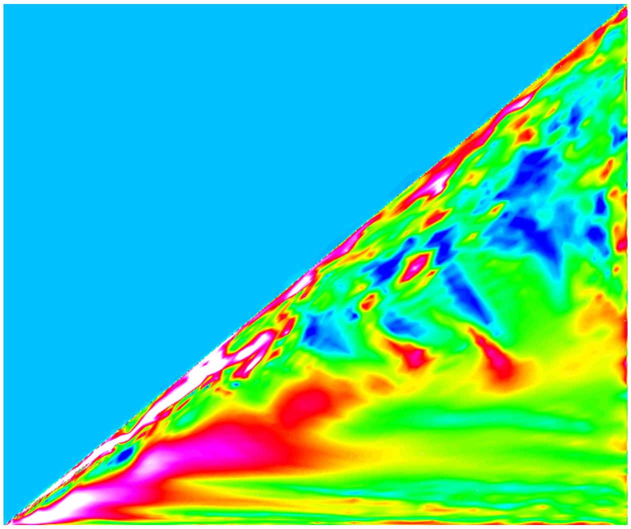

Figure 4-18 Instantaneous spanwise vorticity on the wing surface

These computations highlight the very complex surface boundary layer flows that may develop for this type of low sweep delta wing geometry at this moderate Reynolds number. The results depend highly on the numerical scheme used as well. Some models[17] may suppress this unsteady transition process due to the assumption of turbulent flow at all locations on the surface. Grid resolution is also another important factor. The results obtained using spectral difference method for the coarse mesh are satisfactory and show that the method has a good potential in capturing the physics of the flow over a delta wing. The results are encouraging and with the refinement of the mesh, the results should be closer to the ones reported by Grodnier and Visbal[16].

4.4 Conclusions and Future Work

Computations have been performed for a 50° sweep delta wing at 15° angle of attack and a moderate Reynolds number Re = 2 × 10^5. A preliminary study was carried out using the spectral difference method. The results were compared with the numerical and experiment results obtained by Gordnier et. al[16]. Even though a good qualitative agreement can be seen, an assessment of grid resolution needs to be carried out to significantly capture the smaller scales and providing a more accurate representation of the complex, unsteady, separated flow. But the results highlight the importance of both high-order accuracy and grid resolution in correctly simulating these types of transitional flows. The overall good agreement between the current work and Gordnier's[16] work provides confidence in the ability of the spectral difference approach to simulate these moderate Reynolds number flows.

A detailed description of the computed mean and instantaneous flow structure over the delta wing has been given including the vortex breakdown location. Downstream of breakdown the vortex takes a more oval shape and is comprised of a number of small scale features. The mean flow exhibits helical substructures that corotate with the primary vortex in the shear layer that separates from the leading edge and rolls up to form the primary vortex.

Transition of the surface boundary layer near the symmetry plane was also noted. This unsteady boundary layer flow is characterized by the formation of small scale vortical structures and their subsequent convection downstream. While it is likely that further grid resolution is required to fully capture this transitional/turbulent flow, the presence of this transitional flow region highlights why high-order techniques such as the present spectral difference approach are needed to model the complex flows existing at moderate Reynolds numbers.

The present work provides enough confidence about the performance of spectral difference method in predicting the flow features over a delta wing. But a lot of work still needs to be carried out i.e. like grid refinement to capture the small scale features more accurately. The author also suggests the study of flow over the delta wing with increasing Reynolds number and also at different angles of attack.

Chapter 5 – Tornado Type Wind Energy System

5.1 Introduction

The Tornado-Type Wind Energy System[73-75] is one of several and innovative concepts being investigated as potential ways to reduce the cost and broaden the usability of wind energy. This system (Figure 5-1) uses a large hollow tower to form an internal vortex, and the low pressure at the core of the tower provides an effective and low pressure exhaust reservoir for the turbine, which accepts air inlet supply. The tower serves as a stationary and omni-directional collector and concentrator capable of collecting immense amounts of wind energy and concentrating the collected energy into a high power density turbine. This system provides the unique advantages of a small, compact, vertical-axis, enclosed, and high efficiency turbine. This wind energy system promises a structurally rugged and stable design for both on-land and offshore installations. Based on this design, large and low-cost multi-megawatt wind energy systems may be developed and constructed for the utilities, and small and economically competitive systems may be provided for individual farms and homes.

Analytical investigations of several designs are being carried out. It will however be sometime before all the flow processes involved will be known well enough to yield highly accurate analytical predictions of performance. A variety of models have been designed and CFD analysis has been carried out. Experiments were carried out in the low speed wind tunnel at Iowa State University on some of the models. The prospect for the Tornado-Type Wind Energy System looks encouraging.

Computational and experimental investigations on the Tornado-Type Wind Energy System (Figure 5-1) have been carried out. A general description of the system is presented below:

There are several major difficulties that have to be overcome by an innovative wind energy concept in order to develop a low-cost, rugged, and practical wind energy power plant capable of producing large amounts of power e.g., 10 to 100 MW. The principal difficulty is caused by the basic fact that the energy density of wind is very low. With usual system efficiency or a power coefficient of 30%, a collecting surface of around of around 200m in diameter is needed for a wind energy power plant to collect sufficient amounts of wind energy for producing 10 MW with a 30 mph wind speed. This diameter is increased to 600m if the wind energy power plant is to produce 100 MW.

5.2 System Description

In the Tornado-Type Wind Energy System, a stationary collector is used for collecting immense amount of wind energy, and then concentrates and converts the wind energy into mechanical energy using a compact vertical-axis turbine which is located near the ground. Briefly, as seen in Figure 5-1, wind energy is collected by a stationary and omni-directional collector comprised of a stationary tower. Incoming wind into the tower forms a vortex. The low-pressure core of the vortex is situated directly above the vertical axis turbine so as to reduce the back pressure of the turbine. The underside of the turbine is connected to the atmosphere through an omni-directional bottom inlet. A well designed bottom inlet may raise the pressure within the bottom inlet to the ambient stagnation pressure, higher than the ambient atmospheric pressure.

It is well known that the core of a strong vortex can have a very low pressure. Hence, the vortex and the bottom inlet can maintain a very large pressure difference across the turbine. For example, for a 30 mph (14 m/s) wind, the dynamic pressure $q_\infty = \frac{1}{2}\rho V_\infty^2$ of the wind amounts to only 1/930 of the standard atmospheric pressure. Hence, if the vortex core pressure is at 5% below the atmospheric then a pressure difference of more than $45q_\infty$ can be maintained across the turbine. In contrast, less than one q_∞ can be maintained by the wind across a conventional propeller-type wind turbine. Hence, a Tornado-Type Wind Energy System can produce a much larger pressure difference across, and a much higher power density from the turbine.

5.3 Experimental Investigations

All the experiments were carried out at the Iowa State University. Detailed static pressure measurements have been made in two wind tunnels of sizes 8ft wide by 6ft high section and 3ft high by 2.5ft wide at various wind speeds. Two different sizes of the models were tested out in the wind tunnels. The computational results are compared with the results obtained from the wind-tunnel experiments.

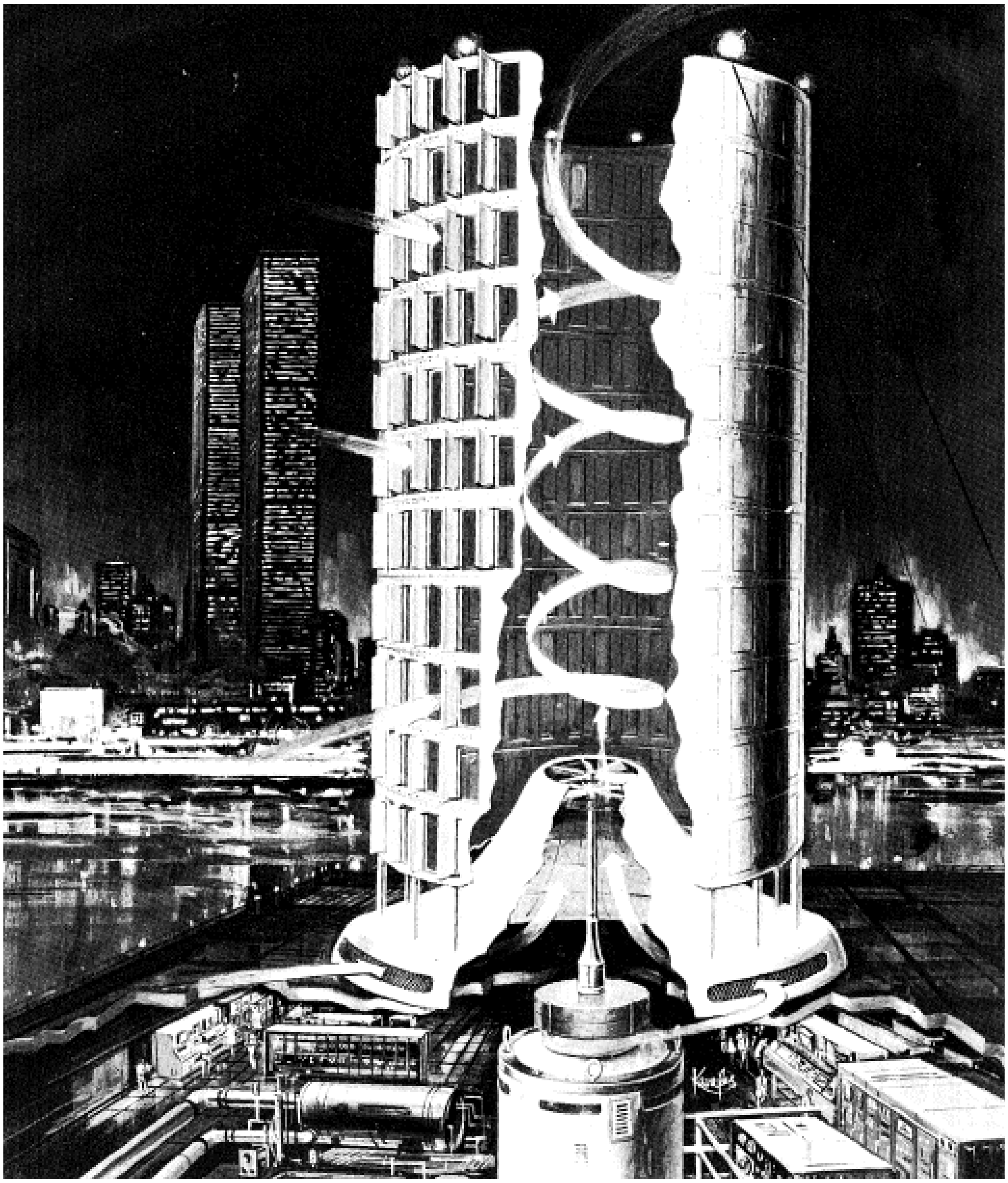

Figure 5-1 Large Tornado-Type Wind Energy System[74]

5.4 Problem Definition and Computational Details

The Tornado-Type Wind Energy System has a spiral shaped collector. The shape of the spiral is governed by the equation $r = r_o e^{-\alpha\theta}$ where r_o is the radius of the spiral at $\theta = 0$, α is a constant and θ is the angle in degrees. The parameters, r_o and α can be varied to get different shapes of the spiral. The diameter D of the spiral is the distance between the points on the spiral at $\theta = 0^o$ and $\theta = 180^o$. A typical 2-D spiral-shaped wind turbine is shown in Figure 5-2. It has an inlet through which air enters and swirls around to form a strong Rankine vortex. Some of the parameters which can influence the pressure coefficient inside the tower are tower height (H), ratio of tower height to diameter (H/D), blockage ratio, to name a few. Models with different inner diameter and tower heights were created and a steady state solution was obtained for them. As mentioned in the previous section, experiments were also performed on a few models for the simulation results to be compared with. The origin and size of the computational domain are shown in Figure 5-3. The x-z cross-section matches with the wind tunnel cross-section. Three different wind tunnel cross-sections (x-z) were used in the analysis i.e. 0.6m by 0.9m, 0.8m by 0.9m and 2.44m by 1.83m. The inlet and outlet of the computational domain is shown in Figure 5-3. The streamwise flow is in the negative y-direction. The tower height is in the z-direction. The upstream velocity is fixed at V_∞=5.7 m/s and is assumed to be uniform across the inlet. The Reynolds number of the flow is 50,000.

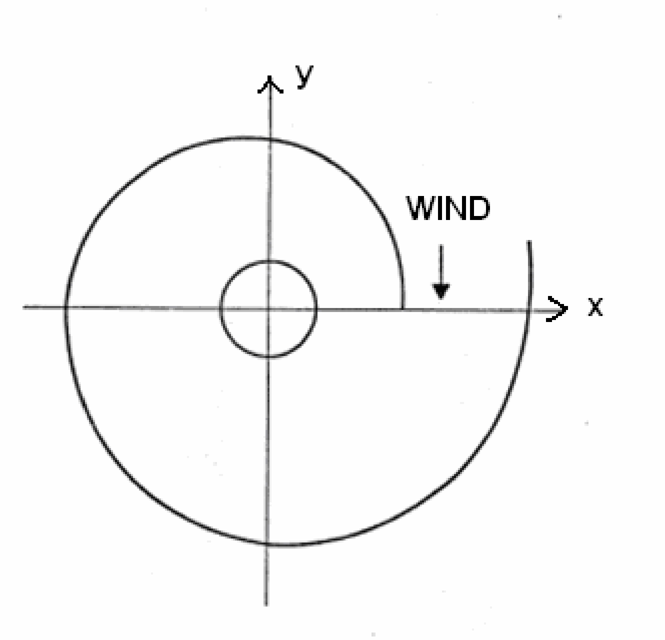

Figure 5-2 Defining the coordinate system for the tower bottom wall

In Figure 5-3, an inlet boundary condition is used at the entrance. Fixed pressure boundary condition is applied at the outlet of the domain. Zero velocity boundary condition is used for the turbine tower wall, while symmetry is imposed on the other surfaces.

Numerical simulations were carried out to seek a steady state solution for different shapes of the spiral. The aim was to obtain practical design parameters which lead to minimum pressure at the tower bottom. A 2nd order finite volume code MUSIC[65] capable of handling arbitrary meshes for compressible fluid flow was used to carry out the numerical simulations. Roe flux difference splitting scheme is used in the convective flux discretization. A commercial solver FLUENT[12] was also used to solve the problem and make comparisons with the results obtained from MUSIC and experiments. Mostly, MUSIC was used to carry out the numerical simulations. A second order scheme in space with a block LU-SGS time scheme for time integration was used. No turbulence model was used with MUSIC. Though, for some of the simulations, a limiter was used. Some of the numerical simulations were carried out using FLUENT with a SIMPLE pressure-based discretization. A 2nd order steady implicit scheme with two different turbulent models Reynolds Stress Models (RSM) and Spallart-Almaras (SA) were used in FLUENT.

5.5 Mesh Details

One of the challenging aspects of this problem was to create a mesh with reasonable resolution to capture the vortex and to avoid its dissipation due to coarseness of the mesh. The mesh and geometry details for all the cases are given in Table 5-1. For case 1, grid refinement study was carried out to assess numerical errors if any. Three meshes with different resolution were created – coarse, fine and finest. The coarse mesh has 1.9 million cells, fine mesh has 3.6 million cells and the finest mesh has 5.1 million cells. The mesh details for different resolution are shown in Table 5-2. Since a strong vortex is formed at the center of the spiral, the mesh resolution in the radial direction is increased from the coarse mesh to the finest mesh. The resolution in the z-direction i.e. along the tower height was increased tremendously from the coarse mesh to the finest mesh. Case 1 forms the basic setup of the problem. Variations have been made to this model to study the effect of H/D ratio, tower height H and the size of the wind tunnel on the pressure coefficient C_p and hence the vortex strength, were carried out for the coarse mesh. The height of the turbine in case 1 is decreased by 20% and it refers to case 2. The height of the turbine model in case 1 is increased by 20% to form case 3. Case 4 refers to a model in which the inlet of the spiral is decreased by roughly 17%, but increasing the H/D ratio by 20%. Case 5 and Case 6 refer to the basic model i.e. case 1, but with different wind tunnel cross-sections. Another model (case 7) was created by increasing both H and D but keeping the H/D ratio the same as that of case 1 i.e. H/D=2.76. Case 8 refers to a model created in GAMBIT, a pre-processor to a 2nd order finite volume commercial code FLUENT. FLUENT is the solver used for cases 8a, 8b and 8c. The fluid flow was modeled as inviscid in FLUENT and is referred to as case 8a. Case 8b and 8c respectively use turbulence models Reynolds Stress Model (RSM) and Spalart-Allmaras (SA) method.

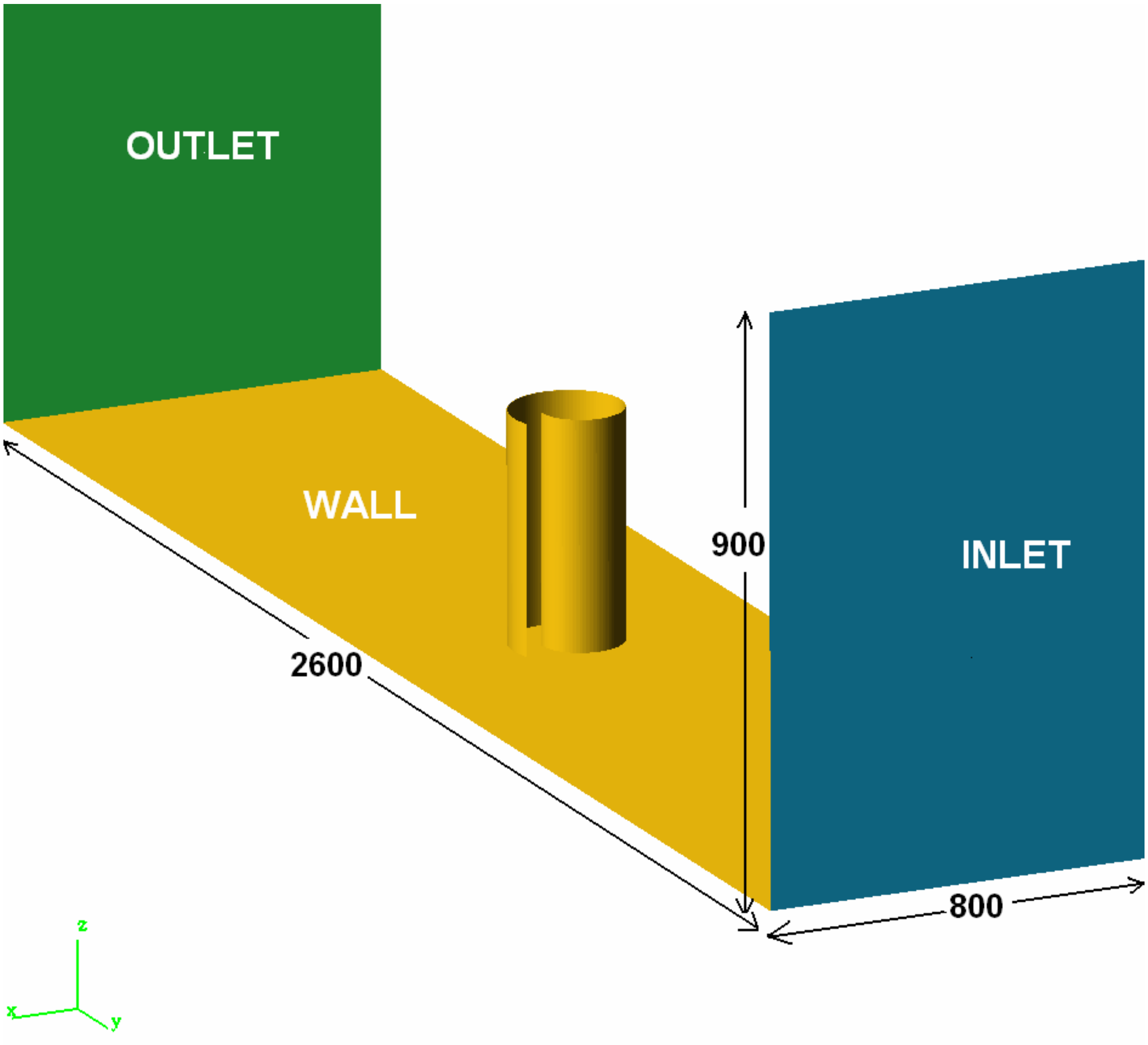

Figure 5-3 Three dimensional view of the computational model

Name	**Wind Tunnel cross-section (mm x mm)**	**Height (mm)**	**Diameter (mm)**	$\frac{H}{D}$	**Mesh Size**	**Solver**
Case 1	800 x 900	350	126.98	2.76	1,922,837	MUSIC
Case 2	800 x 900	280	126.98	2.21	1,922,837	MUSIC
Case 3	800 x 900	420	126.98	3.31	1,919,267	MUSIC
Case 4	800 x 900	420	105.78	3.97	2,014,567	MUSIC
Case 5	600 x 900	350	126.98	2.76	1,922,837	MUSIC
Case 6	2440 x 1830	350	126.98	2.76	2,244,902	MUSIC
Case 7	600 x 900	359.1	130.28	2.76	2,067,753	MUSIC
Case 8a	600 x 900	350	126.98	2.76	1,984,365	FLUENT – inviscid flow
Case 8b	600 x 900	350	126.98	2.76	1,984,365	FLUENT – RSM model
Case 8c	600 x 900	350	126.98	2.76	1,984,365	FLUENT – SA model

Table 5-1 Mesh and solver details of all the different cases used

Name	**Mesh Size**	**Number of cells along the turbine height**	**Number of cells in the radial direction**	**Number of cells along the circumference of the spiral**
Coarse	1,922,837	54	72	175
Fine	3,666,012	100	72	175
Finest	5,138,953	120	96	196

Table 5-2 Grid refinement and mesh details for case 1

Figures 5-4, 5-5 and 5-6 show the coarse, fine and finest meshes used for case 1. The details of all the meshes used are tabulated in Table 5-2. The mesh is refined near the wall boundary of the turbine to incorporate the boundary layer effects. 9 cells are placed within the boundary layer at the bottom wall of the wind tunnel while 6 cells are placed

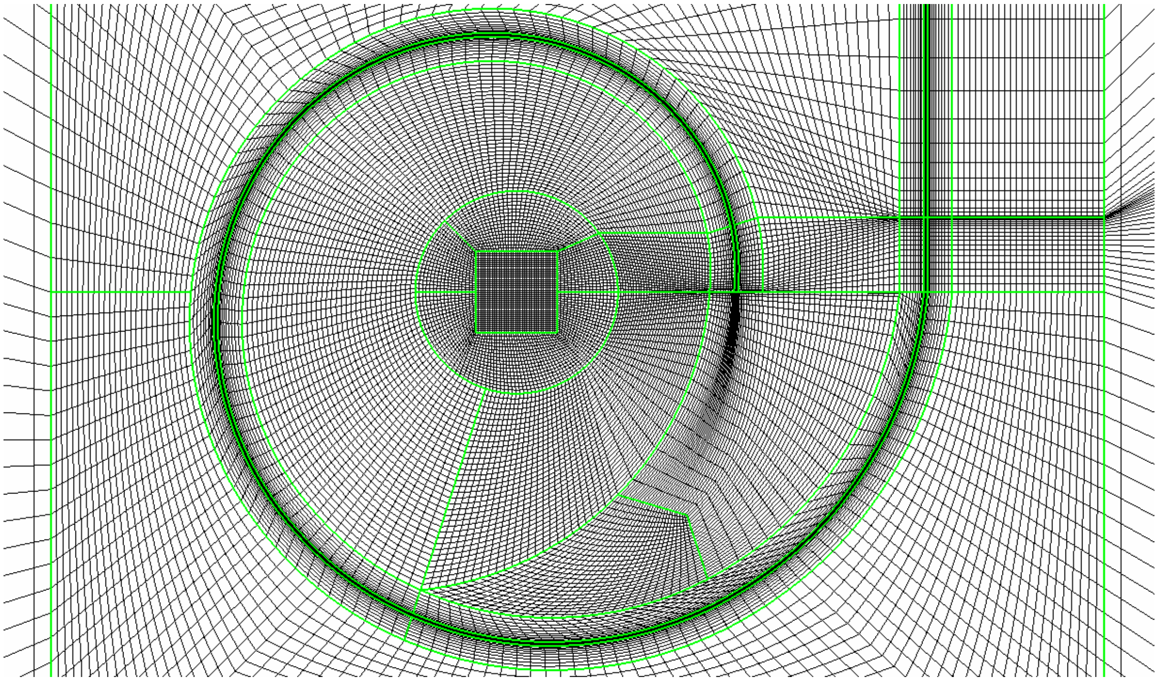

Figure 5-4 Coarse mesh for Case 1 in x-y plane

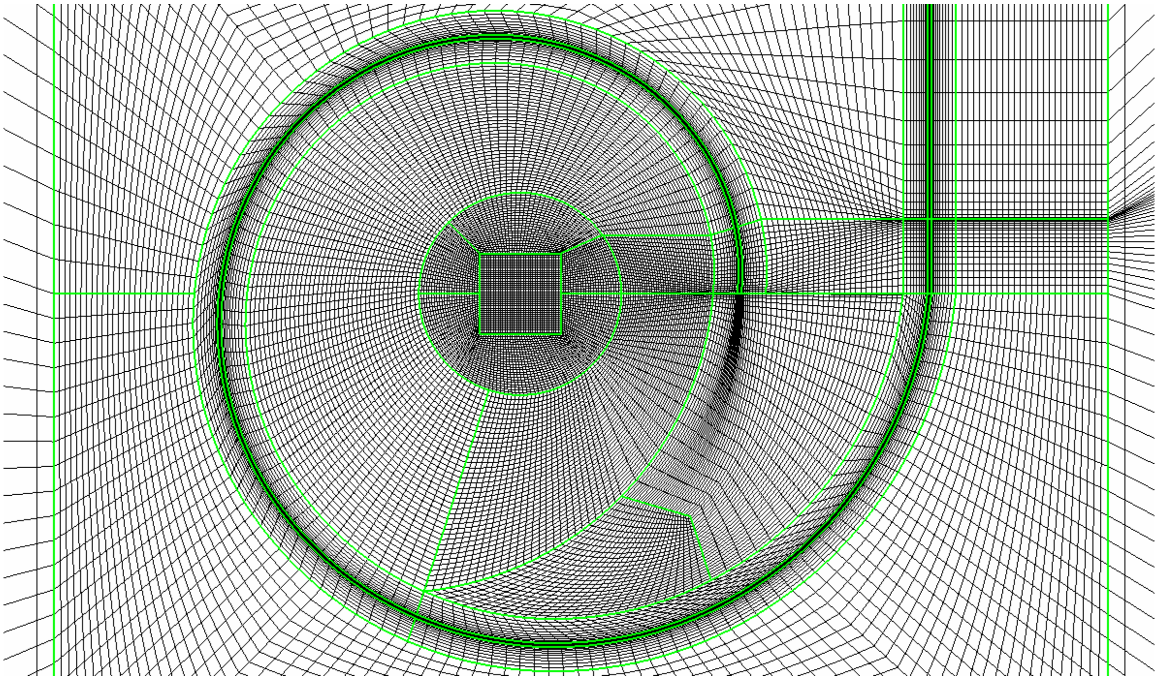

Figure 5-5 Fine mesh for Case 1 in x-y plane

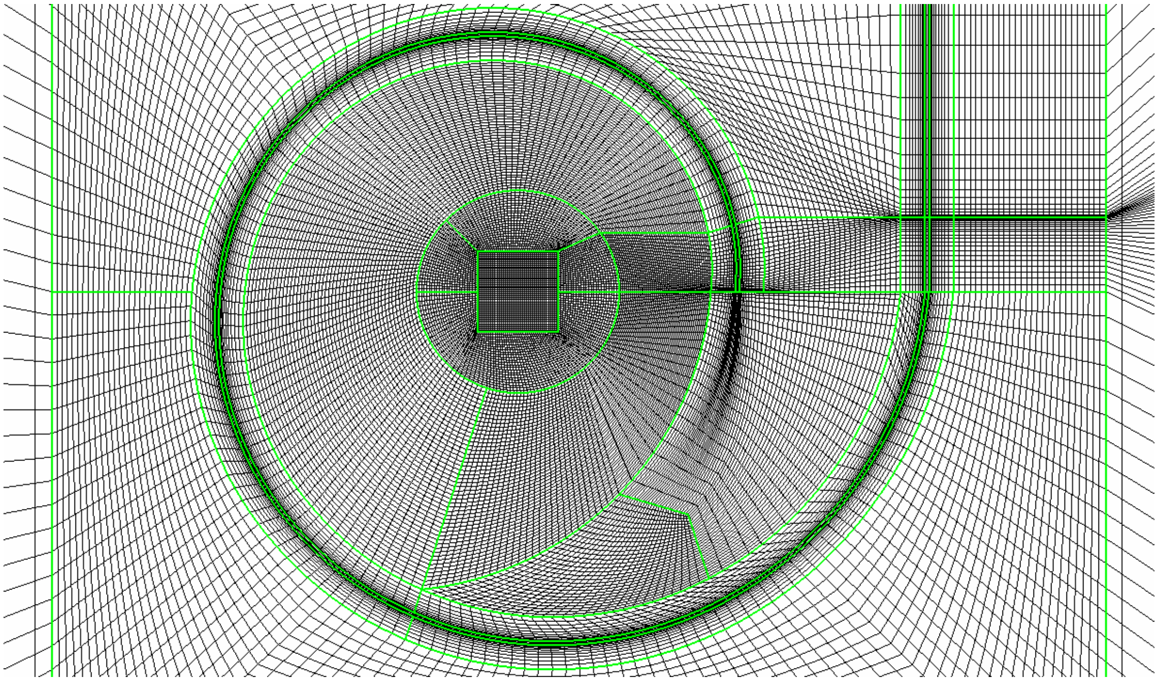

Figure 5-6 Finest mesh for Case 1 in x-y plane

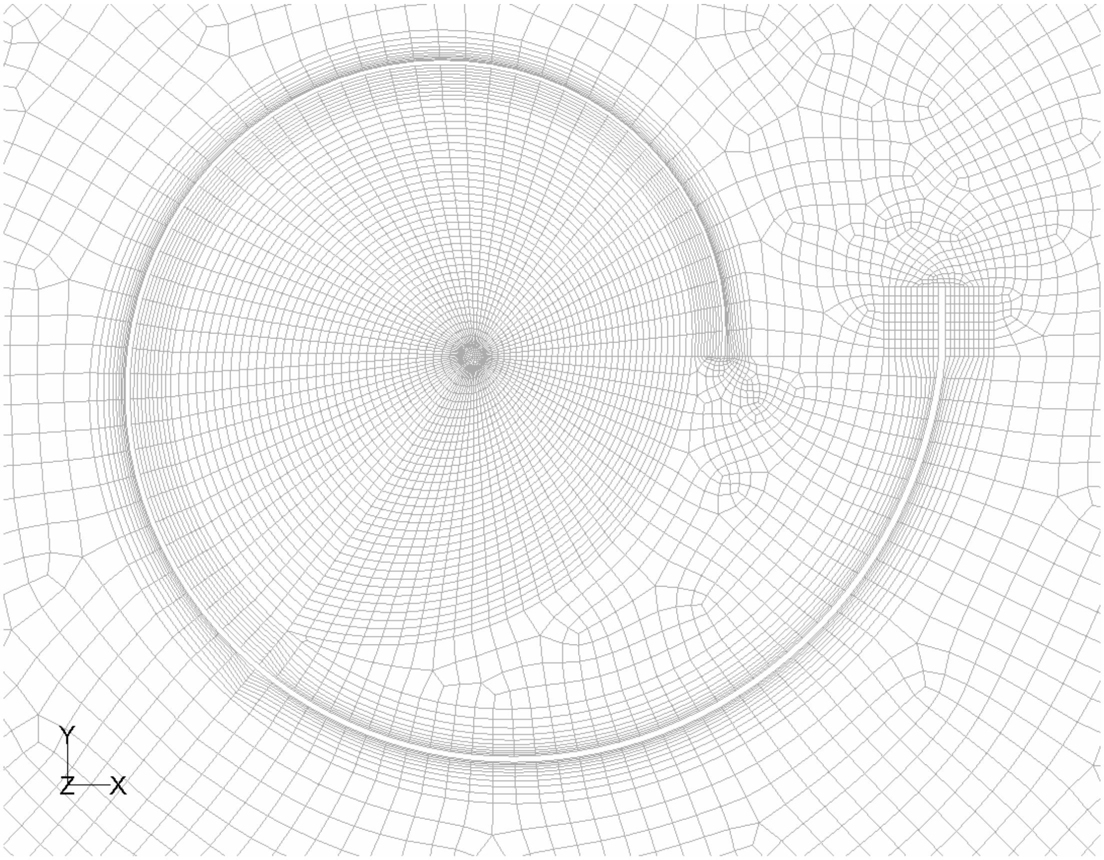

Figure 5-7 Mesh used for simulations in FLUENT

inside the boundary layer in the radial direction. The thickness of the spiral is very small i.e. of the order of a few millimeters. 8 cells are placed along the wall thickness of the spiral. Figure 5-7 shows the mesh created in GAMBIT to carry out numerical simulations using FLUENT. The mesh details are given in Table 5-1. Figures 5-8, 5-9 and 5-10 show the mesh resolution at the top end of the wind turbine wall. The number of cells placed along the turbine height (i.e. in the z-direction) increases from 54 in the coarse mesh to 120 in the finest mesh. The mesh resolution in the z-direction plays an important role in capturing the vortex strength accurately.

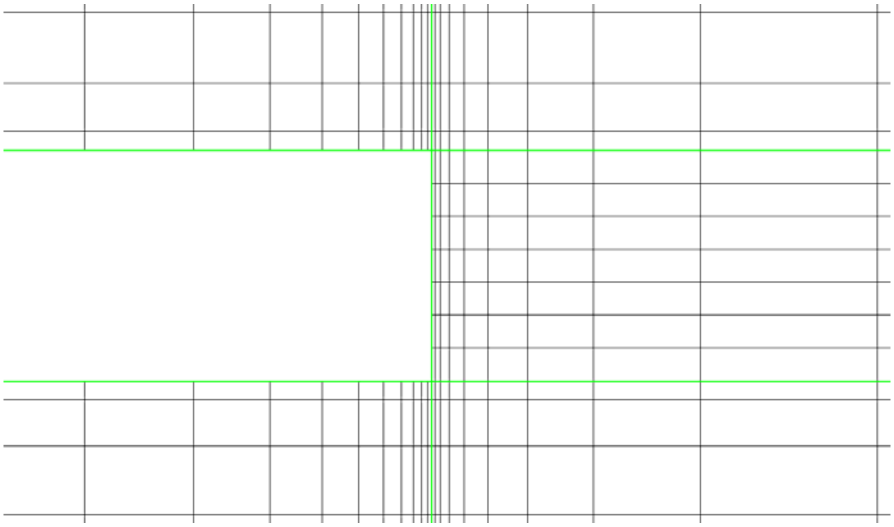

Figure 5-8 Near-wall mesh resolution for coarse mesh

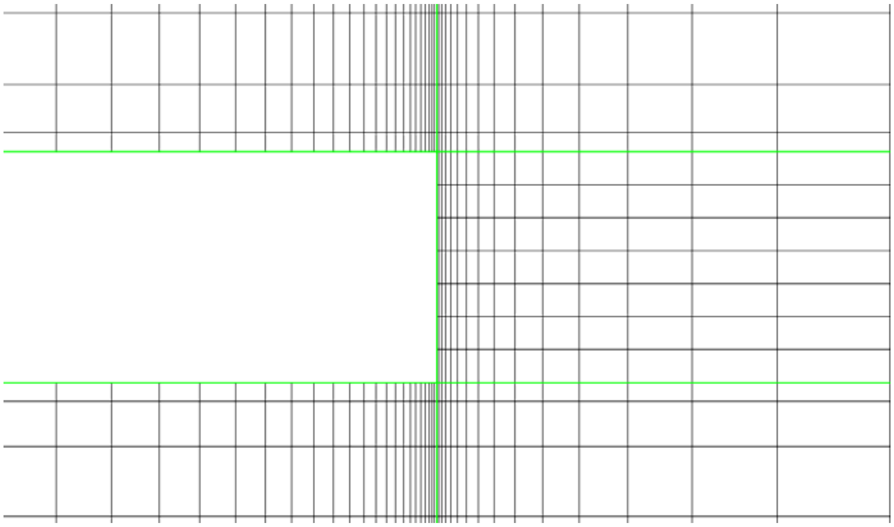

Figure 5-9 Near-wall mesh resolution for fine mesh

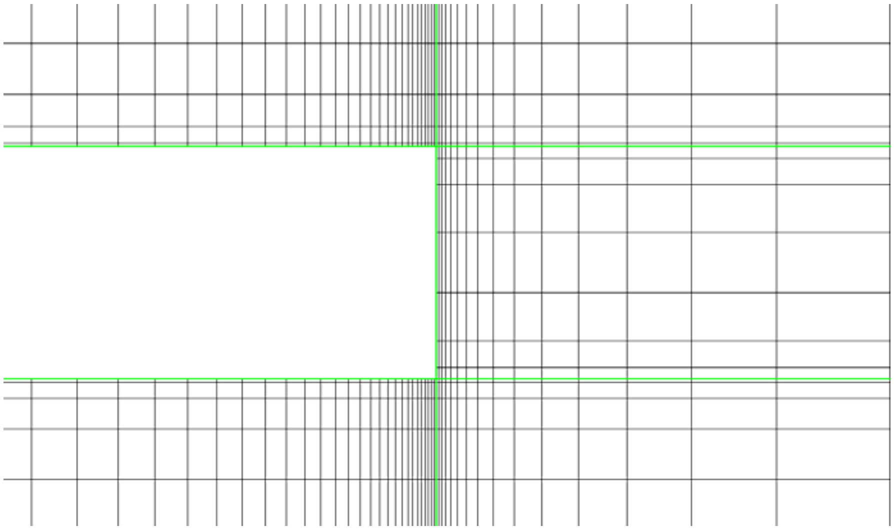

Figure 5-10 Near-wall mesh resolution for finest mesh

5.6 Results and Discussion

Design parameters which could influence the vortex strength have been realized and numerous design study and simulations have been carried out to strengthen the vortex formed inside the spiral-shaped wind turbine by varying those parameters. The aim of the entire work is to generate a strong vortex inside the turbine so that maximum power can be extracted out of it. Computational simulations were carried out to study the pressure distribution at the bottom of the turbine. The key characteristics of a TTWT include:

- a vertical axis turbine
- Uses a strong Rankine vortex to generate low pressure at the turbine exit
- Uses a stagnation chamber to generate high pressure at the turbine inlet

The low pressure developed by the vortex and the high pressure from the stagnation chamber improves the power generated by the turbine:

Power = (volume flow rate) × (change in pressure across the turbine)

The low pressure generated by the vortex of TTWT is critical to the TTWT providing an advantage over the conventional horizontal axis turbines. The vortex has a high tangential velocity and in a strong vortex this velocity is several times higher than the free stream velocity and is responsible for creating the low pressure region needed for the high turbine efficiency reported by Yen[73] and Hsu[27].

Figures 5-11 and 5-12, respectively, show the distribution of coefficient of pressure, C_p along the x and y axis (refer Figure 5-2 for axes direction) inside the spiral. The pressure distributions are measured at the bottom wall of the spiral-shaped turbine. Figure 5-11 shows the effect of grid resolution on the strength of the vortex. It can be noted that with mesh refinement the computational results get closer to the experiment results. The CFD simulations predict a stronger vortex when compared to the experiments and the difference in the minimum C_p obtained by the CFD simulations on the finest mesh and experiment is approximately 5%. This gives an indication that the mesh resolution along the axis of the vortex plays a significant role in capturing the true vortex strength. The fine and finest meshes predict a very similar C_p value.

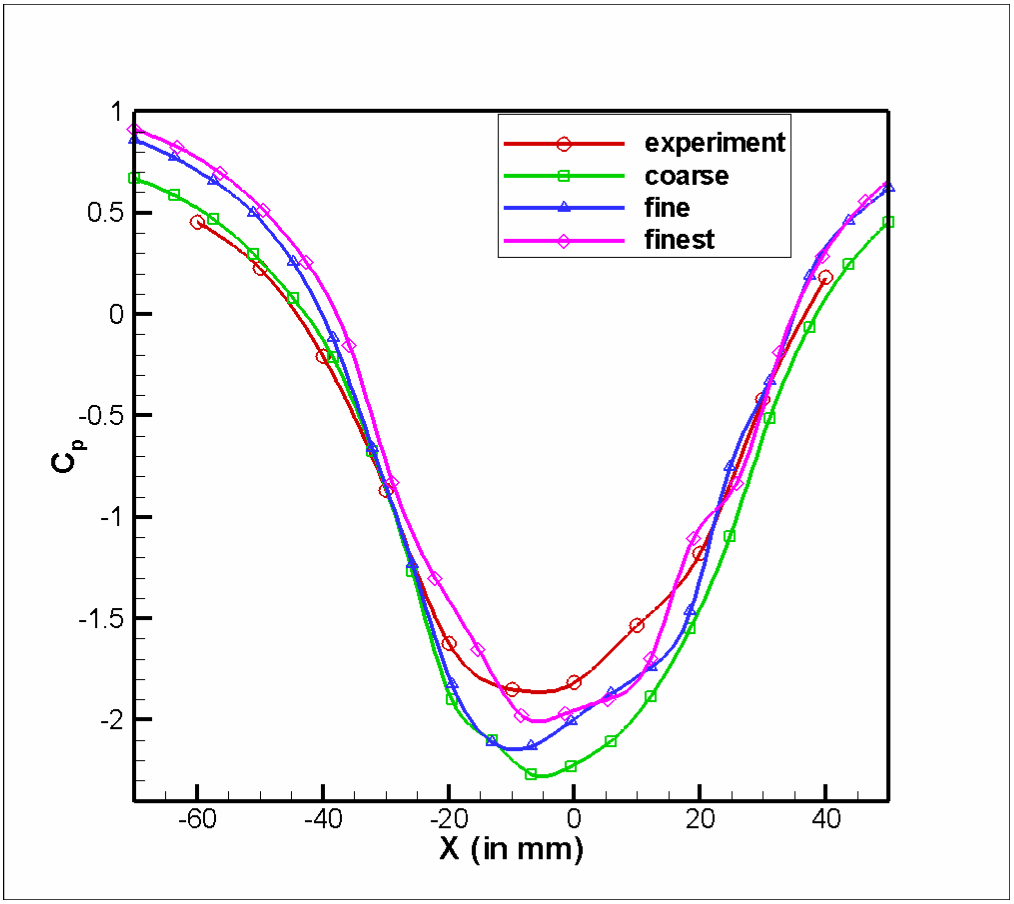

Figure 5-11 Coefficient of pressure C_p along the x-axis for different mesh sizes of case 1

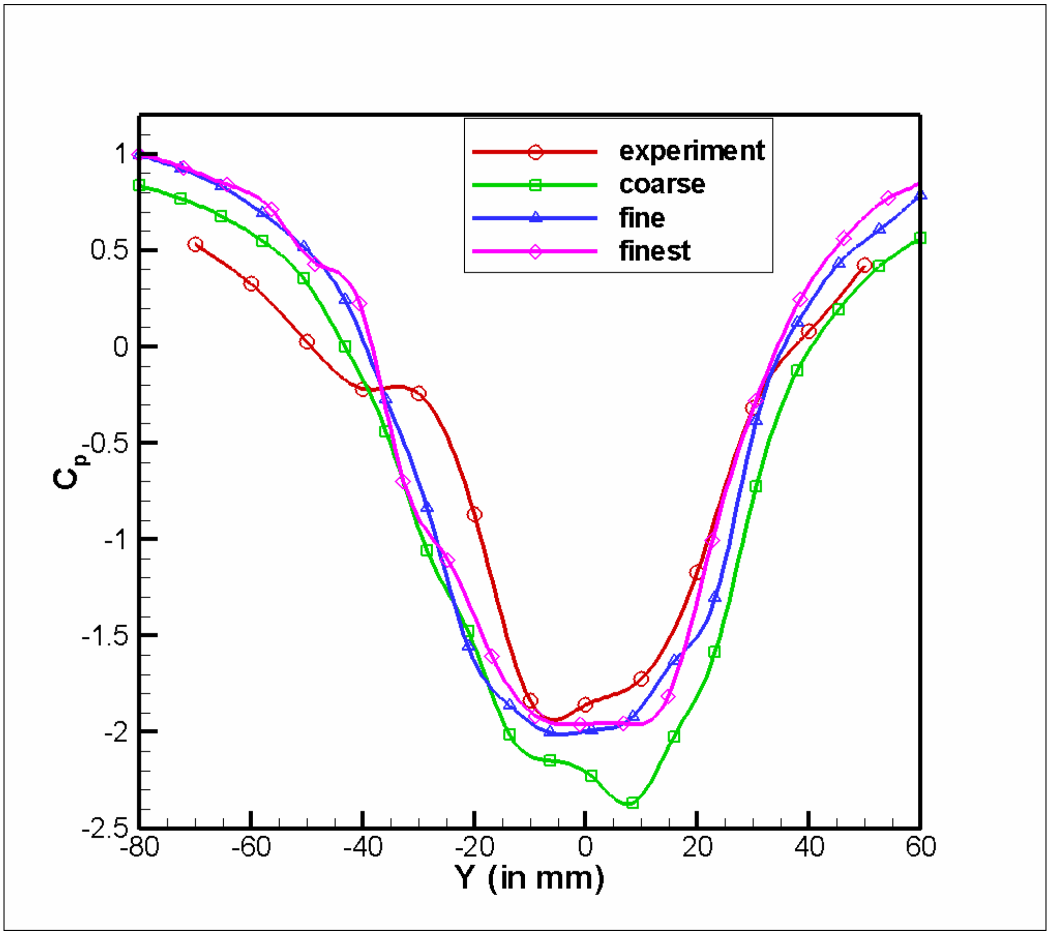

Figure 5-12 Coefficient of pressure C_p along the y-axis for different mesh sizes of case 1

Design parameters are changed to study their effects on the pressure distribution. The height of the turbine is changed from 350 mm in case 1 to 280 mm in case 2 and to 420 mm in case 3. The diameter of the spiral is unchanged to determine the influence of height H of the turbine on the vortex strength. Figures 5-13 and 5-14 show the pressure distribution along the x and y axis respectively for case 2. It can be observed that the vortex strength is highly affected by the height H of the turbine. As the height of the turbine increases, pressure gets lower and hence the strength of the vortex increases. By increasing the height by 50% (from 280 mm to 420 mm), C_p drops by 85%. This is a tremendous development and it can be concluded that by increasing the tower height the vortex can be strengthened to obtain maximum power out of the turbine.

A similar study was carried out to find the effect of diameter D of the spiral on the

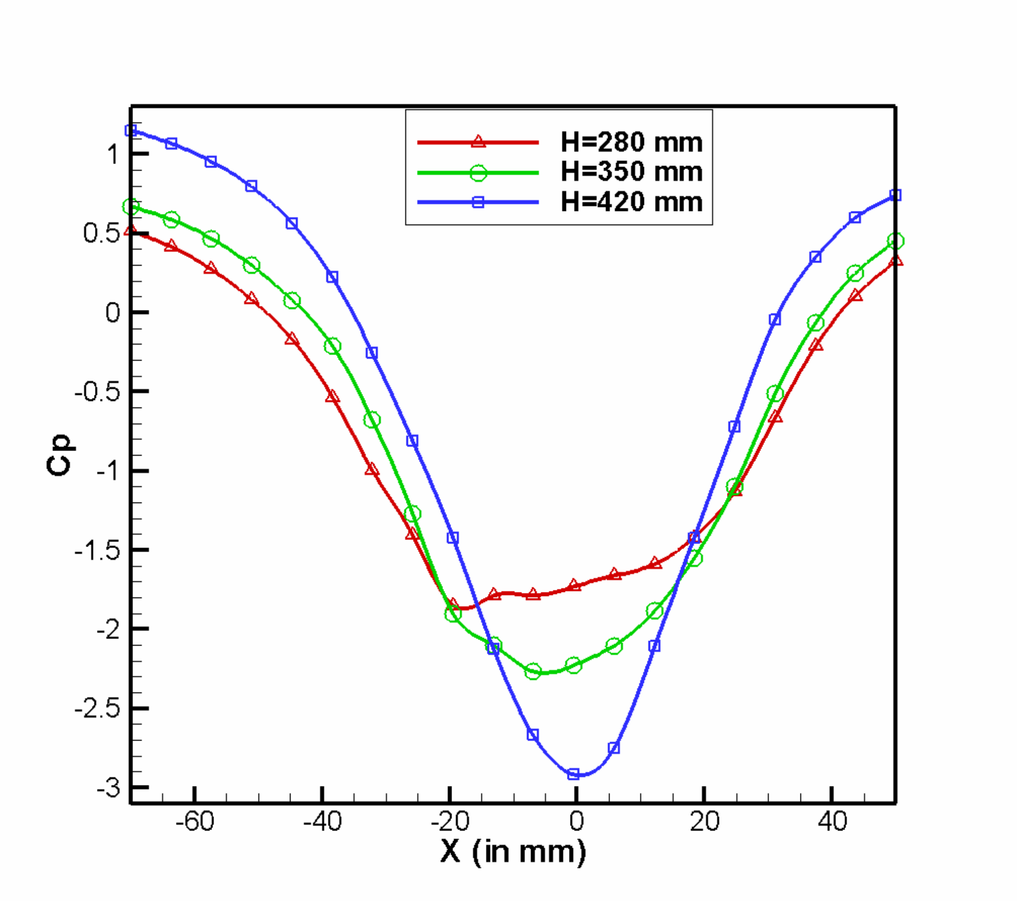

Figure 5-13 Coefficient of pressure C_p along the x-axis for different turbine heights

pressure distribution. Figures 5-15 and 5-16 show the C_p distribution. The height of the turbine was kept as 420 mm for which the lowest C_p was observed in Figures 5-13 and 5-14. The diameter of the spiral was decreased from 126.98 mm to 105.78 mm for a turbine height H equal to 420 mm. By decreasing the diameter D by 17%, C_p increases by 45%. Therefore, from Figures 5-13 to 5-16, it may be concluded that by increasing both height H and D, the vortex strength increases.

The pathlines of velocity are shown in Figure 5-17. It clearly shows the formation of a vortex inside the spiral. The wind entering the spiral swirls around inside the spiral and forms a vortex which has an axis along the turbine height and gets dissipated at the top exit of the turbine. Figure 5-18 shows the velocity pathlines in the wake of the turbine.

The strength of the vortex decreases as we go to the top of the turbine. This can be illustrated by the variation of tangential velocity at different z locations in the turbine. Figures 5-19 and 5-20 show the formation of a strong Rankine vortex inside the spiral and that its strength decreases along the z-direction. It is strongest, if not at the bottom, close to the bottom wall of the turbine. V_S is the tangential velocity in the Figures 5-19 and 5-20. Figure 5-21 clearly shows that C_p increases with increasing z-location. The plot was made for case 1. It is almost linear and clearly showing how the strength degrades as we move along the turbine axis. Figure 5-22 shows the contours of swirl velocity for case 1. At the center of the spiral, the velocities are very small and the formation of a vortex can be seen.

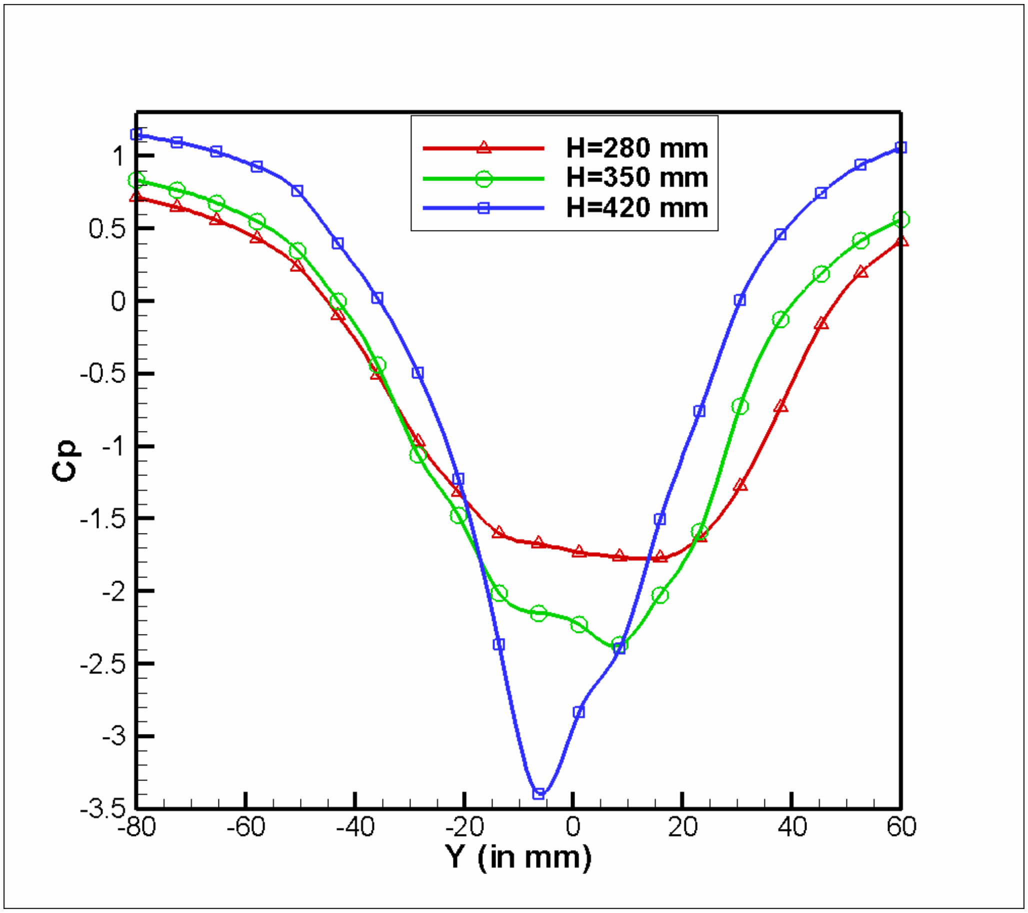

Figure 5-14 Coefficient of pressure C_p along the y-axis for different turbine heights

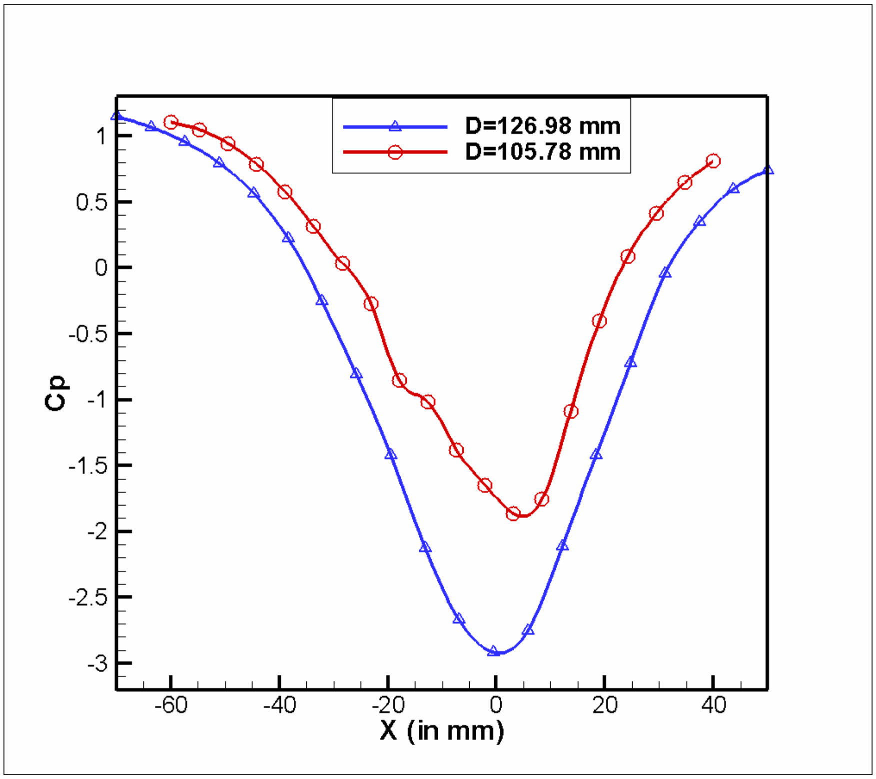

Figure 5-15 Coefficient of pressure C_p along the y-axis for different spiral diameters

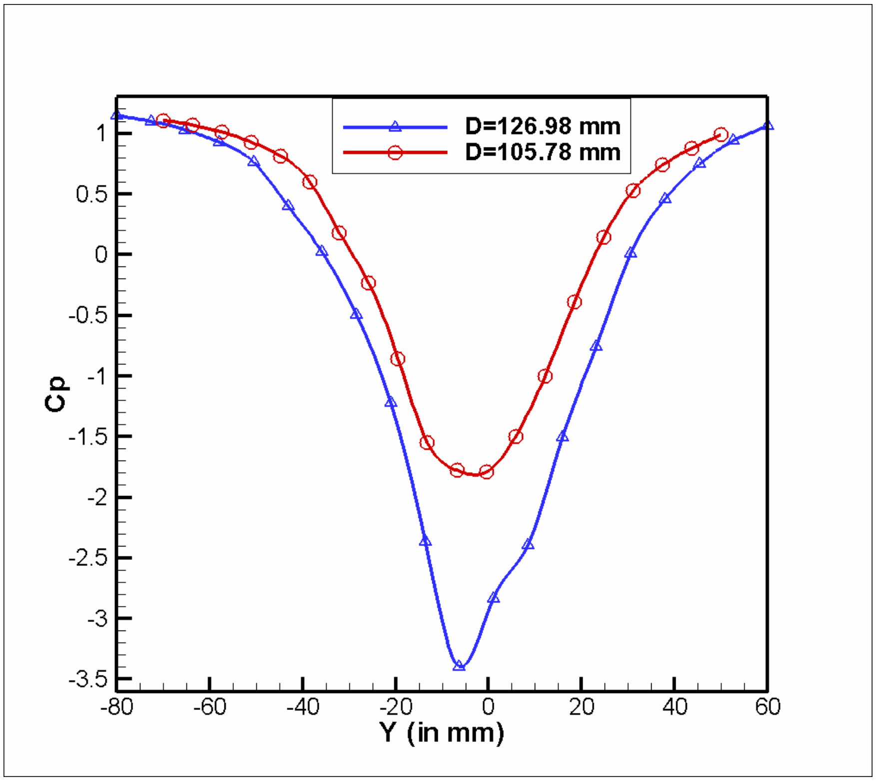

Figure 5-16 Coefficient of pressure C_p along the y-axis for different spiral diameters

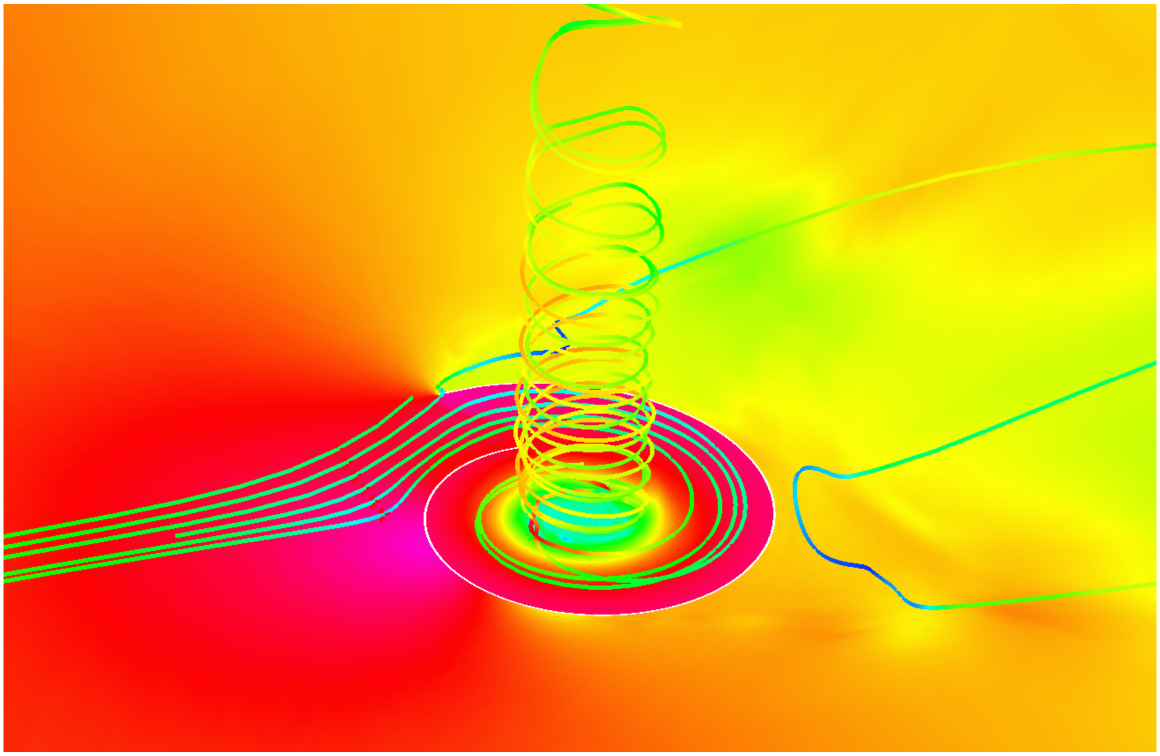

Figure 5-17 Pathlines of velocity inside the spiral

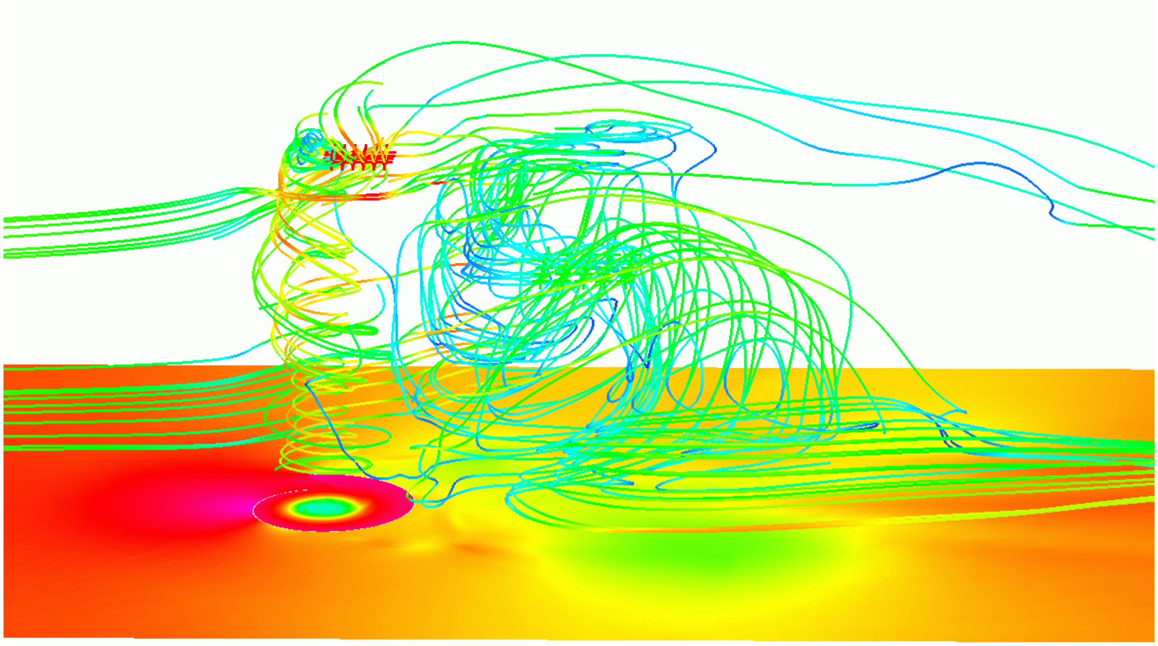

Figure 5-18 Pathlines of velocity in the wake of the turbine

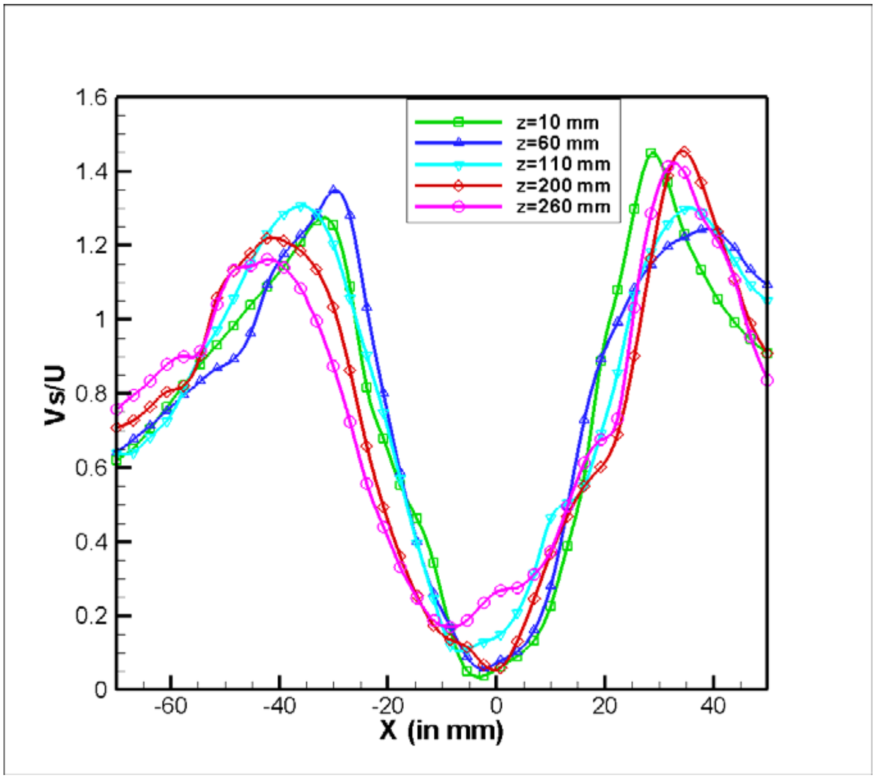

Figure 5-19 Tangential velocity along x-axis inside the spiral

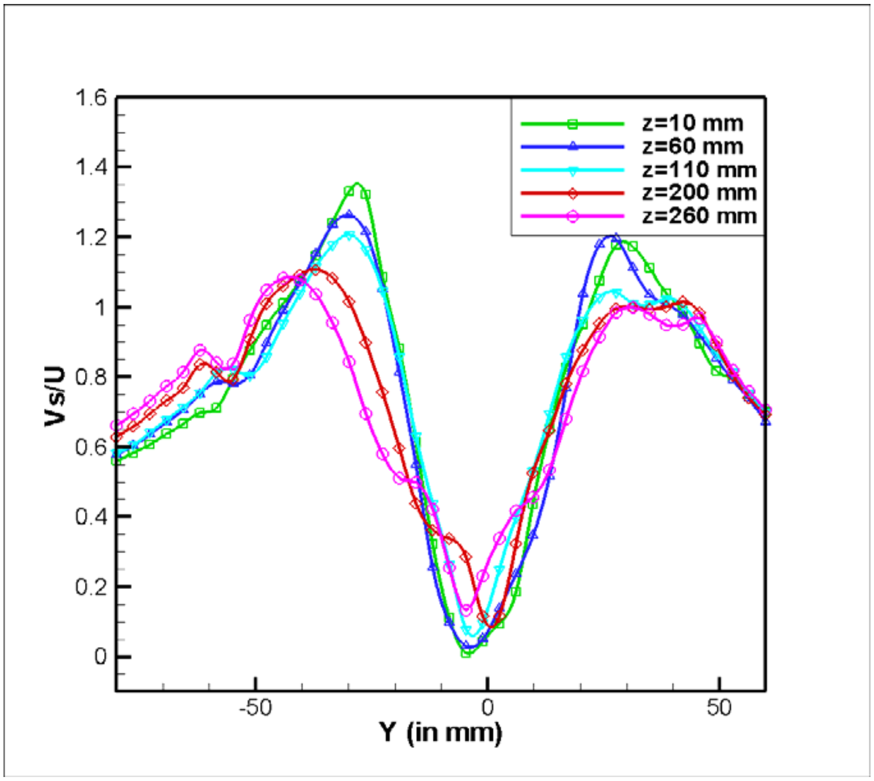

Figure 5-20 Tangential velocity along y-axis inside the spiral

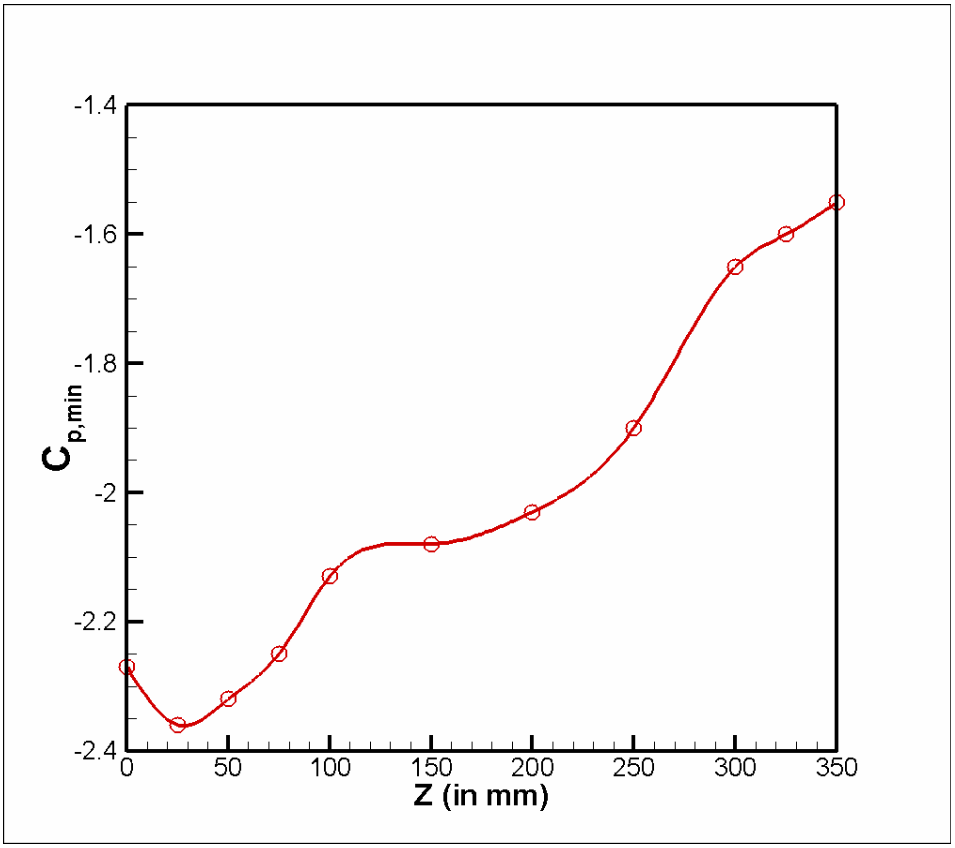

Figure 5-21 Variation of minimum C_p along turbine height for case 1

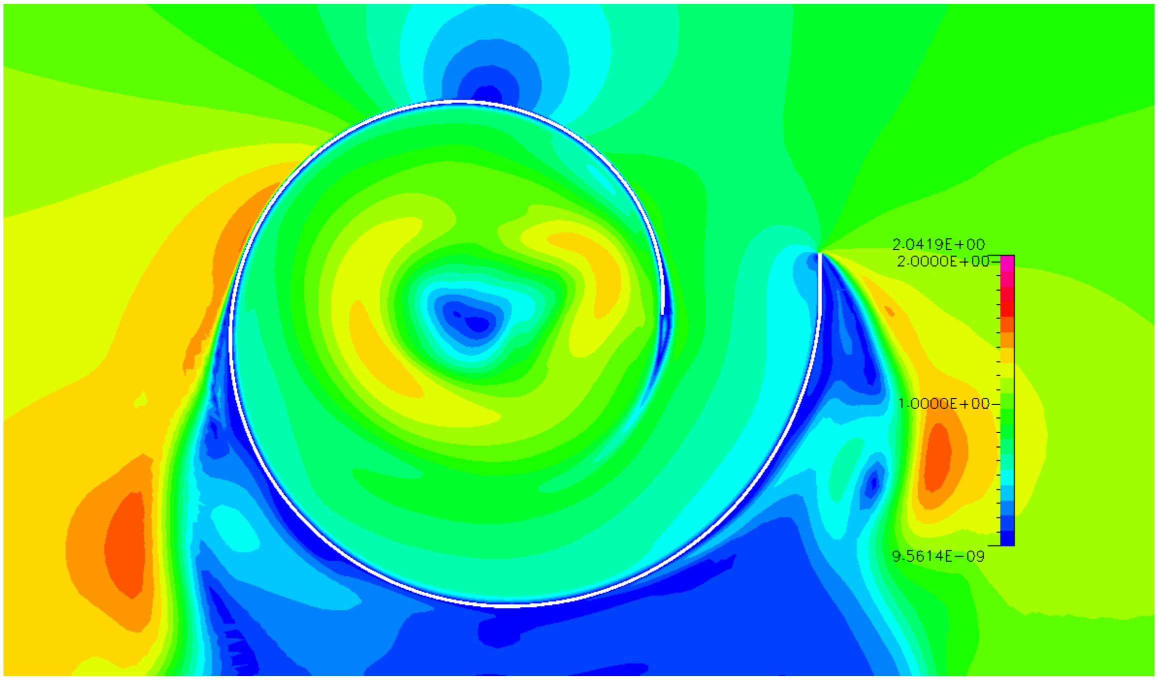

Figure 5-22 Contours of tangential (swirl) velocity for case 1

The effect of blockage ratio on the pressure distribution was also studied. This was carried out in three different wind tunnel sizes. Case 1, case 5 and case 6 correspond to these three different models (refer to Table 5-1). Blockage ratio is defined as the percentage of area occupied by a body in a wind tunnel cross section. Bigger the wind tunnel, smaller is the blockage ratio. It is noticed that the blockage ratio has very little effect on the vortex strength. Figures 5-23 and 5-24 justify the statement.

Figures 5-25 and 5-26 show the pressure distribution of three different cases – case 1, case 4 and case 7. The model is case 4 is obtained by increasing the inlet of the spiral by 20%. Hence the shape of the spiral for case 4 is different from that of case 1 and case 7. This shape of the spiral can be changed by changing the value of constant α in the equation $r = r_o e^{-\alpha\theta}$ mentioned before. The height of turbine for case 4 is made in such a way that the ratio H/D remains the same as in case 1 (equal to 2.76). From Figures 5-25 and 5-26, it can be understood that H/D ratio doesn't play a significant role in the vortex strength.

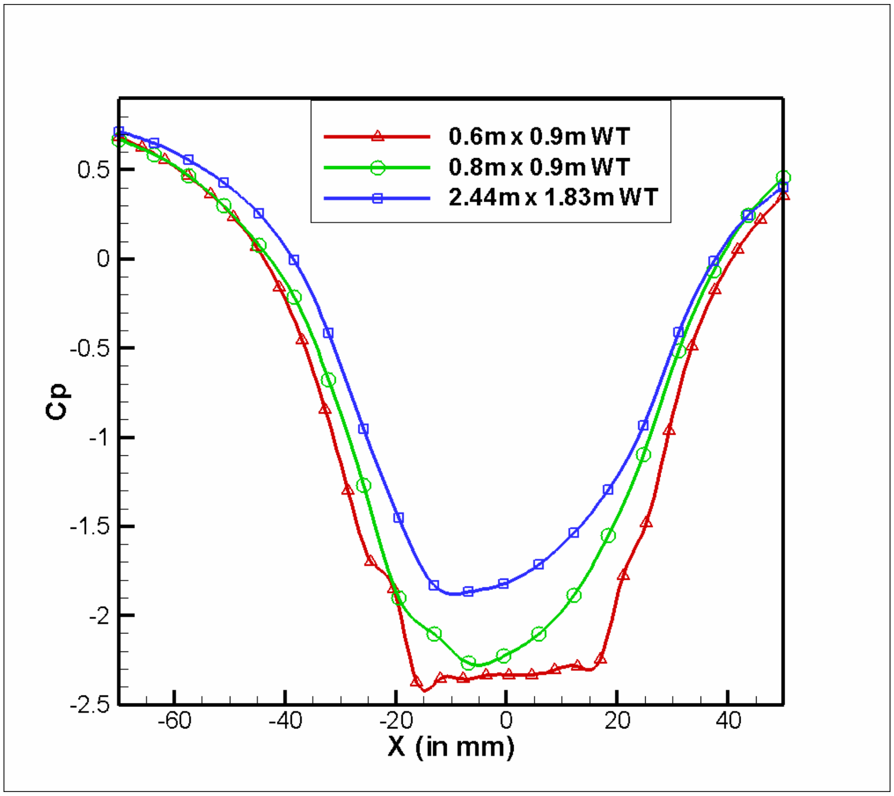

Figure 5-23 Coefficient of pressure C_p along the x-axis for different Wind Tunnel cross-sections

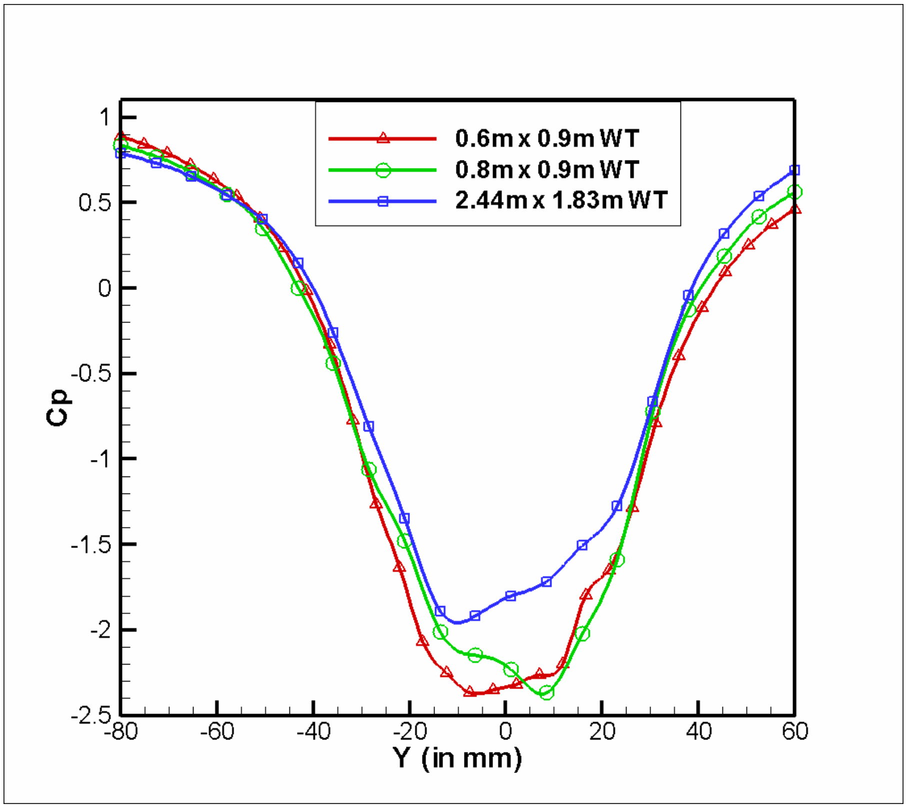

Figure 5-24 Coefficient of pressure C_p along the y-axis for different Wind Tunnel cross-sections

Numerical simulations were carried out with FLUENT as well. An inviscid run was made for a coarse mesh (Figure 5-7). The inviscid fluid flow i.e. case 8a, would predict the lowest C_p because it does not include any viscous effects which reduce the vortex strength. Later on, Reynolds Stress Model (RSM) and Spallart-Almaras (SA) model were used. The pressure distribution at the bottom wall of the turbine is shown in Figures 5-27 and 5-28. As expected, the inviscid flow calculation predicts the strongest vortex. The results from FLUENT are compared with the ones obtained for case 5 with MUSIC. The mesh sizes are similar for both the cases. Case 8b which uses RSM turbulence model is in good agreement with the experiment results. Case 8c which uses SA turbulence model predicts a lower value of C_p. This is as expected because RSM is the most elaborate turbulence model that FLUENT provides. RSM accounts for the effects of streamline curvature, swirl, rotation, and rapid changes in strain rate in a more rigorous manner than one-equation model like SA. RSM has greater potential to give accurate predictions of complex flows than the SA model because SA model is a one

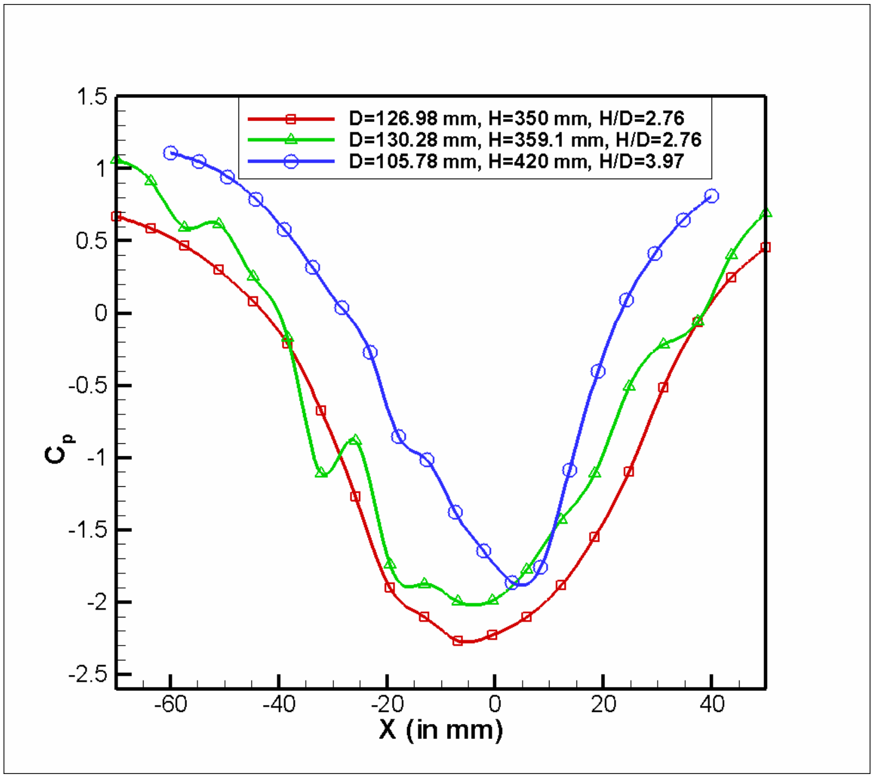

Figure 5-25 Coefficient of pressure C_p along x-axis for cases 1, 4 and 7

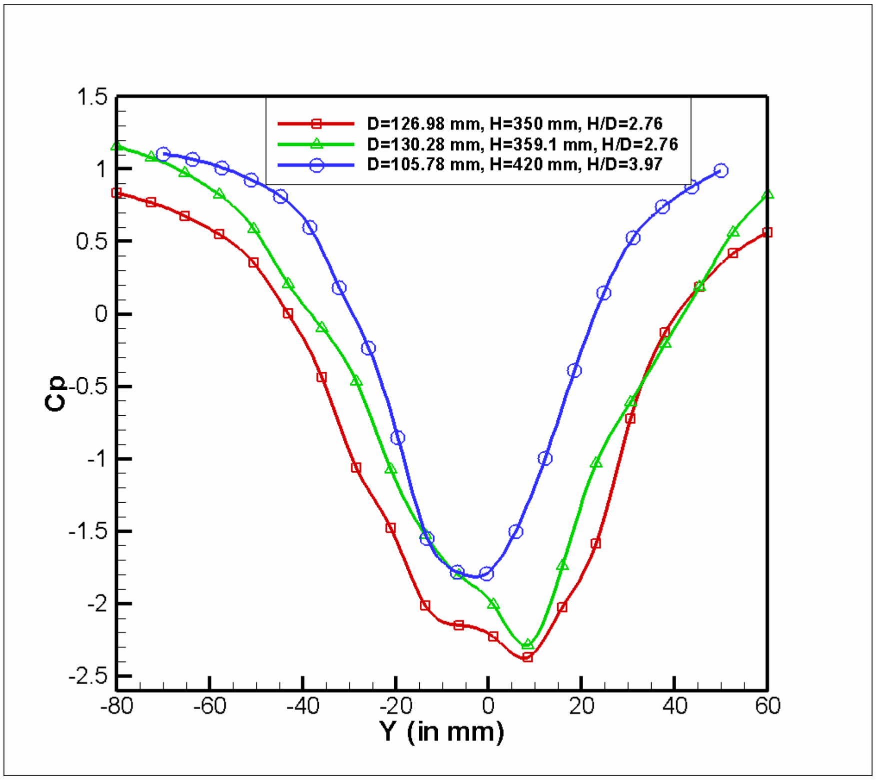

Figure 5-26 Coefficient of pressure C_p along y-axis for cases 1, 4 and 7

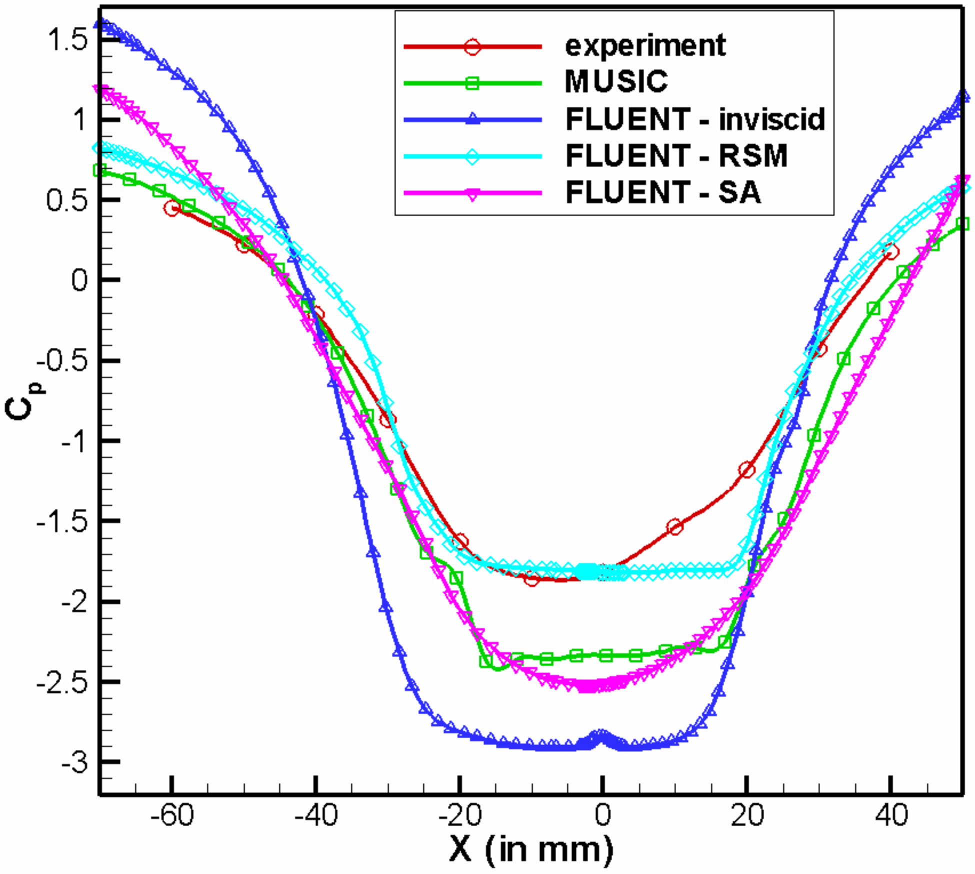

Figure 5-27 Comparison of coefficient of pressure C_p along x-axis for cases 1, 4 and 7 with experiment

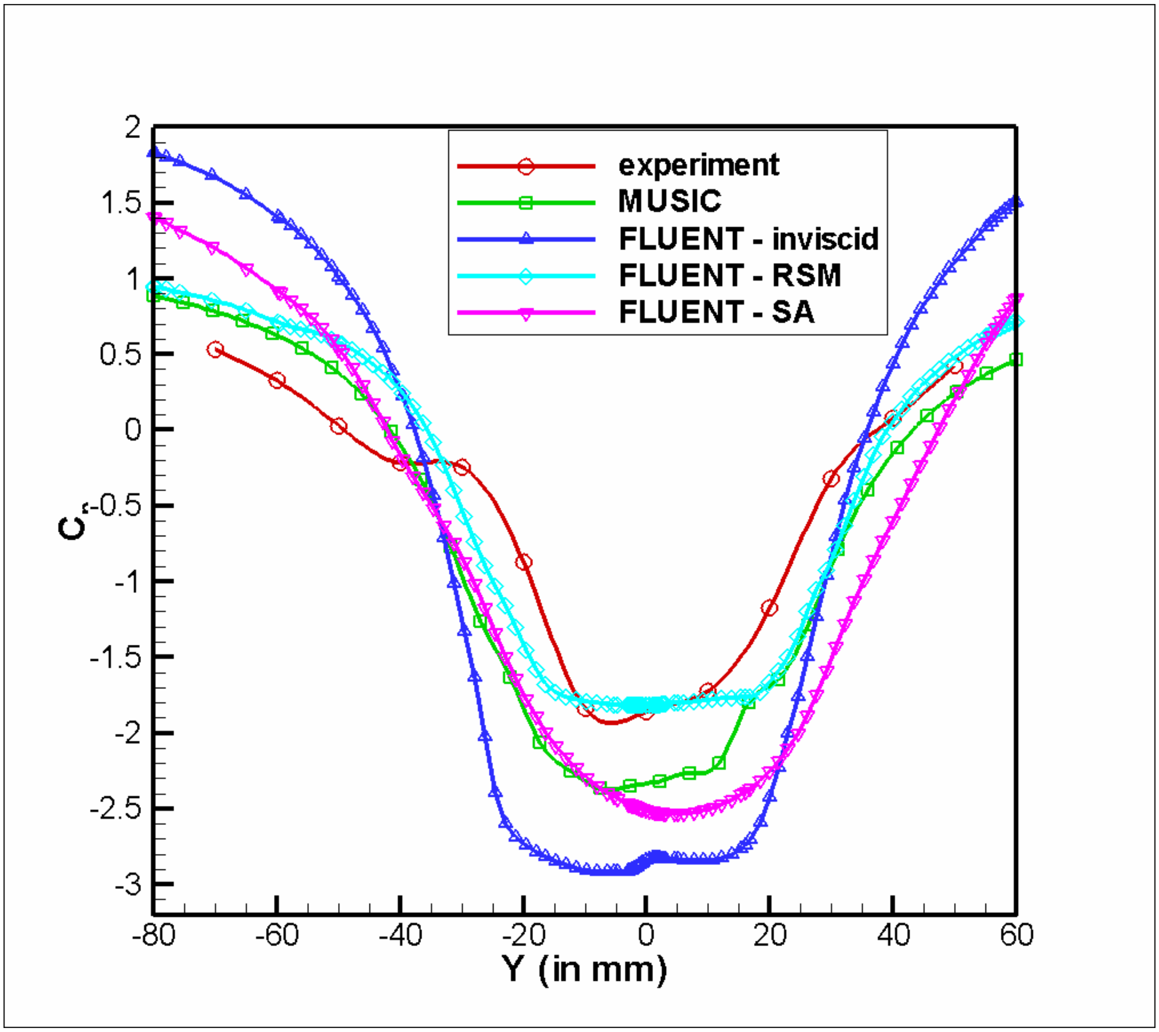

Figure 5-28 Comparison of coefficient of pressure C_p along y-axis for cases 1, 4 and 7 with experiment

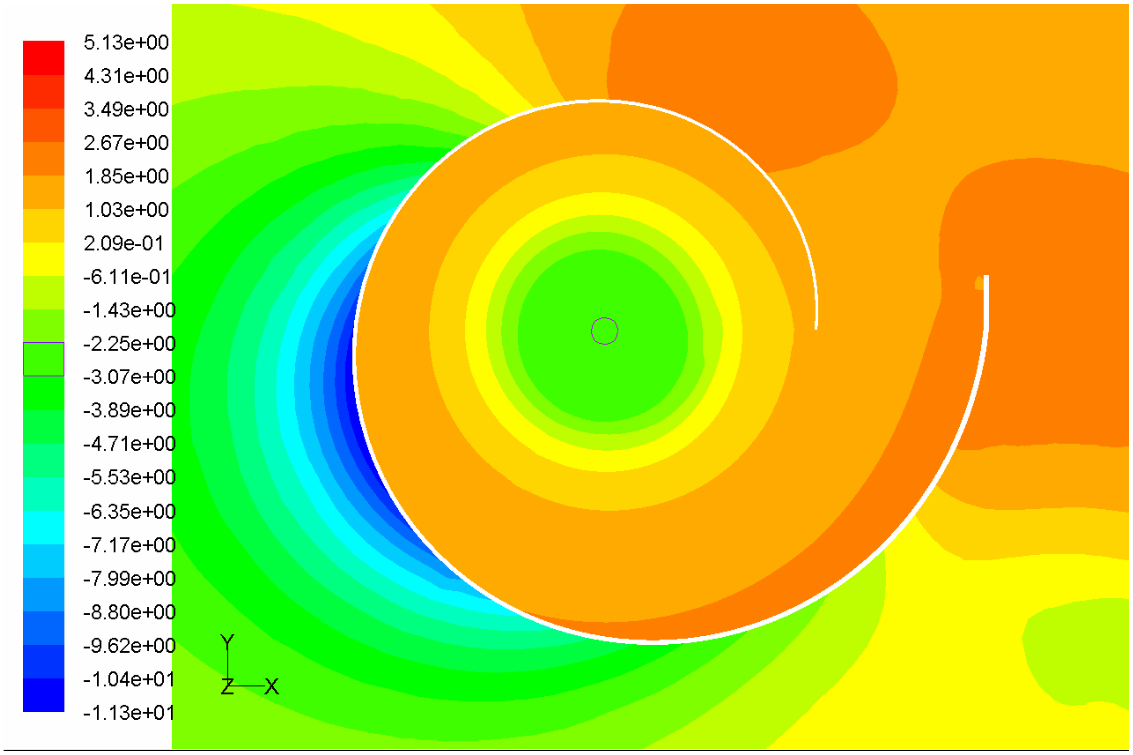

Figure 5-29 Contours of coefficient of pressure C_p for inviscid flow using FLUENT

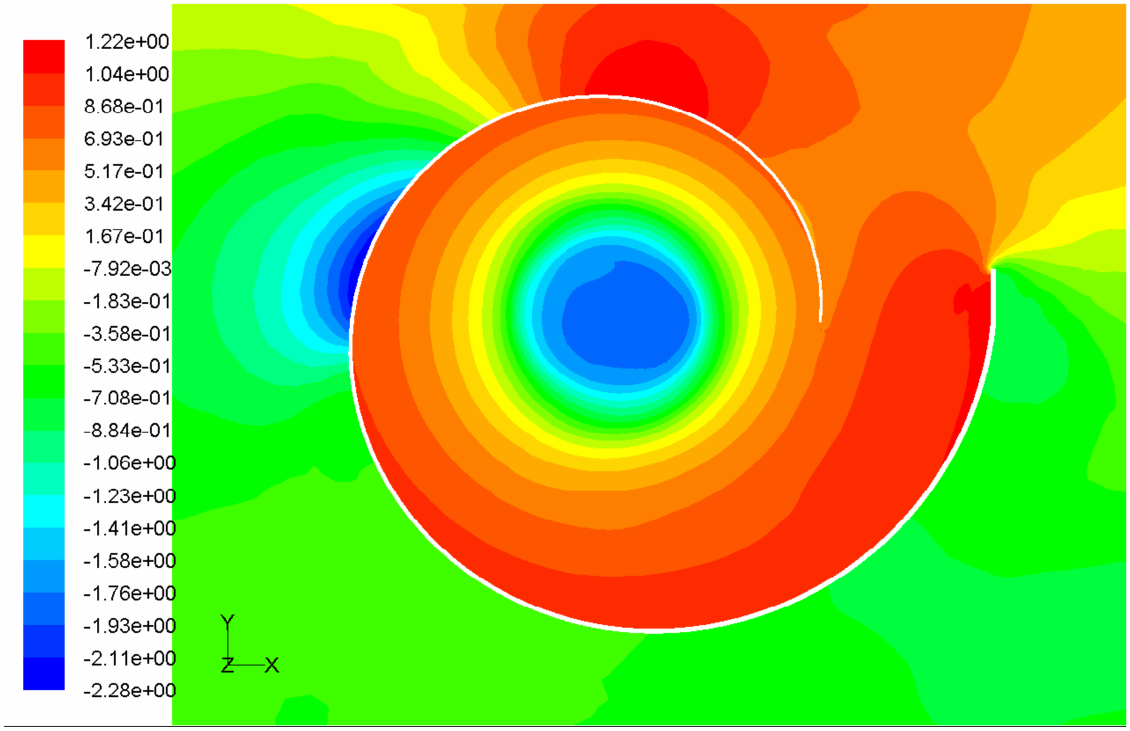

Figure 5-30 Contours of coefficient of pressure C_p for viscous flow using FLUENT with RSM model

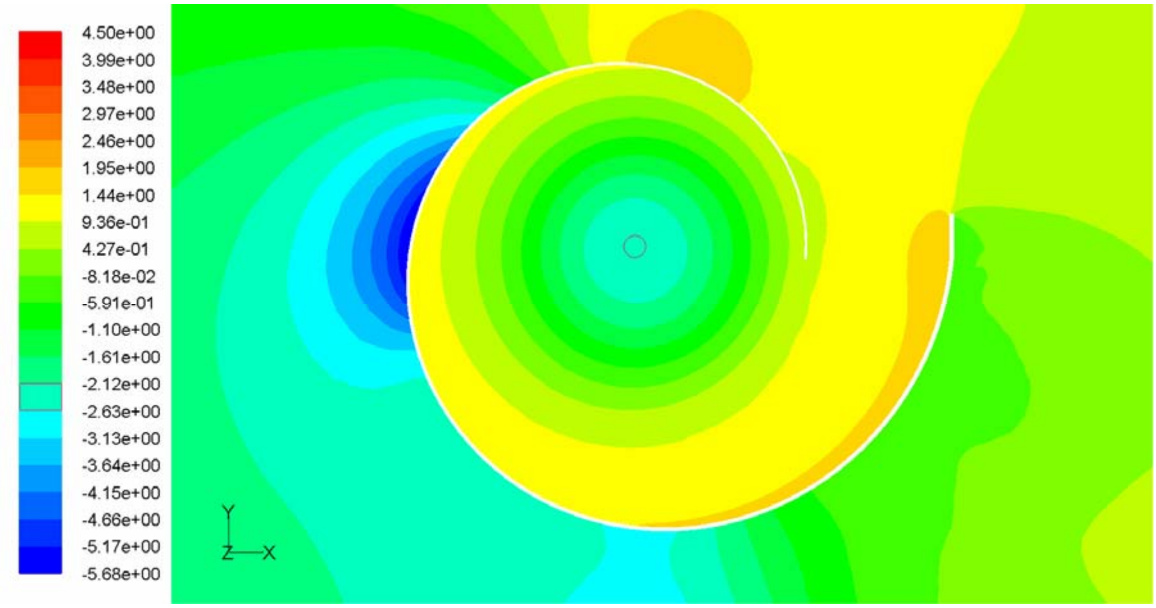

Figure 5-31 Contours of coefficient of pressure C_p for viscous flow using FLUENT with SA model

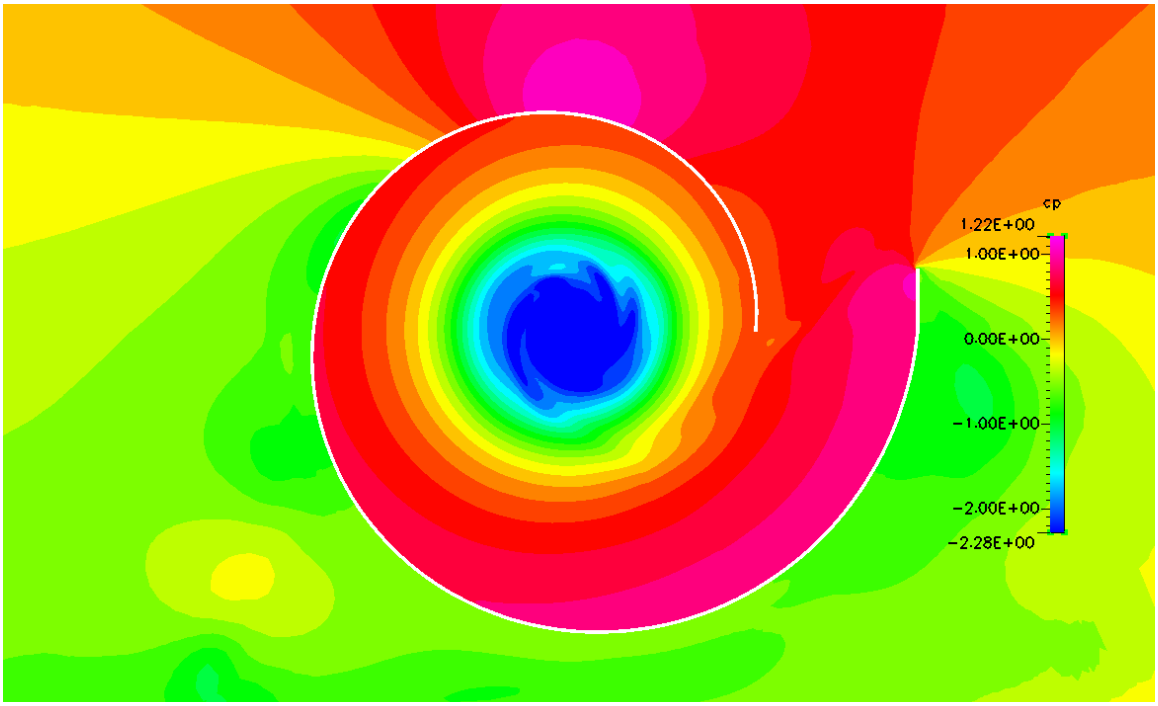

Figure 5-32 Contours of coefficient of pressure C_p for the finest mesh using MUSIC

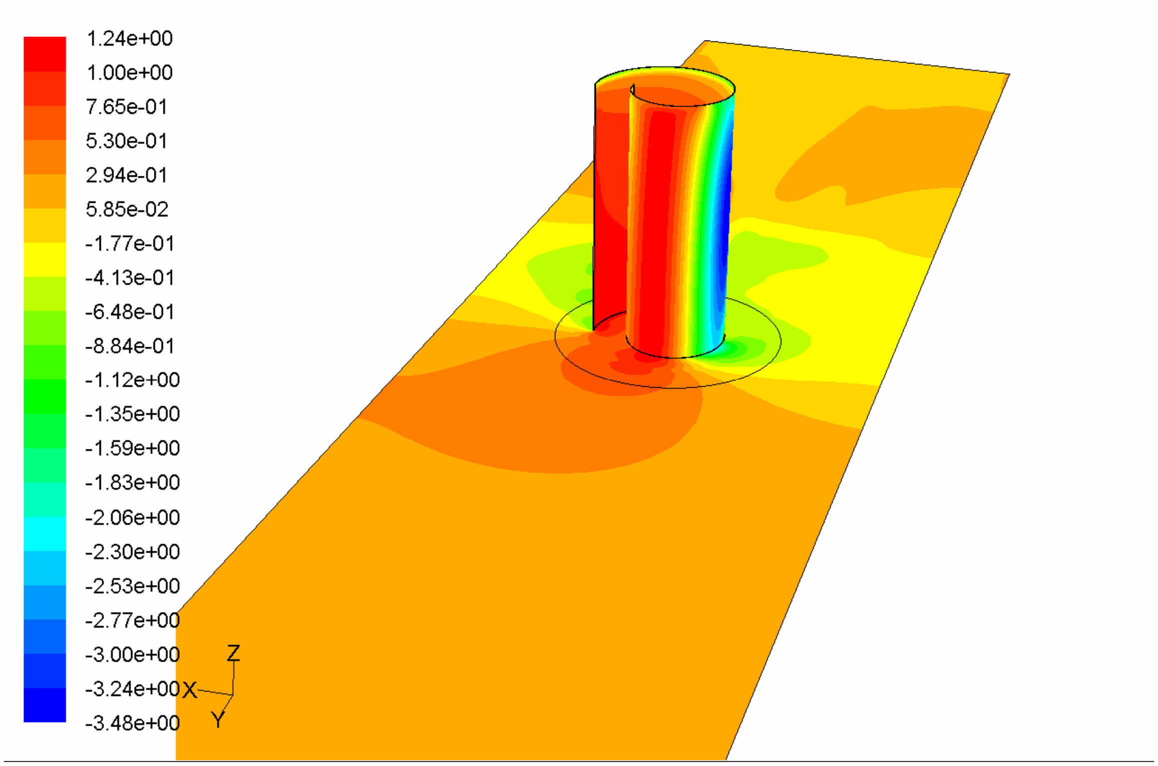

Figure 5-33 Coefficient of pressure C_p distribution on the turbine wall

equation model and hence is expected to be less accurate. Contours of pressure coefficient for all the cases using FLUENT and for the finest mesh using MUSIC are shown in Figures 5-29 to 5-32. These figures give a good comparison of the pressure values at the base of the turbine. Figure 5-33 shows the pressure distribution along the wind tunnel and the turbine walls. A very low pressure area can be seen on the turbulent walls. This is because of the acceleration of the flow due to a high radius of curvature. Figure 5-34 shows the contours of vorticity magnitude on the base of the turbine. A very strong vortex is formed at the center.

As mentioned before, it is important to note the vortex strength along the turbine height. The variation of the vortex strength can be understood from Figure 5-21. In addition to that, Figure 5-34 showing the contours of pressure coefficient in the y-z plane (at x=0), justifies that the vortex strength degrades with the turbine height. Figure 5-35 shows the contours of Mach number and the small values (almost zero) suggest the presence of the vortex at the center of the turbine.

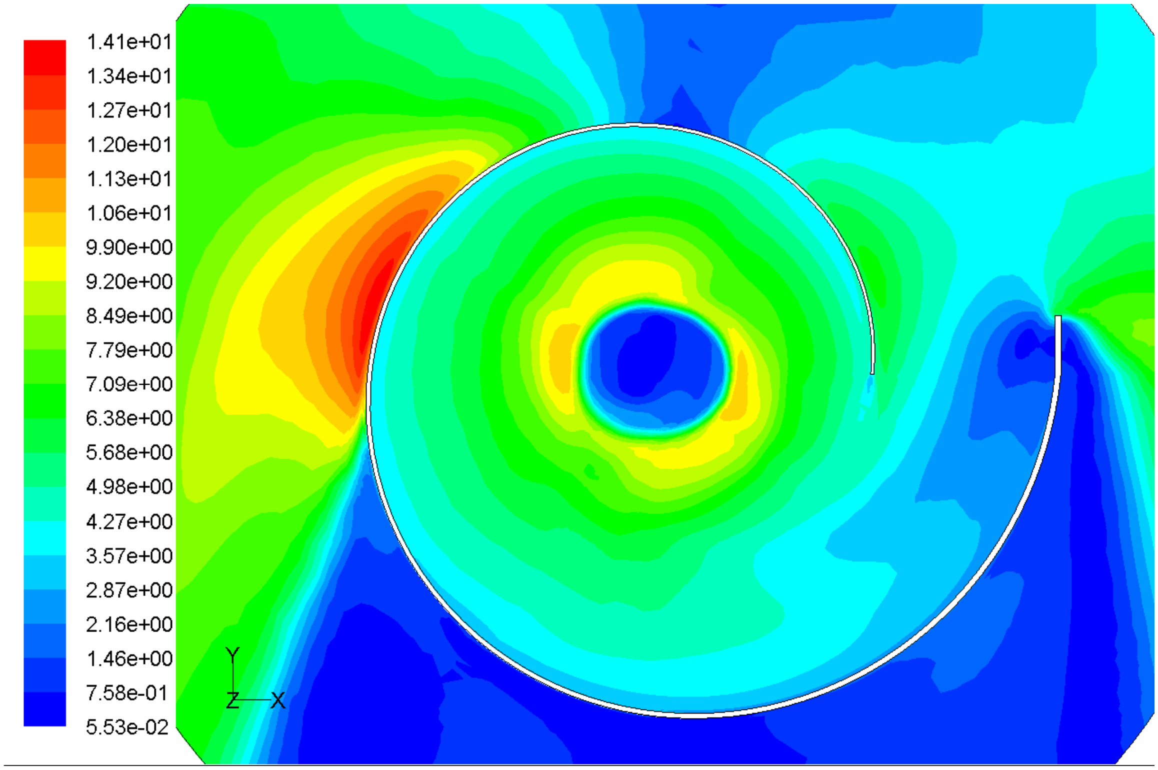

Figure 5-34 Contours of vorticity magnitude using FLUENT

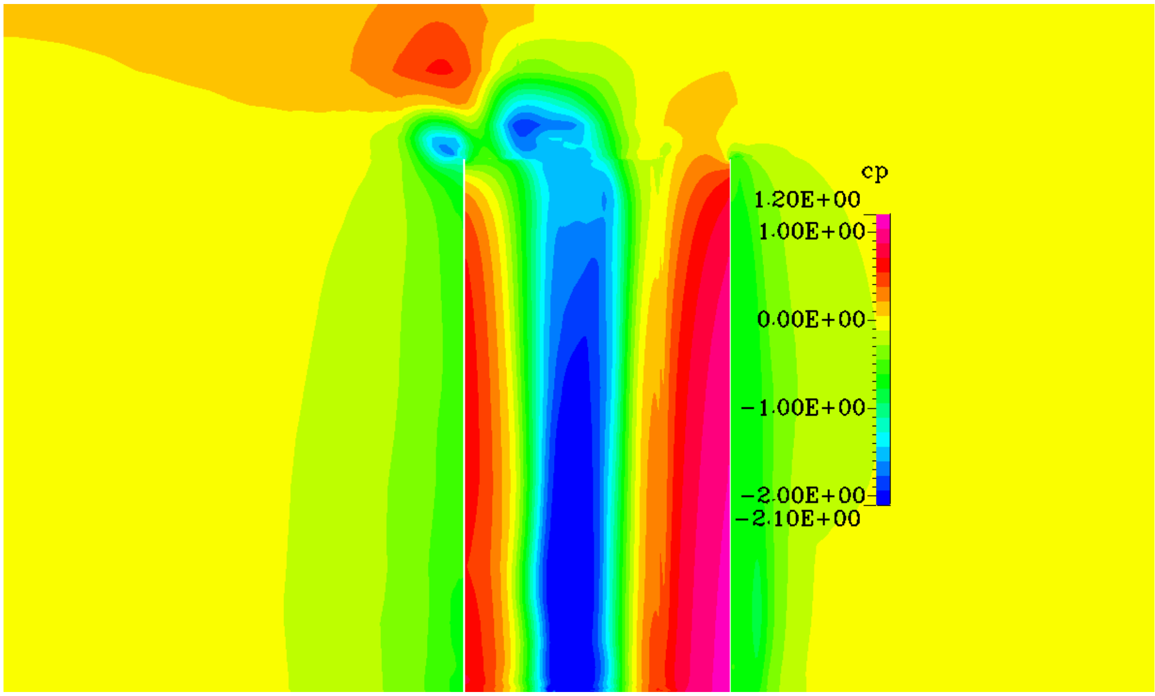

Figure 5-35 Contours of pressure coefficient in the y-z plane

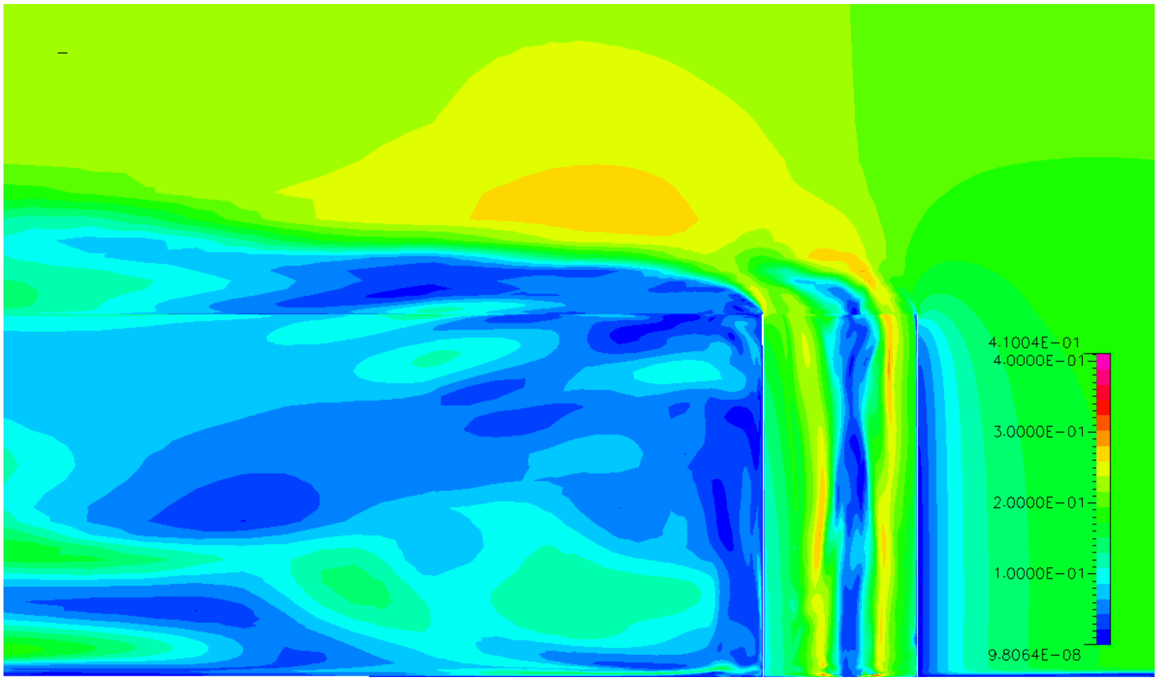

Figure 5-36 Contours of Mach number in the y-z plane

5.7 Conclusions and Future Work

The present work gives a good understanding of the Tornado-Type Wind Energy System. The computational simulations and experiment results show the formation of a Rankine vortex in the center of the turbine which is a characteristic of a TTWT. The numerical simulations carried out by FLUENT and MUSIC produce similar results. The numerical results and experiment results differ by just 5-10%. Grid refinement study was also carried out to assess any numerical errors. The finest mesh results match extremely well with the experiment results suggesting the importance of grid resolution along the turbine height. The effects of various geometry parameters like diameter of the spiral and height of the turbine are studied. The results show the formation of a not-so-strong vortex. More research needs to be carried out to reduce the static pressure even more by making design changes.

In the current work, static pressure surveys were made on the tower bottom with the vortex alone in a tower having a solid bottom. A study can be made with a turbine at the bottom of the turbine which exhausts into the core of the vortex. Hsu et al[27] showed that with the presence of a turbine at the bottom, the static pressure measurements were reduced which means the strengthening of the vortex. This could be because of the fact that with the solid bottom, the vortex is bounded. This is a well proven fact[37] that a vortex can be strengthened by injecting a flow into its core if the flow is in the forward direction of the vortex axial velocity. In this way, there is a possibility that the vortex is strengthened when the turbine is installed to the exhaust into the core of the vortex.

Bibliography

1. T. J. Barth, and P. O. Frederickson, “High-order solution of the Euler equations on unstructured grids using quadratic reconstruction”, AIAA Paper No. 90-0013, 1990.
2. P. Beaudan, and P. Moin, “Numerical experiments on the flow past a circular cylinder at a subcritical Reynolds number”, *Technical report TF-62, Thermosciences Division, Department of Mechanical Engineering, Stanford University*, 1994.
3. Michael Breuer, “Large eddy simulation of the subcritical flow past a circular cylinder: numerical and modeling aspects”, *International Journal for Numerical Methods in Fluids*, Vol. 28, 1998, pp. 1281-1302.
4. Michael Breuer, “Numerical and modeling influences on large eddy simulations for the flow past a circular cylinder”, *International Journal of Heat and Fluid Flow*, Vol. 19, 1998, pp. 512-521.
5. C. Canuto, M. Y. Hussaini, A. Quarteroni, and T. A. Zang, “Spectral Methods in Fluid Dynamics”, *Springer-Verlag*, New York, 1987.
6. P. Catalano, M. Wang, G. Laccarino, and P. Moin, “Numerical simulation of the flow around a circular cylinder at high Reynolds numbers”, *International Journal of Heat and Fluid Flow*, Vol. 24, 2003, pp. 463-469.
7. R.F. Chen, and Z.J. Wang, “Fast, Block Lower-Upper Symmetric Gauss-Seidel Scheme for Arbitrary Grids”, *AIAA Journal*, 2000, Vol. 38, no. 12, pp. 2238-2245.
8. C. K. Chyu, and D. Rockwell, “Near wake structure of an oscillating cylinder: Effect of controlled shear layer vortices”, *Journal of Fluid Mechanics*, Vol. 322, 1996, pp. 21-49.
9. B. Cockburn, and C. W. Shu, “The Runge-Kutta discontinuous Galerkin method for conservation laws V: multidimensional systems”, *Journal of Computational Physics*, Vol. 141, 1998, pp. 199-224.
10. B. Cockburn, and C. W. Shu, “TVB Runge-Kutta local projection discontinuous Galerkin finite element method for conservation laws II: General framework”, *Math. Comput.*, Vol. 52, 1989, pp. 411.

11. M. Delanaye, and Y. Liu, “Quadratic reconstruction .finite volume schemes on 3D arbitrary unstructured polyhedral grids”, AIAA Paper No. 99-3259-CP, 1999.
12. FLUENT Computational Fluid Dynamics Software, Version 6.3.26 (Fluent, Inc., Centerra Resource Park, 10 Cavendish Court, Lebanon, NH 03766).
13. J. Franke, and W. Frank, “Large eddy simulation of the flow past a circular cylinder at Re_D=3900”, *Journal of Wind Engineering and Industrial Aerodynamics*, Vol. 90, 2002, pp. 1191-1206.
14. Jacob A. Freeman, “Computational Fluid Dynamics Investigation of Vortex Breakdown for a Delta Wing at High Angle of Attack”, Thesis submitted to the Department of the Air Force Air University, Air Force Institute of Technology, Ohio, 2003.
15. J. Frohlich, W. Rodi, P. Kessler, J. P. Bertoglio, and D. Laurence, “Large eddy simulation of flow around circular cylinder on structured and unstructured grids”, *In: E. H. Hirshel, editor. Notes on numerical fluid mechanics*, Vol. 66, 1998, pp. 319- 338.
16. R. E. Gordnier and M. R. Visbal, “Compact Difference Scheme Applied to Simulation of Low-Sweep Delta Wing Flow”, *AIAA Journal*, Vol. 43, No. 8, 2005, pp. 1744–1752.
17. R. E. Gordnier and M. R. Visbal, “High-Order Simulation of Low Sweep Delta Wing Flows Using ILES and Hybrid RANS/ILES Models,” AIAA-2006-504, January 2006.
18. R. E. Gordnier and M. R. Visbal, “Instabilities in the Shear Layer of Delta Wings,” AIAA-95-2281, June 1995.
19. R. E. Gordnier and M. R. Visbal, “Unsteady Vortex Structure over a Delta Wing,” Journal of Aircraft, Vol. 31, No. 1, Jan.-Feb. 1994, pp. 243–248.
20. S. Görtz, “Detached-Eddy Simulations of a Full-Span Delta Wing at High Incidence”, *AIAA-2003-4216*, June 2003.
21. D. Gottlieb, and S. A. Orszag, “Numerical Analysis of Spectral Methods: Theory and Applications”, *Society for Industrial and Applied Mathematics*, Philadelphia, 1977.

22. O. M. Griffin, “A note on bluff body vortex formation”, *Journal of Fluid Mechanics*, Vol. 284, 1995, pp. 217-224.
23. I. Gursul, “Review of Unsteady Vortex Flows over Slender Delta Wings”, *Journal of Aircraft*, Vol. 42, No. 2, 2005, pp. 299–319.
24. I. Gursul, R. E. Gordnier, and M. Visbal, “Unsteady Aerodynamics of Nonslender Delta Wings”, *Progress in Aerospace Sciences*, Vol. 41, No. 7, 2005, pp. 515–557.
25. I. Gursul, G. Taylor, and C. L. Wooding, “Vortex Flows over Fixed-Wing Micro Air Vehicles”, *AIAA Paper* 2002-0698, Jan. 2002.
26. R. P. Hasen, and L. N. Long, “Large eddy simulation of a circular cylinder on unstructured grids”, *AIAA Paper* 2002-0982.
27. C. T. Hsu, G. Mellor, and J. T. Yen, “Some Flow Analysis of a Tornado-Type Wind Turbine”, ASME Winter Annual Meeting, December 1978.
28. P. G. Huang, Z. J. Wang, and Y. Liu, “An Implicit space-time Spectral Difference method for discontinuity capturing using adaptive polynomials”, *AIAA-2005-5255*.
29. H.T. Huynh, “A Flux Reconstruction Approach to High-Order Schemes Including Discontinuous Galerkin Methods,” *AIAA-2007-4079*.
30. G. E. Karniadakis, and S. J. Sherwin, “Spectral/hp Element Methods for CFD”, *Oxford University Press*, 1999.
31. E. Konstantinidis, S. Balabani, and M. Yianneskis “Conditional averaging of PIV plane wake data using a cross-correlation approach”, *Experiments in Fluids*, Vol. 39, 2005, pp. 38-47.
32. E. Konstantinidis, S. Balabani, and M. Yianneskis, “The effect of flow perturbations on the near wake characteristics of a circular cylinder”, *Journal of Fluids and Structures*, Vol. 18, 2003, pp. 367-386.
33. D. A. Kopriva, “A conservative staggered-grid Chebyshev multidomain method for compressible flows”, *Journal of Computational Physics*, Vol. 125, 1996, pp. 244-261.
34. A. G. Kravchenko, and P. Moin, “B-spline methods and zonal grids for numerical simulations of turbulent flows”, *Technical report TF-73, Department of Mechanical Engineering, Stanford University, USA*, 1998.

35. A. G. Kravchenko, and P. Moin, “Numerical studies of flow over a circular cylinder at Re_D=3900”, *Physics of Fluids*, Vol. 12, 2000, pp. 403-417.

36. M. Laurenco, and C. Shih, “Characteristics of the plane turbulent near wake of a circular cylinder, a particle image velocimetry study”, *Private communication by Beaudan and Moin*, 1993.

37. W. S. Lewellen, “A Review of Confined Vortex Flows”, NASA CR-1772, 1971.

38. C. Liang, and G. Papadakis, “Large eddy simulation of pulsating flow over a circular cylinder at subcritical Reynolds number”, *Computers and Fluids*, Vol. 36, n 2, February 2007, pp. 299-312.

39. Y. Liu, M. Vinokur, and Z. J. Wang, “Discontinuous Spectral Difference Method for Conservation laws on unstructured grids”, *In proceedings of the 3rd International Conference in CFD, Toronto, Canada*, July 2004.

40. Y. Liu, M. Vinokur, and Z. J. Wang, “Multi-dimensional Spectral Difference method for unstructured grids”, *AIAA-2005-0320*.

41. Y. Liu, M. Vinokur, and Z. J. Wang, “Spectral (Finite) Volume Method for Conservation Laws on Unstructured Grids V: Extension to Three-Dimensional Systems”, *Journal of Computational Physics*, Vol. 212, 2006, pp. 454-472.

42. X. Ma, G. S. Karamanos, and G. E. Karniadakis, “Dynamics and low dimensionality of a turbulent near wake”, *Journal of Fluid Mechanics*, Vol. 410, 2000, pp. 29-65.

43. H. Mansy, P. M. Yang, and D. R. Williams, “Quantitative measurements of three-dimensional structures in the wake of a circular cylinder”, *J. of fluid mechanics*, Vol. 270, 1994, pp. 227.

44. J. J. Miau, K. T. Kuo, W. H. Liu, S. J. Hsieh, J. H. Chou, and C. K. Lin, “Flow Developments above 50-Deg Sweep Delta Wings with Different Leading-Edge Profiles”, *Journal of Aircraft*, Vol. 32, No. 4, 1995, pp. 787-794.

45. R. Mittal, and P. Moin, “Suitability of upwind-biased finite-difference schemes for large-eddy simulation of turbulent flow”, *AIAA Journal*, Vol. 35, 1997, pp. 1415-8.

46. S. A. Morton, “High Reynolds Number DES Simulations of Vortex Breakdown over a 70m Degree Delta Wing”, *AIAA-2003-4217*, June 2003.

47. S. A. Morton, J. Forsythe, A. Mitchell and D. Hajek, "DES and RANS Simulations of Delta Wing Vortical Flows", *AIAA-2002-0587*, January 2002.
48. R. D. Moser, M. M. Rogers, and D. W. Ewing, "Self-similarity of time evolving plane wakes", *Journal of Fluid Mechanics*, Vol. 367, 1998, pp. 255-289.
49. C. Noberg, "Interaction of free stream turbulence and vortex shedding for a single tube in cross-flow", *Journal of Wind Engineering and Industrial Aerodynamics*, Vol. 23, 1986, pp. 501-514.
50. M. V. Ol, and M. Gharib, "Leading-Edge Vortex Structure of Nonslender Delta Wings at Low Reynolds Number", *AIAA Journal*, Vol. 41, No.1, 2003, pp. 16-26.
51. L. Ong, and J. Wallace, "The velocity field of the turbulent very near wake of a circular cylinder", *Exp. Fluids*, Vol. 20, 1996, pp. 441-453.
52. M. M. Rai, and P. Moin, "Direct numerical simulation of transition and turbulence in a spatially evolving boundary layer", *Journal of Computational Physics*, Vol. 109, 1993, pp. 169.
53. D. Rockwell, "Three-Dimensional Flow Structure on Delta Wings at High Angle-of-Attack: Experimental Concepts and Issues," AIAA-93-0550, January 1993.
54. T. Sarpkaya, "A critical review of the intrinsic nature of vortex-induced vibrations", *Journal of Fluids and Structures*, Vol. 19, 2004, pp. 389-447.
55. Y. Sun, Z. J. Wang and Y. Liu, "Efficient Implicit Non-linear LU-SGS Approach for Compressible Flow Computation Using High-Order Spectral Difference Method", *Communications in Computational Physics*, Vol. 5, No. 2-4, pp. 760-778, 2009.
56. Y. Sun, Z. J. Wang and Y. Liu, "High-Order Multidomain Spectral Difference Method for the Navier-Stokes Equations on Unstructured Hexahedral Grids", *Communications in Computational Physics*, Vol. 2, No. 2, pp. 310-333, 2007.
57. G. S. Taylor and I. Gursul, "Unsteady Vortex Flows and Buffeting of a Low Sweep Delta Wing", *AIAA-2004-1066*, January 2004.
58. G. S. Taylor, T. Schnorbus, and I. Gursul, "An Investigation of Vortex Flows over Low Sweep Delta Wings", *AIAA-2003-4021*, June 2003.
59. A. Travin, M. Shur, M. Strelets, and P. Spalart, "Detached-eddy simulations past a circular cylinder", *Flow, Turbulence and Combustion*, Vol. 63, 1999, pp. 293-313.

60. K. Van den Abeele, C. Lacor and Z.J. Wang, "On the stability and accuracy of the spectral difference method," *Journal of Scientific Computing*, in press.
61. M. R. Visbal, "Computed Unsteady Structure of Spiral Vortex Breakdown on Delta Wings," AIAA-96-2074, June 1996.
62. M. R. Visbal and R. E. Gordnier, "Origin of Computed Unsteadiness in the Shear Layer of Delta Wings," Journal of Aircraft, Vol. 32, No. 5, 1995, pp. 1146–1148.
63. M. R. Visbal, and R. E. Gordnier, "On the Structure of the Shear Layer Emanating form a Swept Leading Edge at Angle of Attack," AIAA-2003-4016, June 2003.
64. Z. J. Wang, "Spectral volume and difference methods for unstructured grids", VKI lecture series, 2005.
65. Z. J. Wang, and R.F. Chen, "Anisotropic Solution Adaptive Viscous Cartesian Grid Method for Turbulence Flow Simulation", AIAA Journal, Vol. 40, No. 10, Oct. 2002.
66. Z. J. Wang, and Y. Liu, "Spectral (Finite) Volume Method for Conservation Laws on Unstructured Grids III: Extension to One-Dimensional Systems", *Journal of Scientific Computing*, Vol. 20, No. 1, 2004, pp. 137-157.
67. Z. J. Wang, and Y. Liu, "The Spectral Difference method for the 2D Euler equations on unstructured grids", *AIAA-2005-5112*.
68. Z. J. Wang, L. Zhang, and Y. Liu, "Spectral (Finite) Volume method for conservation laws on unstructured grids IV: extension to two-dimensional systems", *Journal of Computational Physics*, Vol. 194, 2004, pp. 716-741.
69. C. H. K. Williamson, "Vortex dynamics in the cylinder wake", *Annual Review of Fluid Mechanics*, Vol. 28, 1996, pp. 477-539.
70. C. H. K. Williamson, and R. Govardhan, "Vortex Induced Vibrations", *Annual Review of Fluid Mechanics*, Vol. 36, 2004, pp. 413-455.
71. C. H. K. Williamson, J. Wu, and J. Sheridan, "Scaling of Streamwise Vortices in Wakes", *Physics of Fluids*, Vol. 7, 1995, pp. 2307.
72. B. Yaniktepe and D. Rockwell, "Flow Structure on a Delta Wing of Low Sweep Angle", *AIAA Journal*, Vol. 42, No. 3, 2004, pp. 513–523.

73. J. T. Yen, “Summary of Recent Progress on Tornado-Type Wind Energy Systems”, Third Wind Energy Workshop, ed. J. B. F. Scientific Corp., Washington D. C., September 1977, pp. 808-818.

74. J. T. Yen, “Tornado-Type Wind Energy System”, Proceedings, Intersociety Energy Conversion Engineering Conference, September 1975, pp. 987-994.

75. J. T. Yen, “Tornado-Type Wind Energy System, Basic Considerations”, ASME Paper 76-WA-Ener-2, 1976.

76. S. Yoon and A. Jameson A, “Lower-upper symmetric-Gauss-Seidel method for the Euler and Navier-Stokes equations”, *AIAA Journal*, 1988, Vol. 26, pp. 1025-1026.